Exoplanet Mass-Radius Relations Verified by the Solar System

Exoplanet Mass-Radius Relations Incorporating State-of-the-art Physics Validated on Solar System Objects

By
BENNETT NEIL SKINNER,
BSc (Astronomy),
BSc (Physics)

A Thesis Submitted to the School of Graduate Studies
in the Partial Fulfillment of the Requirements for the Degree of

Master of Science
in
Physics & Astronomy (Astrobiology)

McMaster University
Hamilton, Ontario

Master of Science (2025)
Physics & Astronomy
McMaster University
Hamilton, Ontario, Canada

TITLE: Exoplanet Mass-Radius Relations Incorporating State-of-the-art Physics Validated on Solar System Objects

AUTHOR:
Bennett Neil Skinner,
BSc (Astronomy)
BSc (Physics)

SUPERVISORS:
Ralph Pudritz,
Professor Emeritus, Physics & Astronomy,
McMaster University, ON, Canada

Ryan Cloutier,
Assistant Professor, Physics & Astronomy,
McMaster University, ON, Canada

SUPERVISORY COMMITTEE MEMBER:
Dr. Greg Slater
Professor, Earth, Environment & Society,
McMaster University, ON, Canada

NUMBER OF PAGES: xiii, 143

Lay Abstract

Determining the materials that planets around other stars are made out of requires the construction of planetary interior structure models. In this thesis we present a new model that includes features often not included in previous models, such as: new calculations for the density of materials at high pressures, allowing multiple materials to coexist on the same layer of the planet, and transitions of materials between different structures. We verify that our model is accurate by comparing it to the size of Earth, Mars, the Moon, Venus, Mercury, and Europa (a moon of Jupiter). We also compare our model to a number representing how the mass inside a planet is distributed. We get numbers with $<0.5\%$ error. We create graphs using our model for the sizes of planets with different compositions and masses. These graphs can be compared to the measured masses and sizes of planets to guess their compositions.

Abstract

Understanding a planet's composition is necessary to understand its habitability. Inferring a planet's composition solely from observations of mass and radii requires the construction of planetary interior structure models. We present a new planetary interior structure model that includes significant physics excluded from previous models, such as the coexistence of many chemical species within the mantle, high pressure phase transitions of mantle materials, light elements within the planetary core and partitioning between the solid and liquid core, radiative transfer in the upper atmosphere, a prescription to calculate planetary transit radii rather than radii at a particular pressure, and more. We validate our resultant interior structure model by running forward models for the measured masses and compositions of Earth, Mars, the Moon, Venus, Mercury, and Europa. Our model produces radii and moment of inertia coefficients within 0.5% or 1 standard deviation of reality in all cases where the moment of inertia is well-constrained. In the case of a poorly-constrained moment of inertia, our model produces radii and moment of inertia coefficients within 1% or 3 standard deviations of reality. We present the resultant mass-radius curves between 0.01 and 100 $M_{\oplus}$. We find that the radii of sub-Neptunes are consistent with planets made of either a few % H/He or 10s of % H_2O, with surface temperature also playing a crucial factor. We find radii for pure Fe planets significantly systematically lower than much of the literature owing to our adoption of newer EOS. We fit power laws of the form $M = R^X$ in a piecewise fashion with pieces being separated by changes in the state of the planetary interior: for a planet with Earth's composition, the solidification of the core at 2.25 $M_{\oplus}$ and onset of high pressure phases in the mantle at 3.41 $M_{\oplus}$. At higher masses and core mass fractions, X becomes larger. The values of X for Earth-like and cold water worlds are within 1%. Previous values of X reported in the literature are only valid at masses below the solidification of the core.

Acknowledgements

Thank you to the members of my committee, Ralph Pudritz, Ryan Cloutier, and Greg Slater, for comments that have improved this work. Thanks especially to my advisors, Ralph Pudritz and Ryan Cloutier.

Thank you to Caroline Dorn, Jonas Haldemann, Komal Bali, Ankan Sur, and Artem Aguichine for discussions about their interior structure models.

Thank you to Laura Schaefer for comments on the model that have resulted in improvements.

Thank you to my officemates, Atesh Goksu, Emily Rock, Nicholas Owens, and Rachel Pillsworth for sanity checks on points with the abstract.

Thank you to the students in the condensed matter section of the department, Xinran Liu, Charles Cai, and Daniel Sepulveda, for clarifications on notation used within publications providing EOS.

Thank you to the other students within Ryan Cloutier and Ralph Pudritz's research groups during the preparation of this thesis, Drew Weisserman, Erik Gillis, Nicole Gromek, Raven Westlake, Dilen Moodelly, and Tamara Koletic for comments on the work during group meetings which improved its final form.

Thank you to my mom, Emily Skinner, father, Ted Skinner, sister, Lilly Skinner, grandmothers, Marie Neil and Ann Cody, and grandfathers, Richard Neil and Jerry Skinner for encouraging me to pursue my interests in astronomy.

And finally, thank you to every teacher and professor I have had that has given me the requisite knowledge to carry out this work.

Contents

List of Figures

List of Tables

Declaration of Academic Achievement

I, Bennett Neil Skinner, declare that this thesis titled, **Exoplanet Mass-Radius Relations Incorporating State-of-the-art Physics Validated on Solar System Objects**, and works presented in it are my own. I confirm that

- I produced all writing in Chapter 1
- I was the lead author for Chapter 2, writing the entirety of the first draft, composing all of the code, and performing the majority of the analysis. The conclusions are my own with secondary input from the second and third authors.
- I produced all writing in Chapter 3

Chapter 1

Introduction

1.1 Framing the Problem

We, as with all known life, live on a planet orbiting the sun: Earth. The history of life on our planet is intricately connected with the history of our planet, with essential parameters necessary for life such as the chemical inventory and temperature of its surface (Westall and Xiao; 2024; Werlen et al.; 2025), the presence of a magnetic field (González-Cataldo and Militzer; 2023), and its surface gravity all depending on the structure of the planet. The importance of these parameters can be readily observed by a view around the solar system: although there are seven other planets, $\gtrsim 20$ large moons (>198 km radii) (Archinal et al.; 2018), and $\gtrsim 100$ dwarf planets[1], none are known to currently or have ever harboured life. These objects span a large parameter space in mass and bulk composition, from Europa (Petricca et al.; 2025)–less than a hundredth the mass of Earth with a $\sim 10\%$ water mass fraction–to Jupiter, more than a hundred times the mass of Earth with a $\gtrsim 90\%$ H/He mass fraction (Howard and Guillot; 2023).

With the thusfar nondetection of life elsewhere around our star, the search has turned to the rest of the universe. As of writing, $\lesssim 6000$ planets orbiting around other stars–exoplanets–have been discovered[2]. Many of these objects occupy parts of parameter space that are not present in our solar system. Are these parts of parameter space–not identical to life-harbouring Earth but also not identical to the likely lifeless bodies in the rest of the solar system–habitable? Determining so requires an understanding of the compositions of these planets.

At the great distances from Earth of these exoplanets, detailed characterization of the majority of the population beyond masses, radii, and equilibrium temperatures (see

[1] `https://web.gps.caltech.edu/~mbrown/dps.html`
[2] `https://exoplanetarchive.ipac.caltech.edu/`

subsection 1.2 for characterization of these parameters) is intractable (beyond atmospheric characterization that has been conducted on a minority of the total population[3] and is beyond the scope of this study).

Several studies have thus been undertaken to create models that calculate the radii of a planet for a known temperature, mass, and composition (e.g. Sotin et al.; 2007; Seager et al.; 2007; Valencia et al.; 2007; Haldemann et al.; 2024; Unterborn et al.; 2023; Dorn et al.; 2017; Plotnykov and Valencia; 2024; Acuña et al.; 2021; Rice et al.; 2025; Aguichine et al.; 2025; Lopez and Fortney; 2014; van den Berg et al.; 2019; Boujibar et al.; 2020; Sur et al.; 2024; Zeng et al.; 2019). These models rely on solving a system of ordinary differential equations that includes equations of state (the pressure and temperature dependence of material parameters). As denser objects sink towards the bottom of gravity wells, planets are generally assumed broken into several compositional layers, from the outermost least dense to innermost most dense layer: a H/He envelope, a water layer, a silicate-dominated mantle, and an iron-dominated core.

The curves in radius of these model planets for a set of fixed parameters but varying mass (isocomposition curves) are then compared against the distribution of known planetary masses or radii to infer the compositions of known planets. This serves as a crucial broad constraint on the diversity of observed planets in the universe. The crucial step of inverting this relationship–directly inferring the composition of an individual planet from its mass and radius (Dorn et al.; 2015)–is left to future work.

We highlight three classes of objects within the population of observed exoplanets that are not present within our solar system and can thus only be understood through exoplanetary studies: super-Mercuries, super-Earths, and sub-Neptunes. Super-Mercuries are planets with high densities for their masses, super-Earths are planets with densities consistent with being a scaled-up version of the Earth, and sub-Neptunes are planets with radii greater than super-Earths at a similar mass. The overall population of planetary radii when accounting for observational bias is bimodal, with a super-Earth peak and a sub-Neptune peak separated by a radius valley at $\sim$1.7 $R_\oplus$ (Fulton et al.; 2017; Fulton and Petigura; 2018; Cloutier and Menou; 2020).

Isocomposition curves are consistent with sub-Neptunes containing either (1) $\lesssim$ to a few % H/He or (2) tens of % H_2O or (3) a combination thereof. These two compositions result in extremely different planetary environments and thus any investigation of the broad abundance of habitable environments in the universe must discern the relative

[3] `https://exoplanetarchive.ipac.caltech.edu/cgi-bin/atmospheres/nph-firefly?atmospheres`

abundance of these three categories (Radecka and Rimmer; 2025; Rigby and Madhusudhan; 2024; Kite and Ford; 2018; Chakrabarty and Mulders; 2024; Tang et al.; 2025; Rigby et al.; 2024; Dorn and Lichtenberg; 2021). Sub-Neptunes may be the most common type of planet within the habitable zone (the region around a star where liquid water could be sustained under a CO-H_2O-N_2 atmosphere) (Bergsten et al.; 2022).

Precise characterization of super-Earths is important as current observations indicate that they are the most common type of planet around the most common type of star (Cloutier and Menou; 2020; Henry and Jao; 2024). The detection of truly Earth-like planets is currently at the reaches of available technology, so many more super-Earths are known than Earths, regardless of the true intrinsic population (Hara and Ford; 2023; Heller et al.; 2022; Dattilo et al.; 2023).

Motivated by the astrobiological importance of super-Earths and sub-Neptunes, in this work we create new interior structure models accounting for more physics than any previous interior structure model (see Chapter 2).

Although the other objects in the solar system are uninhabited to our current knowledge, their probing of a large region in parameter space allows us to test our interior structure model. If our model is able to recover the true radii and moment of inertia coefficients (a measure of the distribution of mass within a planetary interior) of a wide range of solar system objects when the object's compositions are constrained by other means (e.g. seismology), it indicates their accuracy.

The remainder of this thesis is structured as follows: the remainder of Chapter 1 gives background on exoplanets as well as how EOS for interior structure models are determined; Chapter 2 gives more background on interior structure models and the functional forms of equations of state, presents our model, validates the model, presents results for our model, and discusses those results; Chapter 3 provides a summary of our results within the broad context presented here and discusses future directions to take this work; the Appendix elaborates on some points not discussed in the main text.

1.2 Exoplanet Detection Methods

There are several exoplanet discovery methods, of which two have contributed the most to the current body of known exoplanets: the radial velocity method and the transit method.

In the transit method, exoplanets are discovered by the dip in their host star's luminosity as observed from Earth as they move in front of the star along our line of sight (Winn; 2010). The relative decrease in brightness of the star is proportional to the area of the star that is occulted by the planet and thus the ratio of the planet's radius to its star's radius (Winn; 2010). The radius of the planet can thus be estimated once its star's radius is estimated. The time between occultations gives the orbital period of the planet which can then be used to calculate the surface temperature of the planet assuming thermal equilibrium.

In the radial velocity method, exoplanets are discovered by the Doppler shift of their host star's radial velocity along our line of sight due to motion of the star around the stellar-planet center of mass. For a circular orbit, the amplitude of this Doppler shift is determined by the mass of the host star, the mass of the planet, the inclination of the system (the angle between the planet's orbital plane and the observer's line of sight), the period of the planet's orbit, and the planet's eccentricity (deviation of its orbit from circular). The planetary eccentricity and period can be extracted from the shape of the host star's radial velocity curve (Hogg et al.; 2010). The period can then be converted to the surface temperature of the planet. The inclination of the system is known to be near-90 if the planet transits, otherwise, an average inclination can be assumed for statistical studies as inclinations are isotropic (Lovis and Fischer; 2010).

A planet's mass and radius can thus be simultaneously determined using the two different exoplanet detection methods, so long as its host star's mass and radius are known. These two parameters combine to give the bulk density of the planet. The inference of the composition of a planet from this parameter is the subject of this thesis.

1.3 Errors on Planetary Masses and Radii

As noted in Section 1.2, the determination of a planet's mass and radii depends on the determination of its host star's mass and radii. In the case of planetary radii, the error in stellar radii is the dominant source of error (Otegi et al.; 2020).

There are four main strategies for estimating stellar radii: (1) astroseismology, (2) eclipsing binaries, (3) interferometry, and (4) the Stefan-Boltzmann law (Moya et al.; 2018). The first two can also be used to estimate stellar masses.

Astroseismology derives stellar radii and masses by comparing the oscillation frequencies observed in a star to those predicted by a grid of models with varying stellar

parameters, including radii and mass, and determining the radii which match the oscillations (Basu et al.; 2010; Moya et al.; 2018). Stellar radii can also be attained by scaling relations comparing their observed astroseismic parameters to the sun (Bellinger et al.; 2019; Kjeldsen and Bedding; 1995). In an eclipsing binary–a system of two stars that orbit each other in a plane aligned with our line of sight leading to periodic eclipses of each star by the other–their radii can be determined by their transits (Kallrath; 2009). The sum of the stellar radii is the total time it takes for the eclipse to occur, since the eclipse occurs when any part of one star overlaps the other (Kallrath; 2009). The ratio of stellar radii is determined by the relative time during which the eclipse is at its maximum depth (indicating that both stars are completely overlapping) and the time during which the eclipse is not at its maximum depth (indicating that the stars are not completely overlapping and the eclipsing star is currently moving in front of the occulted star) (Kallrath; 2009). The combination of the ratio of stellar radii and the sum of stellar radii produces individual stellar radii to high accuracy (Torres et al.; 2010).

If the two stars in the eclipsing binary can be visually distinguished, their relative distances from the center of mass of the system gives their mass ratio (Kallrath; 2009). The total distance between the stars and the period of the eclipsing binary's orbit can be combined with Kepler's Third Law to derive the total mass of the system (Kallrath; 2009). The combination of the ratio of stellar mass and the sum of stellar masses produces individual stellar masses (Kallrath; 2009).

Eclipsing binaries are thus important for their simultaneous constraint on stellar masses and radii, however, eclipsing binaries are rare and planets around them rarer still (Stassun et al.; 2018; Moe and Kratter; 2021).

Interferometry is a technique that allows extremely high angular resolutions to be reached and thus stellar angular radii to be observed directly, which can then be converted into physical radii if the distance to the star is known, as is now almost always the case due to Gaia (Boyajian et al.; 2012; Ligi et al.; 2016; Gaia Collaboration et al.; 2016, 2018, 2023).

The Stefan-Boltzmann law relates the luminosity of an object to its temperature and radius, so if the temperature of a star can be determined from the shape of its spectrum and its luminosity can be determined from its brightness and Gaia-determined distance, its radius can be estimated (Stassun et al.; 2017, 2018; Schweitzer et al.; 2019).

The techniques presented above are not universal, so empirical relations derived from systems where the techniques are applicable are necessary to estimate stellar radii (if

no constraint on the stellar radius is possible) or stellar masses (if the radius can be measured but not the mass, as in the latter two cases) (Moya et al.; 2018; Schweitzer et al.; 2019). Relations can also be established using stellar evolution models, although the validity of these models ultimately comes from their replication of the measured mass-radius relation (del Burgo and Allende Prieto; 2018). Stellar density can also be determined for the host of a transiting exoplanet using its semi-major axis, period, and transit time (Seager and Mallén-Ornelas; 2003; Stevens et al.; 2018), which can then be combined with a stellar mass or radius to produce the other.

The important consequence of these techniques is to establish a lower limit on planetary radii estimate uncertainties of $\gtrsim 1\%$ (Schweitzer et al.; 2019), much more accurate than the typical mass uncertainties for the $< 100\ M_{\oplus}$ uncertainties of interst in this study ($\sim 25\%$). This lower limit on planetary radii estimate uncertainties is comparable to the error that many exoplanet interior structure models in the literature have (see Section 2.5.2), indicating that the theoretical error on planetary radii could approach the observational error. This would cause inferred compositions from the observed parameters of exoplanets to be significantly off. This motivates the creation of a new planetary interior structure model with errors significantly lower than observational errors, the subject of this thesis.

1.4 Determining Equations of State

Solving for the interior structure of a planet requires a set of Equations of State (EOS) for the species comprising the planet. EOS give the density and adiabatic temperature gradient of a species at some pressure and temperature, both necessary to solve the ordinary differential equations solved in an interior structure model (see Section 2.2.1). The functional forms of EOS are discussed in Section 2.2.2, here we discuss how the EOS for a particular species is determined experimentally or numerically.

There are three main sources of EOS: static compression, dynamic compression, and simulated data (Dong et al.; 2025). Experimental limitations mean that static compression can only access pressures up to a few hundred GPa and dynamic compression can only access pressures up to approximately a TPa. The cores of exoplanets more than a few times the mass of the Earth reach pressures beyond these experimentally-tested regions, necessitating the usage of simulated data (Hakim et al.; 2018).

Static compression involves compressing a material and taking measurements of its

properties in situ (Mao et al.; 2018). The method capable of accessing the highest pressures is diamond anvil compression, which involves the compression of a material between two diamond anvils (Mao et al.; 2018). Diamond is selected because it is the hardest known material (Mao et al.; 2018). Classical diamond anvils have reached pressures of up to 120 GPa, but pressures as high as 400 GPa can be reached if the diamond anvil surfaces are beveled, allowing the surface of the anvil to serve as a second-stage anvil (Mao et al.; 2018). The pressures that materials are experiencing are determined by the simultaneous compression of materials whose properties at high pressures are already known, allowing the inference of the pressure within the cell from their properties (Mao et al.; 2018). The ultimate limit to the pressures that diamond anvils can achieve is the strength of the material of the anvil (Dubrovinskaia et al.; 2016). New materials are currently being investigated that can push static compression to higher pressures, but have not yet been incorporated into studies of the materials of interest and thusfar can only be used at room temperatures (Dubrovinskaia et al.; 2016; Mao et al.; 2018; Dong et al.; 2025; Duffy and Smith; 2019).

Dynamic compression involves the shocking of a material, generating a mechanical wave within it that generates high pressures (Duffy and Smith; 2019). These shocks can be generated by many means, with the most common for high pressure parameter space being a laser or a projectile accelerated by a strong magnetic field (Duffy and Smith; 2019; Fei et al.; 2021). Although this technique accesses higher pressures than static compression, its chief weakness is that it can only access regions in pressure-temperature space along a specific curve known as the Hugoniot curve along which shocked matter follows (Duffy and Smith; 2019). It thus cannot be used to sample the EOS across all of pressure-temperature space and is specifically biased to high temperatures at high pressures (Duffy and Smith; 2019; Ichikawa and Tsuchiya; 2020).

Able to access any pressure-temperature combination at any pressure are simulations. However, simulations including all known physics are computationally intractable, necessitating the introduction of approximations that may make simulations invalid in reality. The set of approximations most relevant to high-pressure physics is Density Functional Theory (DFT), which was the subject of the 1998 Nobel Prize in Chemistry (Schwarz et al.; 2010). The essential problem is to find the ground state of a system by minimizing the total energy in the Schrödinger equation, however, the computational cost of doing so directly scales exponentially with the number of electrons (Car; 2002). DFT avoids this issue by employing the two theoroms of Hohenberg and Kohn (1964): (1) the ground state of a system of electrons subject to an external potential is uniquely determined by

the electron density and (2) the energy of any positive trial density will be greater than or equal to the ground state (Harrison; 2003; Car; 2002). These facts combine into the fundamental statement of DFT, presented in Equation 1.1 (Harrison; 2003), where $E(\rho)$ is a function of energy in terms of density, $\vec{r}$ is a position, μ is the chemical potential, and N is the number of electrons.

$$\delta(E(\rho) - \mu \int (\rho(\vec{r})d\vec{r} - N) = 0 \tag{1.1}$$

The functional form of $E(\rho)$ presented in equation 1.2 is obtained via three further steps. The first is the separation of the Coloumb energy (Harrison; 2003). The second is the application of the Born-Oppenheimer approximation, which states that the electronic contribution to the atomic energy is much larger than the nuclear contribution and thus the electronic and nuclear terms can be separated (Essén; 1977; Born and Oppenheimer; 2000)–meaning that the atomic nuclei can be treated as an external static potential (Car; 2002). The third is Kohn and Sham (1965)'s approximation of the kinetic energy of the system as arising from a system of non-interacting electrons with a density identical to the ground state of the true system described by the orbital wavefunction $\rho(\vec{r}) = \sum_i^N |\phi_i|^2$. The four terms of Equation 1.2, from left to right, are the kinetic energy of the non-interacting electrons, the external potential, potential from the Coloumb interaction, and a correction term.

$$E(\rho) = T_S(\rho) + V_{\text{ext}}(\rho) + V_H(\rho) + E_{\text{xc}}(\rho) \tag{1.2}$$

Combining Equations 1.1 and 1.2 and re-expressing in terms of ϕ yields the Kohn-Sham equations, reproduced in Equation 1.3, where ε_i are a set of eigenvalues called the Kohn-Sham eigenvalues (Harrison; 2003; Car; 2002).

$$(-\frac{1}{2}\nabla^2 + V_{\text{ext}}(\vec{r}) + \int \frac{\rho(\vec{r})}{|\vec{r} - \vec{r}'|}d\vec{r} + \frac{\delta E_{\text{xc}}}{\delta\rho(\vec{r})})\phi_i(\vec{r}) = \varepsilon_i\phi_i(\vec{r}) \tag{1.3}$$

All that remains is an exact solution for E_{xc} and the result of Equation 1.3 is exact. However, the determination of E_{xc} generally requires further approximations that vary depending on the system. In some systems, E_{xc} is exactly determined, allowing accurate approximations (Harrison; 2003). This means that DFT can be used to make unbiased predictions of material properties (Harrison; 2003). One such approximation for E_{xc} is the local density approximation (LDA), which states that $E_{\text{xc}}(\vec{r}) = E_{\text{xc}}(\rho(\vec{r}))$, that is, E_{xc} depends only on the local density (Perdew and Zunger; 1981; Car; 2002; Harrison; 2003).

DFT can further be expanded into Ab Initio Molecular Dynamics (AIMD), which accounts for the motion of atoms, as is necessary to represent a fluid, high-temperature solid, or a phase transition (Car; 2002). This can be achieved by integrating equation 1.3 and the equations of motion or by employing one of several approximations of such an integration (Car and Parrinello; 1985; Wentzcovitch; 1991; Kresse and Hafner; 1993; Iftimie et al.; 2005; Car; 2002).

In the intermediate pressures at which all methods meet, the EOS tend to agree (Hakim et al.; 2018; Sakai et al.; 2016; Musella et al.; 2019). However, DFT at low pressures systematically overpredicts densities due to the assumptions it makes (Hakim et al.; 2018; Pourovskii et al.; 2014). A fully accurate interior structure model must thus employ different EOS at high and low pressures.

In sum, low pressures can be accessed by static compression experiments, intermediate pressures can be accessed by shock compression experiments but only at certain temperatures, and high pressures can be accessed by simulations. The results of each technique agree at intermediate pressures, but extrapolation of simulations to low pressures is inaccurate, necessitating the usage of separate low and high pressure EOS (see Section 2.2.6).

Bibliography

Acuña, L., Deleuil, M., Mousis, O., Marcq, E., Levesque, M. and Aguichine, A. (2021). Characterisation of the hydrospheres of TRAPPIST-1 planets, **647**: A53.

Aguichine, A., Batalha, N., Fortney, J. J., Nettelmann, N., Owen, J. E. and Kempton, E. M. R. (2025). Evolution of Steam Worlds: Energetic Aspects, **988**(2): 186.

Archinal, B. A., Acton, C. H., A'Hearn, M. F., Conrad, A., Consolmagno, G. J., Duxbury, T., Hestroffer, D., Hilton, J. L., Kirk, R. L., Klioner, S. A., McCarthy, D., Meech, K., Oberst, J., Ping, J., Seidelmann, P. K., Tholen, D. J., Thomas, P. C. and Williams, I. P. (2018). Report of the IAU Working Group on Cartographic Coordinates and Rotational Elements: 2015, *Celestial Mechanics and Dynamical Astronomy* **130**(3): 22.

Basu, S., Chaplin, W. J. and Elsworth, Y. (2010). Determination of Stellar Radii from Asteroseismic Data, **710**(2): 1596–1609.

Bellinger, E. P., Hekker, S., Angelou, G. C., Stokholm, A. and Basu, S. (2019). Stellar ages, masses, and radii from asteroseismic modeling are robust to systematic errors in spectroscopy, **622**: A130.

Bergsten, G. J., Pascucci, I., Mulders, G. D., Fernandes, R. B. and Koskinen, T. T. (2022). The Demographics of Kepler's Earths and Super-Earths into the Habitable Zone, **164**(5): 190.

Born, M. and Oppenheimer, R. (2000). On the quantum theory of molecules, *Quantum Chemistry: Classic Scientific Papers*, World Scientific, pp. 1–24.

Boujibar, A., Driscoll, P. and Fei, Y. (2020). Super-Earth Internal Structures and Initial Thermal States, *Journal of Geophysical Research (Planets)* **125**(5): e06124.

Boyajian, T. S., von Braun, K., van Belle, G., McAlister, H. A., ten Brummelaar, T. A., Kane, S. R., Muirhead, P. S., Jones, J., White, R., Schaefer, G., Ciardi, D., Henry, T., López-Morales, M., Ridgway, S., Gies, D., Jao, W.-C., Rojas-Ayala, B., Parks, J. R., Sturmann, L., Sturmann, J., Turner, N. H., Farrington, C., Goldfinger, P. J. and Berger, D. H. (2012). Stellar Diameters and Temperatures. II. Main-sequence K- and M-stars, **757**(2): 112.

Car, R. (2002). Introduction to density-functional theory and ab-initio molecular dynamics, *Quantitative Structure-Activity Relationships* **21**(2): 97–104.

Car, R. and Parrinello, M. (1985). Unified approach for molecular dynamics and density-functional theory, **55**(22): 2471–2474.

Chakrabarty, A. and Mulders, G. D. (2024). Where Are the Water Worlds? Identifying Exo-water-worlds Using Models of Planet Formation and Atmospheric Evolution, **966**(2): 185.

Cloutier, R. and Menou, K. (2020). Evolution of the Radius Valley around Low-mass Stars from Kepler and K2, **159**(5): 211.

Dattilo, A., Batalha, N. M. and Bryson, S. (2023). A Unified Treatment of Kepler Occurrence to Trace Planet Evolution. I. Methodology, **166**(3): 122.

del Burgo, C. and Allende Prieto, C. (2018). Testing models of stellar structure and evolution - I. Comparison with detached eclipsing binaries, **479**(2): 1953–1973.

Dong, J., Mardaru, G.-D., Asimow, P. D., Stixrude, L. P. and Fischer, R. A. (2025). Structure and Melting of Fe, MgO, SiO_2, and $MgSiO_3$ in Planets: Database, Inversion, and Phase Diagram, **6**(4): 103.

Dorn, C., Khan, A., Heng, K., Connolly, J. A. D., Alibert, Y., Benz, W. and Tackley, P. (2015). Can we constrain the interior structure of rocky exoplanets from mass and radius measurements?, **577**: A83.

Dorn, C. and Lichtenberg, T. (2021). Hidden Water in Magma Ocean Exoplanets, **922**(1): L4.

Dorn, C., Venturini, J., Khan, A., Heng, K., Alibert, Y., Helled, R., Rivoldini, A. and Benz, W. (2017). A generalized Bayesian inference method for constraining the interiors of super Earths and sub-Neptunes, **597**: A37.

Dubrovinskaia, N., Dubrovinsky, L., Solopova, N. A., Abakumov, A., Turner, S., Hanfland, M., Bykova, E., Bykov, M., Prescher, C., Prakapenka, V. B. et al. (2016). Terapascal static pressure generation with ultrahigh yield strength nanodiamond, *Science advances* **2**(7): e1600341.

Duffy, T. S. and Smith, R. F. (2019). Ultra-High Pressure Dynamic Compression of Geological Materials, *Frontiers in Earth Science* **7**: 23.

Essén, H. (1977). The physics of the born–oppenheimer approximation, *International Journal of Quantum Chemistry* **12**(4): 721–735.

Fei, Y., Seagle, C. T., Townsend, J. P., McCoy, C. A., Boujibar, A., Driscoll, P., Shulenburger, L. and Furnish, M. D. (2021). Melting and density of $MgSiO_3$ determined by shock compression of bridgmanite to 1254GPa, *Nature Communications* **12**: 876.

Fulton, B. J. and Petigura, E. A. (2018). The California-Kepler Survey. VII. Precise Planet Radii Leveraging Gaia DR2 Reveal the Stellar Mass Dependence of the Planet Radius Gap, **156**(6): 264.

Fulton, B. J., Petigura, E. A., Howard, A. W., Isaacson, H., Marcy, G. W., Cargile, P. A., Hebb, L., Weiss, L. M., Johnson, J. A., Morton, T. D., Sinukoff, E., Crossfield, I. J. M. and Hirsch, L. A. (2017). The California-Kepler Survey. III. A Gap in the Radius Distribution of Small Planets, **154**(3): 109.

Gaia Collaboration, Brown, A. G. A., Vallenari, A., Prusti, T., de Bruijne, J. H. J., Babusiaux, C., Bailer-Jones, C. A. L., Biermann, M., Evans, D. W., Eyer, L., Jansen, F., Jordi, C., Klioner, S. A., Lammers, U., Lindegren, L., Luri, X., Mignard, F., Panem, C., Pourbaix, D., Randich, S., Sartoretti, P., Siddiqui, H. I., Soubiran, C., van Leeuwen, F., Walton, N. A., Arenou, F., Bastian, U., Cropper, M., Drimmel, R., Katz, D., Lattanzi, M. G., Bakker, J., Cacciari, C., Castañeda, J., Chaoul, L.,

Cheek, N., De Angeli, F., Fabricius, C., Guerra, R., Holl, B., Masana, E., Messineo, R., Mowlavi, N., Nienartowicz, K., Panuzzo, P., Portell, J., Riello, M., Seabroke, G. M., Tanga, P., Thévenin, F., Gracia-Abril, G., Comoretto, G., Garcia-Reinaldos, M., Teyssier, D., Altmann, M., Andrae, R., Audard, M., Bellas-Velidis, I., Benson, K., Berthier, J., Blomme, R., Burgess, P., Busso, G., Carry, B., Cellino, A., Clementini, G., Clotet, M., Creevey, O., Davidson, M., De Ridder, J., Delchambre, L., Dell'Oro, A., Ducourant, C., Fernández-Hernández, J., Fouesneau, M., Frémat, Y., Galluccio, L., García-Torres, M., González-Núñez, J., González-Vidal, J. J., Gosset, E., Guy, L. P., Halbwachs, J. L., Hambly, N. C., Harrison, D. L., Hernández, J., Hestroffer, D., Hodgkin, S. T., Hutton, A., Jasniewicz, G., Jean-Antoine-Piccolo, A., Jordan, S., Korn, A. J., Krone-Martins, A., Lanzafame, A. C., Lebzelter, T., Löffler, W., Manteiga, M., Marrese, P. M., Martín-Fleitas, J. M., Moitinho, A., Mora, A., Muinonen, K., Osinde, J., Pancino, E., Pauwels, T., Petit, J. M., Recio-Blanco, A., Richards, P. J., Rimoldini, L., Robin, A. C., Sarro, L. M., Siopis, C., Smith, M., Sozzetti, A., Süveges, M., Torra, J., van Reeven, W., Abbas, U., Abreu Aramburu, A., Accart, S., Aerts, C., Altavilla, G., Álvarez, M. A., Alvarez, R., Alves, J., Anderson, R. I., Andrei, A. H., Anglada Varela, E., Antiche, E., Antoja, T., Arcay, B., Astraatmadja, T. L., Bach, N., Baker, S. G., Balaguer-Núñez, L., Balm, P., Barache, C., Barata, C., Barbato, D., Barblan, F., Barklem, P. S., Barrado, D., Barros, M., Barstow, M. A., Bartholomé Muñoz, S., Bassilana, J. L., Becciani, U., Bellazzini, M., Berihuete, A., Bertone, S., Bianchi, L., Bienaymé, O., Blanco-Cuaresma, S., Boch, T., Boeche, C., Bombrun, A., Borrachero, R., Bossini, D., Bouquillon, S., Bourda, G., Bragaglia, A., Bramante, L., Breddels, M. A., Bressan, A., Brouillet, N., Brüsemeister, T., Brugaletta, E., Bucciarelli, B., Burlacu, A., Busonero, D., Butkevich, A. G., Buzzi, R., Caffau, E., Cancelliere, R., Cannizzaro, G., Cantat-Gaudin, T., Carballo, R., Carlucci, T., Carrasco, J. M., Casamiquela, L., Castellani, M., Castro-Ginard, A., Charlot, P., Chemin, L., Chiavassa, A., Cocozza, G., Costigan, G., Cowell, S., Crifo, F., Crosta, M., Crowley, C., Cuypers, J., Dafonte, C., Damerdji, Y., Dapergolas, A., David, P., David, M., de Laverny, P. and De Luise, F. (2018). Gaia Data Release 2. Summary of the contents and survey properties, **616**: A1.

Gaia Collaboration, Brown, A. G. A., Vallenari, A., Prusti, T., de Bruijne, J. H. J., Mignard, F., Drimmel, R., Babusiaux, C., Bailer-Jones, C. A. L., Bastian, U., Biermann, M., Evans, D. W., Eyer, L., Jansen, F., Jordi, C., Katz, D., Klioner, S. A., Lammers, U., Lindegren, L., Luri, X., O'Mullane, W., Panem, C., Pourbaix, D., Randich, S., Sartoretti, P., Siddiqui, H. I., Soubiran, C., Valette, V., van Leeuwen, F., Walton, N. A., Aerts, C., Arenou, F., Cropper, M., Høg, E., Lattanzi, M. G., Grebel, E. K.,

Holland, A. D., Huc, C., Passot, X., Perryman, M., Bramante, L., Cacciari, C., Castañeda, J., Chaoul, L., Cheek, N., De Angeli, F., Fabricius, C., Guerra, R., Hernández, J., Jean-Antoine-Piccolo, A., Masana, E., Messineo, R., Mowlavi, N., Nienartowicz, K., Ordóñez-Blanco, D., Panuzzo, P., Portell, J., Richards, P. J., Riello, M., Seabroke, G. M., Tanga, P., Thévenin, F., Torra, J., Els, S. G., Gracia-Abril, G., Comoretto, G., Garcia-Reinaldos, M., Lock, T., Mercier, E., Altmann, M., Andrae, R., Astraatmadja, T. L., Bellas-Velidis, I., Benson, K., Berthier, J., Blomme, R., Busso, G., Carry, B., Cellino, A., Clementini, G., Cowell, S., Creevey, O., Cuypers, J., Davidson, M., De Ridder, J., de Torres, A., Delchambre, L., Dell'Oro, A., Ducourant, C., Frémat, Y., García-Torres, M., Gosset, E., Halbwachs, J. L., Hambly, N. C., Harrison, D. L., Hauser, M., Hestroffer, D., Hodgkin, S. T., Huckle, H. E., Hutton, A., Jasniewicz, G., Jordan, S., Kontizas, M., Korn, A. J., Lanzafame, A. C., Manteiga, M., Moitinho, A., Muinonen, K., Osinde, J., Pancino, E., Pauwels, T., Petit, J. M., Recio-Blanco, A., Robin, A. C., Sarro, L. M., Siopis, C., Smith, M., Smith, K. W., Sozzetti, A., Thuillot, W., van Reeven, W., Viala, Y., Abbas, U., Abreu Aramburu, A., Accart, S., Aguado, J. J., Allan, P. M., Allasia, W., Altavilla, G., Álvarez, M. A., Alves, J., Anderson, R. I., Andrei, A. H., Anglada Varela, E., Antiche, E., Antoja, T., Antón, S., Arcay, B., Bach, N., Baker, S. G., Balaguer-Núñez, L., Barache, C., Barata, C., Barbier, A., Barblan, F., Barrado y Navascués, D., Barros, M., Barstow, M. A., Becciani, U., Bellazzini, M., Bello García, A., Belokurov, V., Bendjoya, P., Berihuete, A., Bianchi, L., Bienaymé, O., Billebaud, F., Blagorodnova, N., Blanco-Cuaresma, S., Boch, T., Bombrun, A., Borrachero, R., Bouquillon, S., Bourda, G., Bouy, H., Bragaglia, A., Breddels, M. A., Brouillet, N., Brüsemeister, T., Bucciarelli, B., Burgess, P., Burgon, R., Burlacu, A., Busonero, D., Buzzi, R., Caffau, E., Cambras, J., Campbell, H., Cancelliere, R., Cantat-Gaudin, T., Carlucci, T., Carrasco, J. M., Castellani, M., Charlot, P., Charnas, J., Chiavassa, A., Clotet, M., Cocozza, G., Collins, R. S., Costigan, G., Crifo, F., Cross, N. J. G., Crosta, M., Crowley, C., Dafonte, C., Damerdji, Y., Dapergolas, A., David, P., David, M. and De Cat, P. (2016). Gaia Data Release 1. Summary of the astrometric, photometric, and survey properties, **595**: A2.

Gaia Collaboration, Vallenari, A., Brown, A. G. A., Prusti, T., de Bruijne, J. H. J., Arenou, F., Babusiaux, C., Biermann, M., Creevey, O. L., Ducourant, C., Evans, D. W., Eyer, L., Guerra, R., Hutton, A., Jordi, C., Klioner, S. A., Lammers, U. L., Lindegren, L., Luri, X., Mignard, F., Panem, C., Pourbaix, D., Randich, S., Sartoretti, P., Soubiran, C., Tanga, P., Walton, N. A., Bailer-Jones, C. A. L., Bastian, U., Drimmel, R., Jansen, F., Katz, D., Lattanzi, M. G., van Leeuwen, F., Bakker, J., Cacciari, C., Castañeda, J., De Angeli, F., Fabricius, C., Fouesneau, M., Frémat,

Y., Galluccio, L., Guerrier, A., Heiter, U., Masana, E., Messineo, R., Mowlavi, N., Nicolas, C., Nienartowicz, K., Pailler, F., Panuzzo, P., Riclet, F., Roux, W., Seabroke, G. M., Sordo, R., Thévenin, F., Gracia-Abril, G., Portell, J., Teyssier, D., Altmann, M., Andrae, R., Audard, M., Bellas-Velidis, I., Benson, K., Berthier, J., Blomme, R., Burgess, P. W., Busonero, D., Busso, G., Cánovas, H., Carry, B., Cellino, A., Cheek, N., Clementini, G., Damerdji, Y., Davidson, M., de Teodoro, P., Nuñez Campos, M., Delchambre, L., Dell'Oro, A., Esquej, P., Fernández-Hernández, J., Fraile, E., Garabato, D., García-Lario, P., Gosset, E., Haigron, R., Halbwachs, J. L., Hambly, N. C., Harrison, D. L., Hernández, J., Hestroffer, D., Hodgkin, S. T., Holl, B., Janßen, K., Jevardat de Fombelle, G., Jordan, S., Krone-Martins, A., Lanzafame, A. C., Löffler, W., Marchal, O., Marrese, P. M., Moitinho, A., Muinonen, K., Osborne, P., Pancino, E., Pauwels, T., Recio-Blanco, A., Reylé, C., Riello, M., Rimoldini, L., Roegiers, T., Rybizki, J., Sarro, L. M., Siopis, C., Smith, M., Sozzetti, A., Utrilla, E., van Leeuwen, M., Abbas, U., Ábrahám, P., Abreu Aramburu, A., Aerts, C., Aguado, J. J., Ajaj, M., Aldea-Montero, F., Altavilla, G., Álvarez, M. A., Alves, J., Anders, F., Anderson, R. I., Anglada Varela, E., Antoja, T., Baines, D., Baker, S. G., Balaguer-Núñez, L., Balbinot, E., Balog, Z., Barache, C., Barbato, D., Barros, M., Barstow, M. A., Bartolomé, S., Bassilana, J. L., Bauchet, N., Becciani, U., Bellazzini, M., Berihuete, A., Bernet, M., Bertone, S., Bianchi, L., Binnenfeld, A., Blanco-Cuaresma, S., Blazere, A., Boch, T., Bombrun, A., Bossini, D., Bouquillon, S., Bragaglia, A., Bramante, L., Breedt, E., Bressan, A., Brouillet, N., Brugaletta, E., Bucciarelli, B., Burlacu, A., Butkevich, A. G., Buzzi, R., Caffau, E., Cancelliere, R., Cantat-Gaudin, T., Carballo, R., Carlucci, T., Carnerero, M. I., Carrasco, J. M., Casamiquela, L., Castellani, M., Castro-Ginard, A., Chaoul, L., Charlot, P., Chemin, L., Chiaramida, V., Chiavassa, A., Chornay, N., Comoretto, G., Contursi, G., Cooper, W. J., Cornez, T., Cowell, S., Crifo, F., Cropper, M., Crosta, M., Crowley, C., Dafonte, C., Dapergolas, A., David, M., David, P., de Laverny, P., De Luise, F. and De March, R. (2023). Gaia Data Release 3. Summary of the content and survey properties, **674**: A1.

González-Cataldo, F. and Militzer, B. (2023). Ab initio determination of iron melting at terapascal pressures and Super-Earths core crystallization, *Physical Review Research* **5**(3): 033194.

Hakim, K., Rivoldini, A., Van Hoolst, T., Cottenier, S., Jaeken, J., Chust, T. and Steinle-Neumann, G. (2018). A new ab initio equation of state of hcp-Fe and its implication on the interior structure and mass-radius relations of rocky super-Earths, **313**: 61–78.

Haldemann, J., Dorn, C., Venturini, J., Alibert, Y. and Benz, W. (2024). BICEPS: An improved characterization model for low- and intermediate-mass exoplanets, **681**: A96.

Hara, N. C. and Ford, E. B. (2023). Statistical Methods for Exoplanet Detection with Radial Velocities, *Annual Review of Statistics and Its Application* **10**(1): 623–649.

Harrison, N. (2003). An introduction to density functional theory, *Nato Science Series Sub Series III Computer and Systems Sciences* **187**: 45–70.

Heller, R., Harre, J.-V. and Samadi, R. (2022). Transit least-squares survey. IV. Earth-like transiting planets expected from the PLATO mission, **665**: A11.

Henry, T. J. and Jao, W.-C. (2024). The Character of M Dwarfs, **62**(1): 593–633.

Hogg, D. W., Myers, A. D. and Bovy, J. (2010). Inferring the Eccentricity Distribution, **725**(2): 2166–2175.

Hohenberg, P. and Kohn, W. (1964). Inhomogeneous Electron Gas, *Physical Review* **136**(3B): 864–871.

Howard, S. and Guillot, T. (2023). Accounting for non-ideal mixing effects in the hydrogen-helium equation of state, **672**: L1.

Ichikawa, H. and Tsuchiya, T. (2020). Ab Initio Thermoelasticity of Liquid Iron-Nickel-Light Element Alloys, *Minerals* **10**(1): 59.

Iftimie, R., Minary, P. and Tuckerman, M. E. (2005). Chemical Theory and Computation Special Feature: Ab initio molecular dynamics: Concepts, recent developments, and future trends, *Proceedings of the National Academy of Science* **102**(19): 6654–6659.

Kallrath, J. (2009). *Eclipsing Binary Stars: Modeling and Analysis*.

Kite, E. S. and Ford, E. B. (2018). Habitability of Exoplanet Waterworlds, **864**(1): 75.

Kjeldsen, H. and Bedding, T. R. (1995). Amplitudes of stellar oscillations: the implications for asteroseismology., **293**: 87–106.

Kohn, W. and Sham, L. J. (1965). Self-Consistent Equations Including Exchange and Correlation Effects, *Physical Review* **140**(4A): 1133–1138.

Kresse, G. and Hafner, J. (1993). Ab initio molecular dynamics for liquid metals, **47**(1): 558–561.

Ligi, R., Creevey, O., Mourard, D., Crida, A., Lagrange, A. M., Nardetto, N., Perraut, K., Schultheis, M., Tallon-Bosc, I. and ten Brummelaar, T. (2016). Radii, masses, and ages of 18 bright stars using interferometry and new estimations of exoplanetary parameters, **586**: A94.

Lopez, E. D. and Fortney, J. J. (2014). Understanding the Mass-Radius Relation for Sub-neptunes: Radius as a Proxy for Composition, **792**(1): 1.

Lovis, C. and Fischer, D. (2010). Radial Velocity Techniques for Exoplanets, *in* S. Seager (ed.), *Exoplanets*, pp. 27–53.

Mao, H.-K., Chen, X.-J., Ding, Y., Li, B. and Wang, L. (2018). Solids, liquids, and gases under high pressure, *Reviews of Modern Physics* **90**(1): 015007.

Moe, M. and Kratter, K. M. (2021). Impact of binary stars on planet statistics - I. Planet occurrence rates and trends with stellar mass, **507**(3): 3593–3611.

Moya, A., Zuccarino, F., Chaplin, W. J. and Davies, G. R. (2018). Empirical Relations for the Accurate Estimation of Stellar Masses and Radii, **237**(2): 21.

Musella, R., Mazevet, S. and Guyot, F. (2019). Physical properties of MgO at deep planetary conditions, **99**(6): 064110.

Otegi, J. F., Dorn, C., Helled, R., Bouchy, F., Haldemann, J. and Alibert, Y. (2020). Impact of the measured parameters of exoplanets on the inferred internal structure, **640**: A135.

Perdew, J. P. and Zunger, A. (1981). Self-interaction correction to density-functional approximations for many-electron systems, **23**(10): 5048–5079.

Petricca, F., Castillo-Rogez, J. C., Genova, A., Melwani Daswani, M., Styczinski, M. J., Cochrane, C. J. and Vance, S. D. (2025). Partial differentiation of Europa and implications for the origin of materials in the Jupiter system, *Nature Astronomy* **9**: 501–511.

Plotnykov, M. and Valencia, D. (2024). Observation uncertainty effects on the precision of interior planetary parameters, **530**(3): 3488–3499.

Pourovskii, L. V., Mravlje, J., Ferrero, M., Parcollet, O. and Abrikosov, I. A. (2014). Impact of electronic correlations on the equation of state and transport in -Fe, **90**(15): 155120.

Radecka, M. W. and Rimmer, P. B. (2025). Nitrogen chemistry of hycean worlds on the example of K2-18b, .

Rice, D. R., Huang, C., Steffen, J. H. and Vazan, A. (2025). Uncertainties in the Inference of Internal Structure: The Case of TRAPPIST-1 f, **986**(1): 2.

Rigby, F. E. and Madhusudhan, N. (2024). On the ocean conditions of Hycean worlds, **529**(1): 409–424.

Rigby, F. E., Pica-Ciamarra, L., Holmberg, M., Madhusudhan, N., Constantinou, S., Schaefer, L., Deng, J., Lee, K. K. M. and Moses, J. I. (2024). Toward a Self-consistent Evaluation of Gas Dwarf Scenarios for Temperate Sub-Neptunes, **975**(1): 101.

Sakai, T., Dekura, H. and Hirao, N. (2016). Experimental and theoretical thermal equations of state of $MgSiO_3$ post-perovskite at multi-megabar pressures, *Scientific Reports* **6**: 22652.

Schwarz, K., Blaha, P. and Trickey, S. B. (2010). Electronic structure of solids with WIEN2k, *Molecular Physics* **108**(21-23): 3147–3166.

Schweitzer, A., Passegger, V. M., Cifuentes, C., Béjar, V. J. S., Cortés-Contreras, M., Caballero, J. A., del Burgo, C., Czesla, S., Kürster, M., Montes, D., Zapatero Osorio, M. R., Ribas, I., Reiners, A., Quirrenbach, A., Amado, P. J., Aceituno, J., Angladа-Escudé, G., Bauer, F. F., Dreizler, S., Jeffers, S. V., Guenther, E. W., Henning, T., Kaminski, A., Lafarga, M., Marfil, E., Morales, J. C., Schmitt, J. H. M. M., Seifert, W., Solano, E., Tabernero, H. M. and Zechmeister, M. (2019). The CARMENES search for exoplanets around M dwarfs. Different roads to radii and masses of the target stars, **625**: A68.

Seager, S., Kuchner, M., Hier-Majumder, C. A. and Militzer, B. (2007). Mass-Radius Relationships for Solid Exoplanets, **669**(2): 1279–1297.

Seager, S. and Mallén-Ornelas, G. (2003). A Unique Solution of Planet and Star Parameters from an Extrasolar Planet Transit Light Curve, **585**(2): 1038–1055.

Sotin, C., Grasset, O. and Mocquet, A. (2007). Mass radius curve for extrasolar Earth-like planets and ocean planets, **191**(1): 337–351.

Stassun, K. G., Collins, K. A. and Gaudi, B. S. (2017). Accurate Empirical Radii and Masses of Planets and Their Host Stars with Gaia Parallaxes, **153**(3): 136.

Stassun, K. G., Corsaro, E., Pepper, J. A. and Gaudi, B. S. (2018). Empirical Accurate Masses and Radii of Single Stars with TESS and Gaia, **155**(1): 22.

Stevens, D. J., Gaudi, B. S. and Stassun, K. G. (2018). Measuring Model-independent Masses and Radii of Single-lined Eclipsing Binaries: Analytic Precision Estimates, **862**(1): 53.

Sur, A., Su, Y., Tejada Arevalo, R., Chen, Y.-X. and Burrows, A. (2024). APPLE: An Evolution Code for Modeling Giant Planets, **971**(1): 104.

Tang, Y., Fortney, J. J., Nimmo, F., Thorngren, D., Ohno, K. and Murray-Clay, R. (2025). Reassessing Sub-Neptune Structure, Radii, and Thermal Evolution, **989**(1): 28.

Torres, G., Andersen, J. and Giménez, A. (2010). Accurate masses and radii of normal stars: modern results and applications, **18**(1-2): 67–126.

Unterborn, C. T., Desch, S. J., Haldemann, J., Lorenzo, A., Schulze, J. G., Hinkel, N. R. and Panero, W. R. (2023). The Nominal Ranges of Rocky Planet Masses, Radii, Surface Gravities, and Bulk Densities, **944**(1): 42.

Valencia, D., Sasselov, D. D. and O'Connell, R. J. (2007). Radius and Structure Models of the First Super-Earth Planet, **656**(1): 545–551.

van den Berg, A. P., Yuen, D. A., Umemoto, K., Jacobs, M. H. G. and Wentzcovitch, R. M. (2019). Mass-dependent dynamics of terrestrial exoplanets using ab initio mineral properties, **317**: 412–426.

Wentzcovitch, R. M. (1991). Invariant molecular-dynamics approach to structural phase transitions, **44**(5): 2358–2361.

Werlen, A., Dorn, C., Burn, R., Schlichting, H. E., Grimm, S. L. and Young, E. D. (2025). Sub-Neptunes Are Drier than They Seem: Rethinking the Origins of Water-rich Worlds, **991**(1): L16.

Westall, F. and Xiao, S. (2024). Precambrian Earth: Co-evolution of life and geodynamics, *Precambrian Research* **414**: 107589.

Winn, J. N. (2010). Exoplanet Transits and Occultations, *in* S. Seager (ed.), *Exoplanets*, pp. 55–77.

Zeng, L., Jacobsen, S. B., Sasselov, D. D., Petaev, M. I., Vanderburg, A., Lopez-Morales, M., Perez-Mercader, J., Mattsson, T. R., Li, G., Heising, M. Z., Bonomo, A. S., Damasso, M., Berger, T. A., Cao, H., Levi, A. and Wordsworth, R. D. (2019). Growth model interpretation of planet size distribution, *Proceedings of the National Academy of Science* **116**(20): 9723–9728.

Chapter 2

A Validated Low-to-Intermediate Mass Planetary Interior Structure Model and New Mass-Radius Relations

The content of this chapter is a draft of the manuscript text in preparation for publication under the following citation:

Skinner, B. N., Pudritz, R. E., Cloutier, R. 2025, Exoplanet Mass-Radius Relations Incorporating State-of-the-art Physics Validated on Solar System Objects. Submitted to The Astrophysical Journal September 24th, 2025.

Exoplanet Mass-Radius Relations Incorporating State-of-the-art Physics Validated on Solar System Objects

Bennett Neil Skinner
Physics & Astronomy
McMaster University, Hamilton, ON, Canada
Email: skinnb1@mcmaster.ca

Ralph Pudritz
Physics & Astronomy
McMaster University, Hamilton, ON, Canada
Email: pudritz@mcmaster.ca

Ryan Cloutier
Physics & Astronomy
McMaster University, Hamilton, ON, Canada
Email: ryan.cloutier@mcmaster.ca

Abstract

Clues on the formation history of exoplanets are embedded within their compositions. Forward models of the radii of planets with known masses and compositions can be compared against the observed exoplanet population to uncover these clues. We present a new interior structure model that includes state-of-the-art equations of state following the latest experimental and computational results, a physically-motivated mineralogy allowing multiple species to coexist within planetary layers, a temperature profile more realistic than adiabatic, melting, and other features. We validate this model by applying it to the seismographically-derived interior structures of Earth, the Moon, and Mars. Our model replicates the radii and moment of inertia coefficients of all three bodies to within 0.5%. Our model replicates Earth's radius to within 0.15%, the best of any similar model. We also validate on Venus, Mercury, and Europa and replicate radii and moment of inertia coefficients to within 1% or 3σ. We use

this new model to calculate mass-radius relationships for iron-rich, earth-like, water-rich, and H/He-enveloped planets with masses less than $100M_{\oplus}$, of particular use for determining the compositions of Earth-like planets, planets nearby the radius valley, and super-Mercuries. We fit power-laws to our results and find that the exponent in $M = aR^b$ increases with mass and core mass fraction. We find that phase transitions induce kinks in mass-radius relations. Our mass-radius curves are available at `https://github.com/Bennett-Skinner/SkinnerPudritzCloutier2025-MR-curves/`.

Keywords: *Exoplanet Structure (495), Planetary Structure (1255), Exoplanet Formation (492), Ocean Planets (1151), Mini Neptunes (1063), Super Earths (1655), Rocky planets (511), Computational Astronomy (293), Mantle (1005), Planetary Cores (1247), Planetary Interior (1248)*

2.1 Introduction

2.1.1 Interior Stucture Models

Observations of exoplanets give radii and mass and thus bulk densities. Understanding the populations of planets in the universe and constraining the predictions of planet formation theory require that these bulk densities are compared to planetary compositions. Doing so requires a planetary interior structure model, which solves for the internal density and temperature structure of a planet with known parameters (Sotin et al.; 2007; Seager et al.; 2007; Valencia et al.; 2007). Plots of the results of these models along curves with planets of uniform composition but varying mass can be compared to the observed exoplanet population to identify broad trends as well as quickly classify a newly discovered planet (Zeng et al.; 2019).

Many planetary interior structure models exist in the literature (e.g. Haldemann et al.; 2024; Unterborn et al.; 2023; Dorn et al.; 2017; Plotnykov and Valencia; 2024; Acuña et al.; 2021; Rice et al.; 2025; Aguichine et al.; 2025; Lopez and Fortney; 2014; van den Berg et al.; 2019; Boujibar et al.; 2020; Sur et al.; 2024; Zeng et al.; 2019). As is necessary for any model they include a number of simplifications about the interior structure of exoplanets. Often, planetary interiors are assumed to be made out of several differentiated layers, with each layer being composed of only a single species. This ignores the fact that Earth's mantle and core are both composed of multiple species, with the most important broad result being that Fe in Earth's mantle makes it denser and light elements in Earth's core make it less dense (Palme and O'Neill; 2014; McDonough; 2014).

Planet interiors are often assumed to be purely adiabatic, neglecting temperature jumps that occur at the top of the mantle and core in Earth's interior due to heat trapped from planet formation (Stixrude; 2014), making planets more dense. High-pressure phases of mantle materials predicted to occur beyond the pressures of Earth's mantle are neglected, making planets less dense (Umemoto et al.; 2017). Solid and liquid cores are often not included simultaneously, resulting in density overestimates if cores are assumed purely solid and underestimates if cores are assumed purely liquid (Rice et al.; 2025). Planetary radii are taken at the outer boundary of the model rather than at the $\tau = \frac{2}{3}$ optical depth of a grazing ray of light that exoplanet transit surveys probe, systematically increasing planetary radii compared to the 20 mbar radius and decreasing planetary radii compared to the 100 Pa radius (Haldemann et al.; 2024). Finally, older Equations of State are used that do not take into account recent experimental and computational advances or use poorly-extrapolating formulations (Hakim et al.; 2018). Importantly, these simplifications and others induce systematic changes in estimated radii, but these systematic changes are not all in the same direction. It is thus unclear a priori if the literature overestimates or underestimates planetary radii, necessitating the construction of a model that relaxes all of the assumptions discussed here and more. That model is the subject of this work.

The major task accomplished in this paper is to greatly improve preexisting interior structure models along four main axes: new equations of state (e.g. Hakim et al.; 2018; Howard and Guillot; 2023; Haldemann et al.; 2020), a less simplified mineralogy (e.g. Stixrude and Lithgow-Bertelloni; 2024), the inclusion of additional phase changes (e.g. Dorogokupets et al.; 2017; Umemoto et al.; 2017), and a more physical thermal structure (e.g. Parmentier et al.; 2015; Parmentier and Guillot; 2014; Stixrude; 2014).

Planetary interior structure models must be benchmarked against planets for which we have non-interior-structure-model constraints on their interiors to verify their accuracy. The literature typically performs this benchmark on Earth. We expand this framework by benchmarking our model against Mercury, Venus, Earth, the Moon, Mars, and Europa.

2.1.2 Exoplanet Applications Requiring Updated Interior Structure Models

One of the most striking planet demographics findings of the past decade has been the discovery of the bimodality of the radii of planets in close-in orbits referred to as the Radius Valley (Fulton et al.; 2017; Fulton and Petigura; 2018; Cloutier and Menou; 2020).

The lower radii super-Earth peak is composed of planets with densities consistent with Earth-like compositions, while the higher radii sub-Neptune peak is composed of planets with lower bulk densities, implying a significant inventory of a lower-density substance, either H/He or water (Dressing et al.; 2015; Rogers; 2015).

A relatively small mass fraction of H/He or a relatively large mass fraction of water would produce similar bulk densities, so observations of planetary masses and radii alone are insufficient to distinguish between H/He-enveloped and water-rich sub-Neptunes on an individual level (Miller-Ricci et al.; 2009; Dressing et al.; 2015; Rogers; 2015). A population-level study would require extreme precision in planetary radii, as the degeneracy in H/He-enveloped and water-rich planetary radii means that even a %-level inaccuracy in the planetary interior structure model can dramatically alter the difference in radii between a H/He-enveloped and water-rich planet of the same mass.

If the lower-density substance is H/He, the radius valley separates planets that have retained a primordial H/He envelope from those that have lost a primordial H/He envelope via mass loss driven by either stellar X-ray and UV radiation, residual heat in the planetary core, or some combination of the two (Owen and Wu; 2013; Lopez and Fortney; 2014; Lopez and Rice; 2018; Gupta and Schlichting; 2019; Owen and Schlichting; 2024). If the lower-density substance is water, the radius valley separates planets that accreted nearly all their material within the iceline and thus never acquired much water from those that accreted a significant mass fraction of water outside the iceline and subsequently migrated inwards (Venturini et al.; 2020, 2024; Izidoro et al.; 2022; Chakrabarty and Mulders; 2024). Around sun-like stars, the positive slope of the location of the radius valley with instellation (Van Eylen et al.; 2018; Martinez et al.; 2019) and its weakening in very young systems have been used as observational evidence for the prevalence of mass loss of H/He envelopes (Christiansen et al.; 2023; Vach et al.; 2024; Fernandes et al.; 2025). However, the radius-instellation slope of the radius valley reverses around M Dwarf stars, potentially indicating the prevalence of inwards-migrating water worlds (Cloutier and Menou; 2020).

Another quandary is presented by Super-Mercuries, planets with much higher densities for their masses than Earth implying formation either via giant impact (e.g. Scora et al.; 2020, 2022) or condensation at high temperatures (e.g. Dorn et al.; 2019). Two super-Mercuries–GJ 367 b and K2-229 b–have bulk densities near that of a pure iron planet of their size, causing even relatively minor changes in modeled radii to draw planets much closer to or further from consistent with pure iron (Adams et al.; 2021; Dai

et al.; 2019; Goffo et al.; 2023). These planets also serve as a lower radius limit that interior structure models must account for.

This paper is structured as follows: in Section 2.2 we describe our new interior structure model in physical detail. The general reader interested only in the results may first read subections 2.2.1 and 2.2.10 for an overview and then skip to Section 2.3 where we compare our model to the observed interior structures of solar system objects for validation. Section 2.4 presents our new isocomposition mass-radius curves and in Section 2.5 we compare our model to empirical mass-radius relations, compare the assumptions of our model to those in the literature, and discuss the implications of missing physics. Finally, Section 2.6 summarizes our results and looks towards future work.

2.2 A New Interior Structure Model

A list of all parameters input into our interior structure model is given in Table 2.1.

2.2.1 Overview and Key Assumptions

We employ the standard assumption that planets are objects in hydrostatic equilibrium composed of multiple layers each with a homogeneous elemental composition, although not necessarily homogeneous in chemical composition or phase. These layers–from the outermost layers of a planet to its core–are 1) a H/He envelope, 2) a pure water layer, 3) a mantle composed of FeO, SiO_2, MgO and minerals formed from the combination of those endmembers (most prominently $MgSiO_3$), 4) a liquid core composed of Fe, S, and O, and 5) a solid core composed of Fe and S. The envelope, water, mantle, and total core mass fractions are set a priori while the size of the liquid and solid core are determined by solving the standard equations of planetary structure below.

We calculate a planet's structure following the three ordinary differential equations: mass conservation

$$\frac{\partial r}{\partial m} = \frac{1}{4\pi r^2 \rho(P,T)}, \tag{2.1}$$

hydrostatic equilibrium

$$\frac{\partial P}{\partial m} = -\frac{Gm}{4\pi r^2}, \tag{2.2}$$

and thermal transport

$$\frac{\partial T}{\partial m} = \frac{\partial P}{\partial m}\frac{T}{P}\nabla, \tag{2.3}$$

Variable	Parameter	Source
$m_{\rm p}$	Planet mass	Independent Variable
$F_{\rm p}$	Planet instellation	Independent Variable
$w_{\rm H/He}$	Envelope mass fraction	Independent Variable
$w_{\rm H_2O}$	Water mass fraction	Independent Variable
$w_{\rm mantle}$	Mantle mass fraction	Independent Variable
$w_{\rm core}$	Core mass fraction	Independent Variable
$x^s_{\rm Fe}$	Fe molar mass fraction in solid core	Independent Variable ($x^s_{\rm Fe,\oplus} = 0.885$)
$x^s_{\rm S}$	S molar mass fraction in solid core	Independent Variable ($x^s_{\rm S,\oplus} = 0.115$)
$x^l_{\rm Fe}$	Fe molar mass fraction in liquid core	Independent Variable ($x^l_{\rm Fe,\oplus} = 0.83$)
$x^l_{\rm S}$	S molar mass fraction in liquid core	Independent Variable ($x^l_{\rm S,\oplus} = 0.09$)
$x^l_{\rm O}$	FeO molar mass fraction in liquid core	Independent Variable ($x^l_{\rm O,\oplus} = 0.08$)
$x_{\rm MgO}$	MgO endmember molar mass fraction in mantle	Independent Variable ($x_{\rm MgO,\oplus} = 0.512$)
$x_{\rm SiO_2}$	SiO_2 endmember molar mass fraction in mantle	Independent Variable ($x_{\rm SiO_2,\oplus} = 0.425$)
$x_{\rm FeO}$	FeO endmember molar mass fraction in mantle	Independent Variable ($x_{\rm FeO,\oplus} = 0.063$)
$x_{\rm H}$	H molar mass fraction in envelope	Set as solar (0.725)
$x_{\rm He}$	He molar mass fraction in envelope	Set as solar (0.275)
t	Age of planet	Set as Earth-like (4.5 Gyr)
A_B	Bond Albedo of planet	Set as Earth-like (0.3)
$T_{\rm eff}$	Stellar Effective Temperature	Set as sun-like (6000 K)
$Z_{\rm Atm}$	Atmospheric metallicity	Set following observations ($50Z_\odot$)
$P_{\rm rot}$	Rotation period of planet	Effect set to zero ($P_{\rm rot} = \infty$)

TABLE 2.1: All parameters input into the interior structure model. Note the restrictions $w_{\rm H/He} + w_{\rm H_2O} + w_{\rm mantle} + w_{\rm ccore} = 1$, $x_{\rm H} + x_{\rm He} = 1$, $x_{\rm MgO} + x_{\rm SiO_2} + x_{\rm FeO} = 1$, $x^s_{\rm Fe} + x^s_{\rm FeS} = 1$, and $x^l_{\rm Fe} + x^l_{\rm FeS} + x^l_{\rm FeO} = 1$, reducing the number of free parameters by 5 from the total number of variables. In total, our model has 16 free parameters, 5 of which we vary in our generation of mass-radius curves, 5 of which are varied but generally set to be Earth-like, 4 of which we hold to solar or Earth values, 1 of which we set following exoplanet observations, and 1 of which is excluded outside the validation sample. We emphasize that all parameters can be freely varied within our framework.

where $r(m)$ is the distance from the planetary center at which the variables are evaluated, m is the enclosed mass, $\rho(P,T)$ is the density, $P(m)$ is pressure, $T(m)$ is temperature, G is the gravitational constant, and $\nabla \equiv \frac{P}{T}\frac{\partial T}{\partial P}$ is the dimensionless temperature gradient (Prialnik; 2009).

Our boundary conditions are the pressure, temperature, and radius of the planet at its center and outermost layer (set as $P_{\text{out}} = 100$ Pa throughout this work, not to be confused with the condensed surface of the planet). At the core of the planet, $r(0) = 0$ is known, while at the surface of the planet, $P(r_{\text{out}}) = P_{\text{out}}$ and $T(r_{\text{out}}) = T_{\text{eff}}$ are known, where P_{out} is a small pressure representing the edge of the planet, T_{eff} is the effective surface temperature of the planet. As not all three dependent variables are known at the same location, we guess the unknown variables at the surface and core, then integrate the ODEs from the surface inward and the core outward simultaneously to some m_{fit}, a location within the planet at which the inwards and outwards integration meet that carries no physical meaning. If the values of $r(m_{\text{fit}})$, $P(m_{\text{fit}})$, and $T(m_{\text{fit}})$ are similar for the surface inward and core outward integrations, then our guesses were correct. Guesses are iterated via the Newton-Raphson method (Press et al.; 1996). We seed initial guesses by the Zeng et al. (2019) parametric fit to planetary radii. We integrate using the Cash-Karp Runge-Kutta method, a fifth-order Runge-Kutta scheme in which step sizes are adaptively varied to keep error–estimated by comparing fifth-and fourth-order solutions– below a chosen threshold (Press et al.; 1996). Numerical details are provided in Section A3.

We make the assumption (with the exception of the low-pressure mantle region covered by HeFESTo, see Section 2.2.5) that all species are solely in one phase at a given pressure and temperature, even though in reality some phases may coexist. We justify this assumption by the already imprecise nature of many of the phase transitions of interest. If lower-density phases coexist with higher-pressure phases beyond where we expect a phase transition to occur, our model tends to overestimate densities, conversely, if higher-density phases coexist with lower-density phases below where we expect a phase transition to occur, our model tends to underestimate densities.

Our assumption of an Earth-like inventory of mantle and core elements is justified by the relatively consistent midplane temperatures in the protoplanetary disks of Sun-like stars. This results in Mg, Si, and Fe almost universally condensing at the radii where planets are formed, causing planets to inherit abundance ratios from their host stars, which themselves exhibit relatively minor abundance deviations (Unterborn et al.; 2020; Hinkel et al.; 2014; Bedell et al.; 2018). Indeed, measurements of the chemical

composition of polluted white dwarf atmospheres assumed to come from the infall of exoplanetary material indicate Earth-like compositions (e.g. Doyle et al.; 2019). We emphasize that our model only assumes an Earth-like inventory of elements and that the relative abundances of MgO, SiO_2, and FeO in the mantle and Fe, FeS, and FeO in the core can be freely varied.

Measurements of Earth's bulk mantle composition from mid-ocean ridge basalts indicate that the end members that we include compose $\gtrsim 90\%$ of Earth's mantle, further justifying our simplification of the mantle to those components (Workman and Hart; 2005). Al_2O_3 and CaO comprise the largest fraction of missing materials from our model in the case of Earth, however our (see Section 2.3.1) and other interior structure models represent Earth well without them (Workman and Hart; 2005; Unterborn et al.; 2020). Carbon may constitute a more significant component in exoplanetary systems than our own and is the subject of future work (Lin and Seager; 2025; Li et al.; 2025; Bergin et al.; 2023).

Our core inventory is slightly less complete, with greater than 85% of the weight of Earth's core being Fe, O, or S, with Fe being by far the most abundant element (McDonough; 2014). Ni and/or Si likely represent much of the remainder of the core but we justify their exclusion by (1) our good match to observations within the Solar System discussed in Section 2.3, (2) Mars' core being much more S-rich than Earth's indicating a diversity in core S compositions (Gendre et al.; 2022; Le Maistre et al.; 2023), and (3) the possibility of FeS enhancement in planetary cores as mantle materials oxidize the core, removing bare Fe from the core while oxidation-protected FeS is relatively enhanced in the remaining core (e.g Johansen et al.; 2023). The inclusion of lower-density materials within the core reduces its bulk density and thus previous models assuming pure Fe cores underpredict core radii, especially when those cores are assumed to be purely solid rather than at least partially liquid, as is the case for Earth (Unterborn et al.; 2020).

In addition to these compositional layers, the planet is divided into an irradiated outermost atmospheric layer (atmosphere) that receives all incident stellar flux and an interior layer that receives no stellar flux. The outermost layer has a temperature profile following the radiative transfer results of Parmentier and Guillot (2014); Parmentier et al. (2015), while the interior layer has a temperature profile that is radiative or adiabatic.

In section 2.2.2 we provide background on the forms of equations of state (EOS) used in our model. In sections 2.2.3-2.2.6, we discuss the mineralogy, phases, and EOS used in

our model, from the H/He envelope down to the core. In sections 2.2.7-2.2.9, we discuss further details of the model.

2.2.2 Equations of State

Equations Of State (EOS) are thermodynamic equations that relate the properties of a substance, with the relevant properties in our formalism being pressure P, temperature T, density ρ, and entropy S (necessary for calculating $\nabla_{\rm ad}$, see Section 2.2.2.4), i.e EOS give $\rho(P,T)$ and $S(P,T)$. They are thus necessary to calculate Equations 2.1 and 2.3. The entirety of any planetary interior structure model thus hinges on EOS, which we now give a brief overview of before discussing the particular EOS we use in Sections 2.2.3-2.2.6.

In the majority of EOS used, V instead of ρ is the variable related to the size of the substance, giving the volume of a mole of that material. V can be converted to ρ via $V = \frac{M}{\rho}$ where M is the molar mass of the material. EOS can either be provided as tables in a publication or fit to one of several equations. All fit EOS have Helmholtz free energies composed of an isothermal term (i.e $\rho(P)$, $S(P)$) and up to two temperature-dependent terms, with the first related to harmonic oscillations in the material and the second related to anharmonic oscillations and electrons (i.e $\rho(P,T)$, $S(P,T)$), whose forms we discuss in Sections 2.2.2.1 2.2.2.2, and 2.2.2.3, respectively. The thermal and anharmonic/electronic pressures are generally (but not universally) positive, so neglecting them leads to lower pressures at similar densities than would otherwise be calculated. As we calculate densities from pressures, this results in a bias towards higher densities. Intuitively, ignoring these terms ignores thermal expansion, resulting in higher densities (for example, our reference Earth's radius decreases by 0.04% if the mantle EOS is always calculated using $T = 300$ K).

We will provide the functional forms of all EOS used and a brief description of the physics used to derive them, for full derivations the reader is directed towards the references provided. The purpose of this overview is to give the reader an intuition for where our EOS arise and over what pressure ranges certain EOS are appropriate, justifying the EOS forms we employ in our model as discussed in Sections 2.2.3-2.2.6.

When discussing phase transitions, we use in this publication the subscript notation $X^{Y}_{Z_1/Z_2}$, where X is P or T, Y is the material and Z_1 and Z_2 are the higher and lower-pressure phases (even if X is T), respectively.

2.2.2.1 Isothermal EOS

The third-order finite strain Birch-Murnagham (BM3) EOS formulation given by Eq. 2.4 is derived by expanding a material's Helmholtz free energy in terms of the change in surface area of a compressed cube (Murnaghan; 1937, 1944; Birch; 1947; Katsura and Tange; 2019).

$$P = \frac{3}{2}K_0\left[\left(\frac{\rho}{\rho_0}\right)^{\frac{7}{3}} - \left(\frac{\rho}{\rho_0}\right)^{\frac{5}{3}}\right]\left[1 + \frac{3}{4}(K_0' - 4)\left(\left(\frac{\rho}{\rho_0}\right)^{\frac{2}{3}} - 1\right)\right], \tag{2.4}$$

where ρ_0, K_0, and K_0' are fitting constants representing the density in fiducial conditions, the isothermal bulk modulus (K_T) at reference conditions, and its pressure derivative, respectively.

The Rose-Vinet[1] formulation of Eq. 2.5 is derived by taking the volume derivative of the Helmholtz free energy of a Rydberg potential, an approximation of atomic binding energies (Rose et al.; 1983; Vinet et al.; 1987; Rydberg; 1932; Holzapfel; 2002).

$$P = 3K_0(\frac{\rho}{\rho_0})^{\frac{2}{3}}(1 - (\frac{\rho}{\rho_0})^{-\frac{1}{3}})e^{\frac{3}{2}(K_0'-1)(1-(\frac{\rho}{\rho_0})^{-\frac{1}{3}})} \tag{2.5}$$

The Holzapfel formulation of Eq. 2.6 is derived by modifying the Rose-Vinet equation such that it matches the high-compression free-electron Fermi gas limit (i.e K' approaches $\frac{5}{3}$ as pressure approaches ∞) while remaining integrable in closed form (Holzapfel; 1996, 1998, 2002; Hakim et al.; 2018).

$$P = 3K_0(\frac{\rho}{\rho_0})^{\frac{5}{3}}(1 - (\frac{\rho}{\rho_0})^{-\frac{1}{3}})e^{c_0(1-(\frac{\rho}{\rho_0})^{-\frac{1}{3}})} \cdot (1 + (\frac{\rho}{\rho_0})^{-\frac{1}{3}}c_2(\frac{\rho}{\rho_0})^{-\frac{1}{3}}), \tag{2.6}$$

where c_0 and c_2 are fitting constants. All fitting constants are derived via simulation or experimentation.

The Keane formulation of Eq. 2.7 is a consequence of Keane's rule, which states that the pressure derivatives of the bulk modulus at zero pressure, K_0', and infinite pressure, K_∞', must satisfy $\frac{K_0'}{2} < K_\infty' < K_0' - 1$ (Stacey and Davis; 2004; Keane; 1954; Sakai et al.; 2016). The Keane formulation is only used in one EOS in our sample, where it lies between the BM3 and Rose-Vinet equations and is the best fit to the data up to 300 GPa among those three (Sakai et al.; 2016).

[1]Synonymous with Vinet or Vinet-Rydberg.

$$P = K_0 \frac{K_0'}{{K_\infty'}^2}((\frac{V_0}{V})^{K'_\infty} - 1) - (\frac{K_0'}{K_\infty'} - 1)\ln(\frac{V_0}{V}) \tag{2.7}$$

BM3 is valid for $\lesssim$ 200 GPa, Rose-Vinet for $\lesssim 10^3$ GPa, and Holzapfel is valid up to pressures of $\gtrsim 10^4$ GPa (Hama and Suito; 1996; Cohen et al.; 2000; Seager et al.; 2007; Hakim et al.; 2018). BM3 or Rose-Vinet EOS are thus not applicable to the high-pressure interiors of super-Earths or sub-Neptunes, motivating the necessity of EOS updates. Although the Holzapfel EOS has the best high pressure limit, we caution that the Rose-Vinet EOS has been found to match experiments better at lower pressures, motivating an approach as considered here where the Holzapfel EOS is applied only to the highest pressure phases (Hama and Suito; 1996; Cohen et al.; 2000).

We note that all of these EOS are of the form $P(\rho)$ while we desire $\rho(P)$. We generated tables of these EOS in the desired form using the Newton-Raphson method of iteration and interpolated over these tables while running our interior structure model to save the computational expense of repeated iteration.

2.2.2.2 Thermal Contributions to the EOS

The temperature-dependent portion of the EOS is itself split into two parts, a quasi-harmonic contribution and an anharmonic and/or electronic contribution.

All quasi-harmonic contributions to the EOS considered here arise from the Mie–Grüneisen framework of Eq. 2.8, where Δ is the change between a temperature T and some reference temperature T_0 and γ_{th} is the thermal Grüneisen parameter (Mie; 1903; Grüneisen; 1912; Goodstein; 1985; Poirier; 2000; Heuzé; 2012). The EOS formulations differ in their expressions for E_{th}.

$$\Delta P_{th} = \gamma_{th} \frac{\Delta E_{th}}{V} \tag{2.8}$$

In the Einstein Model, a material is made up of simple harmonic oscillators vibrating at some characteristic frequency ω_E corresponding to a characteristic temperature $\theta_E = \frac{\hbar\omega_E}{k_B}$ and the resulting partition function is used to derive an energy as shown in Eq. 2.9 (Einstein; 1906; Goodstein; 1985; Poirier; 2000)[2].

$$E = 3nR(\frac{\theta_E}{e^{\frac{\theta_E}{T}} - 1}) \tag{2.9}$$

[2]This expression leaves out the zero-point energy, which makes no difference on the final result as we are only concerned with ΔE, not its absolute value.

In the Debye model, rather than assuming a uniform characteristic frequency, all frequencies below some frequency ω_D corresponding to a temperature $\theta_D = \frac{\hbar\omega_D}{k_B}$ contribute to the internal energy of the material (Debye; 1912; Goodstein; 1985; Poirier; 2000). The total internal energy is then an integral in frequency space of the energy per oscillator per mode, $\hbar\omega$, times the density of modes $g(\omega)$, times the number of quanta of vibration occupying that mode (phonons, c.f photons with $E = \hbar\omega$), resulting in Eq. 2.10 (Debye; 1912; Goodstein; 1985; Poirier; 2000).

$$\begin{aligned} E &= \int_0^{\omega_D} < n > \hbar\omega g(\omega) d\omega \\ &= 9nRT\frac{\gamma_{th}}{V}(\frac{T}{\theta_D})^3 \int_0^{\frac{\theta_D}{T}} \frac{x^3}{e^x - 1} dx \end{aligned} \tag{2.10}$$

At $T >>> \theta_D$, the entire portion of Eq. 2.10 to the right of $\frac{\gamma_{th}}{V}$ (also known as the Debye Function) approaches a limit of $\frac{1}{3}$, so the Debye EOS can be re-expressed in the Linear form of Eq. 2.11 (Ichikawa et al.; 2014; Ichikawa and Tsuchiya; 2020; Kuwayama et al.; 2020).

$$E = 3nRT \tag{2.11}$$

The three formulations converge at higher temperatures, with the Debye and Einstein models in agreement for $T >> \theta_D$ and at even higher temperatures all energies converging to Eq. 2.11, as can be derived by Taylor expanding $e^{\frac{\theta_D}{T}}$ in Eq. 2.9 (Dorogokupets; 2010).

Thus, as one goes from the Debye model of Eq. 2.10 to the Einstein model of Eq. 2.9 to the Linear model of Eq. 2.11, the complexity of the equation decreases at the cost of a worse representation of reality, with this cost decreasing at higher temperatures.

If θ_D and θ_E were constant, the model would be harmonic; however, as a material compresses, its characteristic temperature θ_D changes, hence the "quasi-" in quasi-harmonic (Anderson; 2005). Under the quasi-harmonic approximation used in all EOS considered here θ_D has no temperature dependence (Anderson; 2005). The parameter γ_{th} thus has a physical interpretation as indicating the change in θ_D with volume, which can be combined with Eq. 2.8 to express γ_{th} in terms of the constant volume heat capacity C_V, the thermal expansion coefficient α, and K_T, as in Eq. 2.12 (Grüneisen; 1912; Poirier; 2000; Anderson; 2005). Note that the three definitions of γ_{th} are only fully equivalent if the Mie–Grüneisen EOS is valid and can vary by up to tens of % in low-density,

high-temperature environments (Oganov and Dorogokupets; 2004).

$$\gamma_{th} = \frac{P_{th}}{E_{th}}V = -\frac{d(\ln(\theta))}{d(\ln(V))} = \frac{\alpha V K_T}{C_V} \tag{2.12}$$

The volume dependence of γ_{th} has been theoretically shown in the Thomas-Fermi atom to approach a constant at low volumes and experimentally determined to follow a power law at higher volumes (Gilvarry; 1956; Boehler and Ramakrishnan; 1980), leading to the Al'tshuler form of γ_{th} of Eq. 2.13 (Al'tshuler et al.; 1987).

$$\gamma_{th} = \gamma_\infty + (\gamma_0 - \gamma_\infty)(\frac{V}{V_0})^\beta \tag{2.13}$$

For many materials under Earth-like conditions, $\gamma_\infty \to 0$, leading to an assumption of $\gamma_\infty = 0$ or in some cases $\beta \approx 1$, resulting in a constant γ assumption (Anderson; 1979). Al'tshuler et al. (1987)'s original form had $\beta \equiv (\gamma_0)/(\gamma_0 - \gamma_\infty)$, but most of the EOS used here treat β as a free parameter. As one moves from a fixed γ to $\gamma_\infty = 0$ to the Al'tshuler Form to the Al'tshuler Form (Varied β), one increases the number of free parameters. This can result in a better fit to the data, but risks overfitting, especially as the number of free parameters approaches the order of magnitude of the number of datapoints.

In any case, the definition of γ_{th} in Eq. 2.12 combined with Eq. 2.13 leads to a formulation for θ_D or θ_E (numerically, $\theta_E \approx 0.75\theta_D$, so scaling laws that apply to one apply to both (Anderson; 2019)) presented in Eq. 2.14.

$$\theta_D = \theta_0(\frac{V}{V_0})^{-\gamma_\infty} \exp(\frac{\gamma_0 - \gamma_\infty}{\beta}(1 - (\frac{V}{V_0})^\beta)) \tag{2.14}$$

Despite the numerous approximations used in the derivation of the thermal energy, the fact that thermodynamic properties are integrals over an entire spectrum of vibrational states makes them relatively insensitive to the exact form of the spectrum, explaining the good agreement between this simplified theory, experiment, and the properties of Earth's interior (Stixrude and Lithgow-Bertelloni; 2005).

2.2.2.3 Anharmonic and Electronic EOS

Real material structures are not composed solely of harmonic oscillators; application of perturbation theory to the potential of a weakly anharmonic oscillator in the high-temperature limit reveals an additional contribution to the internal energy proportional

to T^2 (Oganov and Dorogokupets; 2004; Dewaele et al.; 2006). Electrons within the structure contribute an additional energy term; solving the Thomas-Fermi model for the electrons in an atom results in a contribution to the internal energy proportional to T^2 (Thomas; 1927; Fermi; 1928; Gilvarry; 1954a,b; Al'Tshuler et al.; 1960). Experimental data reveals that the electronic energy varies with $\frac{V}{V_0}$ to a constant power (Al'Tshuler et al.; 1960; Gilvarry; 1956; Latter; 1955). Similarly, the anharmonic energy varies with $\frac{V}{V_0}$ to a constant power, decreasing with pressure (and thus increasing with V) (Oganov; 2015; Oganov and Dorogokupets; 2004; Zharkov and Kalinin; 1971).

As anharmonic and electronic contributions to internal energy have identical temperature scaling, all EOS of interest in this paper combine them into one term or use a formulation involving only an electronic or anharmonic term but not the other(Belonoshko et al.; 2008; Bouchet et al.; 2013). Although the volume scaling of the electronic and anharmonic terms can differ, the impact is minor enough that this complication does not affect the quality of the fit (Belonoshko et al.; 2008; Bouchet et al.; 2013). The anharmonic-electronic internal energy is thus given in Eq. 2.15[3], with e_0 and g being fit terms.

$$E_{ae} = \frac{3}{2} n R e_0 (\frac{V}{V_0})^g T^2 \tag{2.15}$$

Eq. 2.8 is not valid for these non quasi-harmonic terms and pressure is instead derived via the thermodynamic relation $P = -(\frac{\partial F}{\partial V})_T$ for a volume-independent S, resulting in Eq. 2.16[4] (Dorogokupets et al.; 2017; Oganov; 2015; Al'Tshuler et al.; 1960).

$$P_{ae} = \frac{3R}{2V} n e_0 g (\frac{V}{V_0})^g T^2 \tag{2.16}$$

Having determined the temperature dependence of the EOS, the entropy S of a material can be determined via Eq. 2.17.

$$S = \int_0^T \frac{\frac{dE}{dT'}}{T'} dT' \tag{2.17}$$

2.2.2.4 Multiple Species in a Layer: Combining EOS

When multiple species are present in one layer, their EOS are combined using the fact that the extensive variables (V, the volume of a mole of a substance, and S, entropy, in this framework) of different substances add for constant intensive variables (P and T)

[3]Bouchet et al. (2013); Musella et al. (2019) absorb n into e_0

[4]See Footnote 3

(Fontaine et al.; 1977; Saumon et al.; 1995), as expressed in Eq. 2.18,

$$X = \sum_{i=1}^{N} x_i X_i, \tag{2.18}$$

where X is some extensive property and X_i is that extensive property for some species i comprising a molar fraction fraction x_i of the mixed material[5]. Although Eq. 2.18 is only strictly valid for ideal gases, Eq. 2.18 has been experimentally verified up to 3 TPa and computationally verified for Earth's core (Bradley et al.; 2018; Umemoto and Hirose; 2020; Huang et al.; 2019).

We apply Eq. 2.18 directly for S, but in the case of V, we desire the density rather than specific volume of substances. We convert between the two using the molar mass of the species, which yields Eq. 2.19 for ρ.

$$\rho = \left(\sum_{i=1}^{N} \frac{w_i}{\rho_i} \right)^{-1} \tag{2.19}$$

Having determined S, we calculate the adiabatic gradient via Eq. 2.20, a consequence of the definition of $\nabla_{\rm ad}$ used here and setting $dS = 0$ in $dS = (\frac{\partial S}{\partial T})_P dT + (\frac{\partial S}{\partial P})_T dP$. Note that $\nabla_{\rm ad}$ is not extensive and thus Eq. 2.18 does not directly apply to $\nabla_{\rm ad}$ (Saumon et al.; 1995).

$$\nabla_{\rm ad} \equiv (\frac{\partial \log T}{\partial \log P})_S = -\frac{(\frac{\partial \log S}{\partial \log P})_T}{(\frac{\partial \log S}{\partial \log T})_P} \tag{2.20}$$

In the specific case of the liquid core EOS provided by Ichikawa and Tsuchiya (2020); Kuwayama et al. (2020), the simplification of Eq. 2.11 forces $(\frac{\partial \log (T)}{\partial \log (P)})_S = 0$ and thus $\nabla_{\rm ad} = 0$, even though $\nabla {\rm ad} \neq 0$. For the liquid mantle, we instead calculate $\nabla_{\rm ad}$ using α, K_T, and C_V. $\alpha \equiv \frac{1}{V}(\frac{\partial V}{\partial T})_P$ and $K_T \equiv -V(\frac{\partial P}{\partial V})_T$ are determined by numerically differentiating our EOS, $c_V \equiv (\frac{\partial E}{\partial T})_V$ is determined by taking derivatives of Equations 2.9-2.11 Anderson (2005); Glasser (2013). Combining the rightmost definition of γ_{th} in Eq. 2.12 with the thermodynamic relations and Eq. 2.20 yields Eq. 2.21 (Stacey and Hodgkinson; 2019; Hakim et al.; 2018; Haldemann et al.; 2024).

$$\nabla_{\rm ad} = \frac{\gamma_{th} P}{K_T(1 + \alpha \gamma_{th} T)} = \frac{\alpha V P}{C_V + \alpha^2 V K_T T} \tag{2.21}$$

[5]Chabrier et al. (2019) use w_i instead of x_i, this is because all of their properties are not extensive but rather extensive variables per unit mass. Converting their variables back into extensive variables would involve multiplying by their masses, changing x_i into w_i.

The values of α, C_V, and K_T for a mixture are derived using Eq. 2.18, which applies directly to C_V (Ita and Stixrude; 1992), αV, and $\frac{V}{K_T}$, with V calculated from dividing the sum of molar weights of a substance by ρ from Eq. 2.19 (Stixrude and Lithgow-Bertelloni; 2005, 2011). We also use 2.21 for the high-pressure mantle, for which we have tabular values of α, C_V, and K_T but no functional form (Tsuchiya and Tsuchiya; 2011; Umemoto and Wentzcovitch; 2011; Umemoto et al.; 2017).

As a final contrast between the EOS used for the liquid core and the other EOS used in this publication, the Mie-Grüneisen model is assumed to apply to all T-dependent terms in Xie et al. (2025); Ichikawa and Tsuchiya (2020); Kuwayama et al. (2020) rather than just the quasi-harmonic term, i.e $\Delta(P_{th} + P_{ae}) = \gamma_{th}\frac{\Delta(E_{th}+E_{ae})}{V}$ rather than the form of Eq. 2.8.

We calculate the melting temperature of a layer that is composed of multiple species by modifying the melting temperature of the dominant species in that layer following Stixrude (2014) via Eq. 2.22[6],

$$T_m^{layer} = \frac{T_m^{species}}{1 - \log\left(x_{species|layer}\right)}, \tag{2.22}$$

where T_m^{layer} is the layer melting temperature, $T_m^{species}$ is the melting temperature of some species derived via its EOS, and $x_{species|layer}$ is the molar fraction of that species in the layer.

We do not include partial melting in our model, which could be enhanced by volatiles within the mantle not included in our model (Katz et al.; 2003; Hirschmann et al.; 2009; Unterborn et al.; 2020). As the liquid mantle is generally less dense than the solid mantle, this results in an overestimation of mantle densities. Although simple, Eq. 2.22 reproduces the expected result that mantle melting temperatures containing $MgSiO_3$ mixed with a few weight percent of other substances are lower than mantle melting temperatures containing pure $MgSiO_3$ (Andrault et al.; 2011; Fiquet et al.; 2010; Nomura et al.; 2014; Unterborn et al.; 2020).

2.2.3 H/He Envelope

Chabrier et al. (2019) calculate P-T tables for pure H and He that we combine using Eq. 2.18 with the addition of $V_{mix}(P,T)$ and $S_{mix}(P,T)$ terms derived by Howard and

[6]Eq. 2.22 breaks down for very low $x_{species|layer}$. In this study, the only occurrence of such a breakdown is in the Fe-rich mantle of Europa (see Section 2.3.6). We thus set $x_{\mathrm{MgSiO_3|mantle}}$ to Earth-like in this equation for Europa.

Guillot (2023) using the results of Chabrier and Debras (2021) to account for non-ideal mixing. Our model can account for any H/He ratio, but we assume a solar H/He ratio throughout this publication.

The EOS of Howard and Guillot (2023); Chabrier and Debras (2021); Chabrier et al. (2019) generally agrees with the older widely-used EOS of Saumon et al. (1995) below ∼100 GPa, but above are systematically denser, with densities up to ∼10% greater than formulations not accounting for non-ideal mixing.

These systematically higher densities can have consequences in the interpretation of interior structure models, as is the case for interpretation of Juno data. The core mass of Jupiter estimated from Chabrier et al. (2019) alone is $14.1 M_{\oplus}$ whereas the core mass of Jupiter estimated from Chabrier et al. (2019); Chabrier and Debras (2021); Howard and Guillot (2023) is 20.8 $M_{\oplus}$, closer to the pebble isolation mass (Lambrechts and Johansen; 2014; Bitsch et al.; 2018). However, we note that (1) Jupiter may have accreted significant solids after core formation and thus Jupiter's current metallicity may not reflect its mass before beginning runaway gas accretion and (2) data from the Juno spacecraft point toward a diluted core of Jupiter, so these numbers are not exact and merely indicate that these EOS increase Jupiter's inferred metallicity (Wahl et al.; 2017; Helled et al.; 2022).

2.2.4 Water

We used the AQUA model *P-T* tables of Haldemann et al. (2020) to calculate the EOS of the water layer. These tables combine the previous results of Feistel and Wagner (2006), Journaux et al. (2020), French and Redmer (2015), Wagner and Pruß (2002), Brown (2018), Gordon and McBride (1994); McBride and Gordon (1996), and Mazevet et al. (2019), with the high pressure results of Mazevet et al. (2019) forming the dominant contributor for planets with significant water mass fractions (Haldemann et al.; 2020).

Applying this EOS to isothermal pure water planets produces radii ∼3% smaller than the older EOS used by Zeng et al. (2019, 2016) (Haldemann et al.; 2020); a similar trend is found using a different set of water EOS reported by Grande et al. (2019) Huang et al. (2021). In both cases, the fact that Zeng et al. (2019, 2016)'s model is not isothermal at high pressures makes a direct comparison difficult, although Haldemann et al. (2024) find a similar increased water layer density compared to Zeng et al. (2016, 2019) with a non-isothermal temperature profile.

2.2.5 Mantle

An overview of the species and phases present in our mantle is shown in Figure 2.1.

We calculate the melting temperature of the mantle using the $MgSiO_3$ melting temperature equations of Belonoshko et al. (2005) for low pressures, Stixrude (2014) for intermediate pressures, and Fei et al. (2021) for high pressures, switching at their intersections, as shown in Eq. 2.23. Our reason for this three-piece piecewise curve is that Belonoshko et al. (2005) is required for low pressures to reproduce the melting temperature at 0 pressure but Fei et al. (2021) and Belonoshko et al. (2005) intersect at pressures too low (8.4 GPa) for Fei et al. (2021) to be appropriate. We thus utilize Stixrude (2014) as the intermediate curve between the two extremes. For Earth-like planets, using solely Stixrude (2014) at high pressures leads to an unphysical pattern in which planetary cores at increasing masses first solidify and then re-liquify while using Fei et al. (2021) at Earth's pressures leads to temperatures far too high to explain Earth's solid inner core in our methodology (see Sections 2.2.6, 2.2.7, 2.3.1, and 2.4).

$$T_{Solid/Liquid}^{MgSiO_3} = \begin{cases} 1831\text{K}(1 + \frac{P}{4.6\text{GPa}})^{0.33} & P \leq 199.5\text{GPa} \\ 5400\text{K}(\frac{P}{140\text{GPa}})^{0.48} & 358.7\text{GPa} > P > 199.5\text{GPa} \\ 6295\text{K}(\frac{P}{140\text{GPa}})^{0.317} & P \geq 358.7\text{GPa} \end{cases} \tag{2.23}$$

Dong, Mardaru, Asimow, Stixrude and Fischer (2025); Dong, Fischer, Stixrude, Brennan, Daviau, Suer, Turner, Meng and Prakapenka (2025) used a machine learning technique to determine the slope of the $MgSiO_3$ melting temperature, giving results similar but not identical to this (within 12% from 3,200-10,000 K). We do not use this melting curve because of concerns with extrapolating a constant melting curve slope to high pressures with sparse data. We calculate $x_{\text{MgSiO}_3|\text{mantle}}$ for Eq. 2.22 following the analytical formulae for the lower mantle given in Haldemann et al. (2024).

Above the melting temperature, we use the equations of state listed in Table 2.3. Stewart et al. (2020)'s Mg_2SiO_4 EOS is provided in ρ-T space and we use linear interpolation between adjacent data points in ρ and T to generate a table in P-T space. We use this EOS rather than one for MgO as we are unaware of any liquid MgO EOS covering the desired parameter space (Haldemann et al.; 2024). As there is no EOS for Mg in the mantle not in Mg_2SiO_4, this limits our model to planets with $\frac{\text{Mg}}{\text{Si}} > 0.5$, which is the case for every star in the study of sun-like stars in the solar neighbourhood by Bedell et al. (2018).

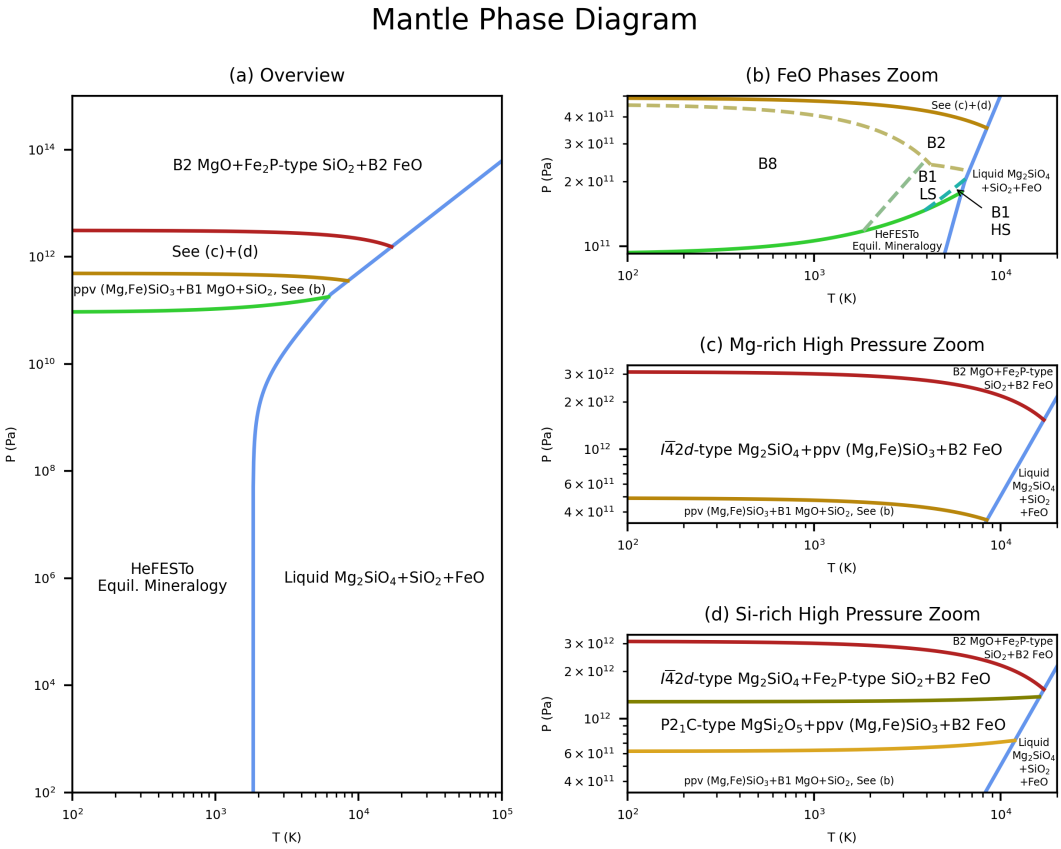

FIGURE 2.1: The species and phases of those species in our mantle. Solid lines represent changes in chemical composition, dashed lines represent solely changes in phase of a species. Colours are arbitrary but are consistent across panels. Equil. is an abbreviation for equilibrium. + indicates the coexistence of multiple species. Note that many phase and chemical transitions take place in the region labeled HeFESTo Equi. Mineralogy. The case shown is for $x_{\mathrm{MgSiO_3}} = 1$ in the region with post-perovskite, the melting curve would move to lower temperatures with the addition of other species. See text for details. (a) The entire parameter space of the mantle. (b) Zoom-in to the region where post-perovskite is present, with FeO phase transitions indicated. (c) Zoom-in to ∼TPa pressures for a mantle with Mg/Si > 1. (d) Zoom-in to ∼TPa pressures for a mantle with Mg/Si ≤ 1.

Stewart et al. (2020) find a melting point different from that obtained using Equations 2.22 and 2.23 and we do not have access to separate solid and liquid EOS, so we allow for solid Mg_2SiO_4 within our liquid state. We avoid this phase transition introducing an artificial jump in the adiabatic gradient by keeping $(\frac{\partial S}{\partial T})_P$ constant for pressures inside or within one datapoint of the solid-liquid transition. This constant value of $(\frac{\partial S}{\partial T})_P$ is that of the highest-pressure liquid for the given temperature.

We use the publicly available FEOS code of Faik et al. (2018) to calculate ρ-T SiO_2 EOS grids and use linear interpolation between adjacent data points in ρ and T to generate a table in P-T space. We use Faik et al. (2018) for all pressures; although there are concerns with Faik et al. (2018)'s EOS' applicability to pressures below the critical point (Haldemann et al.; 2024), we prioritize avoiding an artificial discontinuity in the SiO_2 EOS, especially one in which higher pressure leads to lower densities. Planetary mantle pressures are generally in excess of the critical point (in our model Earth, ∼99% of the mass of the mantle is at pressures greater than the SiO_2 critical point), so the effects of non-applicability are minimal.

Below the melting temperature, we use different sets of EOS depending on the pressure. The Perovskie–Post-Perovskite (pv–ppv)transition is given by Dong, Fischer, Stixrude, Brennan, Daviau, Suer, Turner, Meng and Prakapenka (2025); Dong, Mardaru, Asimow, Stixrude and Fischer (2025) as in Eq. 2.24.

$$P_{\text{ppv/pv}}^{\text{MgSiO}_3} = \left(120 + 0.014(\frac{T}{K} - 2000)\right) \text{GPa} \tag{2.24}$$

Below the Perovskite–Post Perovskite transition, we implement the HeFESTo system of equations of state presented in Stixrude and Lithgow-Bertelloni (2024, 2011, 2005) using Perple_X 7.1.7 (Connolly; 2009). Perple_X is a geochemical software that solves for the equilibrium mineralogy of mantle materials using Gibbs free energy minimization (Connolly; 2009, 2017). The chemical composition of the upper mantle thus varies freely to its equilibrium state while its elemental composition remains uniform.

HeFESTo includes its own EOS for $MgSiO_3$ post-perovskite, but it is in the poorly-extrapolating BM3 form (Stixrude and Lithgow-Bertelloni; 2005, 2011, 2024). We thus stop using HeFESTo above the pv-to-ppv transition, minimizing artificial changes in the density profile by changing at a preexisting density jump.

For pressures above the Perovskite–Post-Perovskite transition we calculate the equations of state for the species $MgSiO_3$, $FeSiO_3$, MgO, SiO_2, and FeO, with each species' relative abundance determined from the input mantle-wide molar fractions of MgO,

SiO_2, and FeO[7] following Haldemann et al. (2024)'s equations that ensure the molar mass fraction of perovskite is as high as possible. The EOS that we use in the solid mantle are shown in Table 2.2.

Sakai et al. (2016) report multiple fits for ppv $MgSiO_3$'s EOS, we use Fit 8–which is derived via simulation–rather than Fit 7–which is derived via experiment–because it satisfies Keane's rule (see section 2.2.2.1) while Fit 7 does not (Keane; 1954; Guignot et al.; 2007). Sakai et al. (2016) do not recommend use of their Fits 1-6. At high ($\sim$300 GPa) pressures, Fit 8 is $\lesssim$1% less dense than Fit 7, indicating good agreement.

Greenberg et al. (2023) report only isothermal parameters for the EOS of B2 FeO, so we use the thermal parameters for B8 FeO from Fischer et al. (2011) for B2 FeO. We select B8 FeO rather than B1 FeO for this purpose because B8 FeO is likely to be the phase present immediately above B2 FeO in super-Earth mantles.

The FeO B8-B1 transition begins at the triple point from Fei and Mao (1994) and follows the slope of Ozawa et al. (2010), resulting in a phase transition given by Eq. 2.25. The FeO B2-B8 transition of Eq. 2.26 is from Zhang et al. (2023). The FeO B1-B8 of Eq. 2.27 transition is from Ozawa et al. (2011), with the slope reported in the text and the intercept extracted from their Figure 1.

$$P^{\mathrm{FeO}}_{\mathrm{B8/B1}} = \left(66.4 + 0.063(\frac{T}{K} - 1020)\right) \text{ GPa} \tag{2.25}$$

$$P^{\mathrm{FeO}}_{\mathrm{B2/B8}} = \left(329 - 0.052(\frac{T}{K} - 2496)\right) \text{ GPa} \tag{2.26}$$

$$P^{\mathrm{FeO}}_{\mathrm{B2/B1}} = \left(242 - 0.0062(\frac{T}{K} - 3842)\right) \text{ GPa} \tag{2.27}$$

FeO can be in a low-spin (LS) or high-spin (HS) state (Greenberg et al.; 2023; Badro; 2014). In the parameter space relevant to planetary interiors, B8 FeO and B2 FeO are always in the LS state (Greenberg et al.; 2023). In contrast, B1 undergoes a transition from HS to LS as pressure increases following Eq. 2.28, which we obtain from Greenberg et al. (2023)'s Figure 1. This transition can cause FeO density jumps nearing 10% (Greenberg et al.; 2023), so studies that assume FeO is in the HS state–as it is in ambient conditions–systematically underestimate FeO's density. Greenberg et al. (2023) provide no thermal EOS and thus we couple their isothermal pressure with the thermal pressure of Fischer et al. (2011), with the caveat that Fischer et al. (2011) assumed HS

[7]Stixrude and Lithgow-Bertelloni (2024)'s model take x_{Fe} and x_O as separate free parameters, we take $x_{\mathrm{O}} = x_{\mathrm{Fe}} = x_{\mathrm{FeO}}/2$

FeO[8] and Ozawa et al. (2011) find that LS B8 FeO has a greater thermal expansivity than HS B8 FeO.

$$P^{\mathrm{FeO}}_{\mathrm{B1(LS)/B1(HS)}} = \left(93 - 0.023(\frac{T}{K} - 1571)\right)\ \mathrm{GPa} \tag{2.28}$$

The MgO B2-B1 transition curve of Eq. 2.29 is identical to the chemical transition curve of Eq. 2.30, we choose this to align our transitions. This is extremely close ($T = 0$ point differs by 9 GPa and slope by 2 MPa) to the findings of Dong, Mardaru, Asimow, Stixrude and Fischer (2025); Dong, Fischer, Stixrude, Brennan, Daviau, Suer, Turner, Meng and Prakapenka (2025).

$$P^{\mathrm{MgO}}_{\mathrm{B2/B1}} = \left(490 - 0.016(\frac{T}{K} - 300)\right)\ \mathrm{GPa} \tag{2.29}$$

Umemoto and Wentzcovitch (2011); Umemoto et al. (2017) report that theoretically ppv $MgSiO_3$ undergoes a high-pressure phase transition into $I\bar{4}2d$ Mg_2SiO_4 and $P2_1/c$-type $MgSi_2O_5$. This transition has never been experimentally confirmed due to its high pressure, however, the $I\bar{4}2d$ or the similar $I\bar{4}3d$ phase have been experimentally observed in Mg_2GeO_4 and Fe_3O_4, analogues for Mg_2SiO_4 that undergo similar phase transitions at lower pressures (Dutta et al.; 2022; Umemoto and Wentzcovitch; 2019; Zurkowski et al.; 2022).

The exact sequence depends on whether there is free MgO or free SiO_2 in the mantle (i.e if Mg/Si is $>$ or $\leq$1). If there is free MgO in the mantle, past the pressure of Eq. 2.30 as much MgO as possible combines with $MgSiO_3$ to form Mg_2SiO_4 (Umemoto et al.; 2017).

$$P^{\mathrm{Mg_2SiO_4+MgSiO_3}}_{\mathrm{MgSiO_3+MgO}} = \left(0.49 * 10^{12} - 16 * 10^6 \frac{T}{K}\right)\ \mathrm{Pa} \tag{2.30}$$

If there is free SiO_2 in the mantle, past the pressure of Eq. 2.31 as much SiO_2 as possible combines with $MgSiO_3$ to form $MgSi_2O_5$ (Umemoto et al.; 2017). At the higher pressures of Eq. 2.32, $MgSi_2O_5$ dissociates into Mg_2SiO_4 (Umemoto et al.; 2017).

$$P^{MgSi_2O_5+MgSiO_3}_{\mathrm{MgSiO_3+SiO_2}} = \left(0.62 * 10^{12} + 9 * 10^6 \frac{T}{K}\right)\ \mathrm{Pa} \tag{2.31}$$

[8]Whenever calculating the thermal pressure using a different EOS from that used for the isothermal pressure, we use the V_0 from the source of the thermal EOS, as is done by Hakim et al. (2018)

$$P^{\mathrm{Mg_2SiO_4+SiO_2}}_{\mathrm{MgSi_2O_5+MgSiO_3}} = \left(1.31 * 10^{12} + 6 * 10^6 (\frac{T}{K} - 5000)\right) \mathrm{Pa} \tag{2.32}$$

Regardless of the value of Mg/Si, above the pressures of Eq. 2.33, the Mg and Si of the mantle are completely dissolved into oxides (Umemoto et al.; 2017).

$$P^{\mathrm{MgO+SiO_2\ or\ MgO}}_{\mathrm{Mg_2SiO_4+SiO_2\ or\ MgO}} = \left(3.1 * 10^{12} - 92 * 10^6 \frac{T}{K}\right) \mathrm{Pa} \tag{2.33}$$

This sequence was specifically reported for molar ratios of MgO or SiO_2 to $MgSiO_3$ of 1:1. We do not include all transitions on the path between MgO or SiO_2 and $MgSiO_3$ to MgO and SiO_2 because to the authors' knowledge there is no publicly available precise curve for these transitions, only approximate curves as in van den Berg et al. (2019). We assign all excess atoms to ppv $MgSiO_3$ because it is the only molecule at these pressures existing in a form that has been directly observed. Thus, for Mg/Si$>$ 1 we have Reactions 2.34-2.35 while for Mg/Si$<$ 1 we have Reactions 2.36-2.38.

$$\mathrm{xMgSiO_3 + yMgO \rightarrow (x-y)MgSiO_3 + yMg_2SiO_4} \tag{2.34}$$

$$\mathrm{(x-y)MgSiO_3 + yMg_2SiO_4 \rightarrow (x+y)MgO + xSiO_2} \tag{2.35}$$

$$\mathrm{xMgSiO_3 + ySiO_2 \rightarrow (x-y)MgSiO_3 + yMgSi_2O_5} \tag{2.36}$$

$$\mathrm{(x-y)MgSiO_3 + yMgSi_2O_5 \rightarrow \frac{x}{2}Mg_2SiO_4 + \frac{x+2y}{2}SiO_2} \tag{2.37}$$

$$\mathrm{\frac{x}{2}Mg_2SiO_4 + \frac{x+2y}{2}SiO_2 \rightarrow xMgO + (x+y)SiO_2} \tag{2.38}$$

Niu et al. (2015) report a different sequence with a temperature dependence, we favor the sequence of Umemoto et al. (2017) due to its relative simplicity.

Tsuchiya and Tsuchiya (2011) and Wu et al. (2011) report EOS for Fe_2P-type SiO_2. Wu et al. (2011) report no thermal parameters while Tsuchiya and Tsuchiya (2011) do not report a K_0'. We thus combine their EOS. We use the values of V_0, K_0, γ, and θ_D (all assumed constant) from Tsuchiya and Tsuchiya (2011) at 0.7 TPa. Our K_0 value is for a T_0 of 300 K, the lowest temperature reported, and our γ value is for a temperature of 4000 K, which is representative both of the temperatures at which this phase exists in planetary interiors and of the typical value of γ across temperatures (as we assume γ is temperature-dependent throughout this work). We take the value of K_0' from Wu et al. (2011) at 0.8 TPa as extrapolated from a BM3 fit. As our reference conditions are at high rather than ambient pressures, we add the constant term $P_0 = 0.7$ TPa to

Eq. 2.5. Even though we apply a Vinet rather than a BM3 fit and use K_0' from a different literature source, we find that our results are within $\lesssim 1\%$ of those shown in Tsuchiya and Tsuchiya (2011)'s Figure 2.

We caution that this approach is not consistent as their parameters were derived assuming different values and the BM3 and Vinet fit values are not the same (e.g. Sakai et al.; 2016), but we needed an EOS that could go above 3.5 TPa. At 100 K, our Vinet fit is less dense than their BM3 fit by 0.3% at 852 GPa, 1.3% at 1.5 TPa, and 4.6% at 2.5 TPa. Our Vinet fit to the Fe_2P-type SiO_2 EOS is always denser than the lower-density SiO_2 EOS of Faik et al. (2018) at the same pressures, indicating that our solution is still sound.

Dutta et al. (2023) find that $I\bar{4}2d$ Mg_2SiO_4 disorders at high temperatures, causing it to have lower densities than predicted by the EOS we use here. We do not include this effect due to the lack of a closed-form EOS for this effect.

We additionally caution that the tabular EOS reported by Umemoto and Wentzcovitch (2011) $P2_1/c$-type $MgSi_2O_5$ and by Umemoto et al. (2017) for $I\bar{4}2d$ Mg_2SiO_4 have poor resolution (200 GPa and 1000 K). Despite these weaknesses in the EOS and the unconfirmed nature of these high-pressure phases in the mantle, we include them to avoid a systematic underprediction of the mantle densities of massive planets. Even if these phase transitions are not accurate, the phase transitions in reality would have the same systematic effect of increasing densities as our treatment here.

Another high-pressure phase of SiO_2, cotunnite, has been reported at high temperatures Oganov (2015); Umemoto et al. (2006); González-Cataldo et al. (2016), we do not include it here as it occurs at temperatures higher than occur in the mantles of the vast majority of planets in our isocomposition curves and it has very similar parameters to Fe_2P-type SiO_2 (Wu et al. (2011) find it has the same K_0' and a K_0 within 0.5% of Fe_2P-type SiO_2).

Further phase transitions such as Fe_2P-type SiO_2 into I4/mmm at 10-14 TPa (encountered in mantles of Earth-like planets $\gtrsim 20 M_\oplus$) have been predicted, but we avoid implementing unobserved phase transitions beyond the dissociation of the mantle into oxides (Lyle et al.; 2015; Wang, Lv, Hu, Wang and Zhao; 2024). Umemoto et al. (2017) found that further changes in chemical composition deeper in the mantle are unlikely, indicating our model is likely largely accurate up to very high pressures.

The net effect of this suite of mantle EOS is denser planets than those assumed by models of pure $MgSiO_3$ due to the inclusion of $FeSiO_3$, the densest silicate stable in the lower mantle of the Earth (Yang et al.; 2024), and denser planets than those derived from extrapolations from Earth's structure due to the inclusion of high-pressure phase transitions not present in Earth's interior. For sufficiently hot planets, allowing the mantle to melt and including thermal pressure terms results in lower densities.

TABLE 2.2: The EOS used within the solid mantle at pressures beyond the perovskite-post-perovskite transition. AE is short for anharmonic & electronic. Vinet is short for Vinet-Rydberg. Ppv is short for post-perovskite. BM3 is short for third-order Birch-Murnaghan. Debye is short for Mie-Grüneisen-Debye.

Compound	Phase	Isothermal EOS	Thermal EOS	AE EOS	γ_{th}	Reference
$MgSiO_3$	ppv	Keane	Debye	None	Al'tshuler	Sakai et al. (2016)
$FeSiO_3$	ppv	BM3	Debye	None	$\gamma_\infty = 0$	Stixrude and Lithgow-Bertelloni (2024)
FeO	B1 (HS)	BM3	Debye	None	$\gamma_\infty = 0$	Morard et al. (2022); Fischer et al. (2011)
FeO	B1 (LS)	BM3	Debye	None	$\gamma_\infty = 0$	Greenberg et al. (2023); Fischer et al. (2011)
FeO	B8	BM3	Debye	None	$\gamma_\infty = 0$	Greenberg et al. (2023); Fischer et al. (2011)
FeO	B2	BM3	Debye	None	$\gamma_\infty = 0$	Greenberg et al. (2023); Fischer et al. (2011)
MgO	B1	Vinet	Debye	Quadratic	β varied	Ye et al. (2017); Dorogokupets and Dewaele (2007)
MgO	B2	Holzapfel	Einstein	Quadratic	β varied	Musella et al. (2019)[a]
SiO_2	Fe_2P-type	Vinet	Debye	None	Fixed	Tsuchiya and Tsuchiya (2011); This work
SiO_2	Various		Tabular			Faik et al. (2018)
Mg_2SiO_4	$I\bar{4}2d$		Tabular			Umemoto et al. (2017)
$MgSi_2O_5$	$P2_1/c - type$		Tabular			Umemoto and Wentzcovitch (2011)

[a] β is incorrectly listed as negative in Musella et al. (2019)'s original publication. Using the same value of β reported with a positive sign replicates their Figure 1. The given Holzapfel equation formulation is also incorrect, it should follow Eq. 2.6.

TABLE 2.3: The EOS used within the liquid mantle. AE is short for anharmonic & electronic. Vinet is short for Vinet-Rydberg.

Compound	Phase	Isothermal EOS	Thermal EOS	AE EOS	γ_{th}	Reference
FeO	Liquid	Vinet	Einstein	Quadratic	$\gamma_\infty = 0$	Morard et al. (2022)
Mg_2SiO_4	Liquid		Tabular			Stewart et al. (2020)
SiO_2	Liquid		Tabular			Faik et al. (2018)

2.2.6 Core

The phase diagram we employ for Iron is shown in Figure 2.2.

Seismology indicates that Earth's core density is lower than that of pure iron and thus the inclusion of lower-density core materials is essential to recreate the radii of Earth-like planets (Birch; 1952, 1964; McQueen and Marsh; 1966; Ahrens; 1979; Jeanloz; 1979; Unterborn et al.; 2020). The main low-density elements within the Earth's core are Si, O, and S (McDonough; 2014). Si and/or O likely form the majority by weight of the lower-density element in Earth's core, however the partitioning of Si and O into the core rather than the mantle is uncertain at higher pressures: Fischer et al. (2015) find that Si

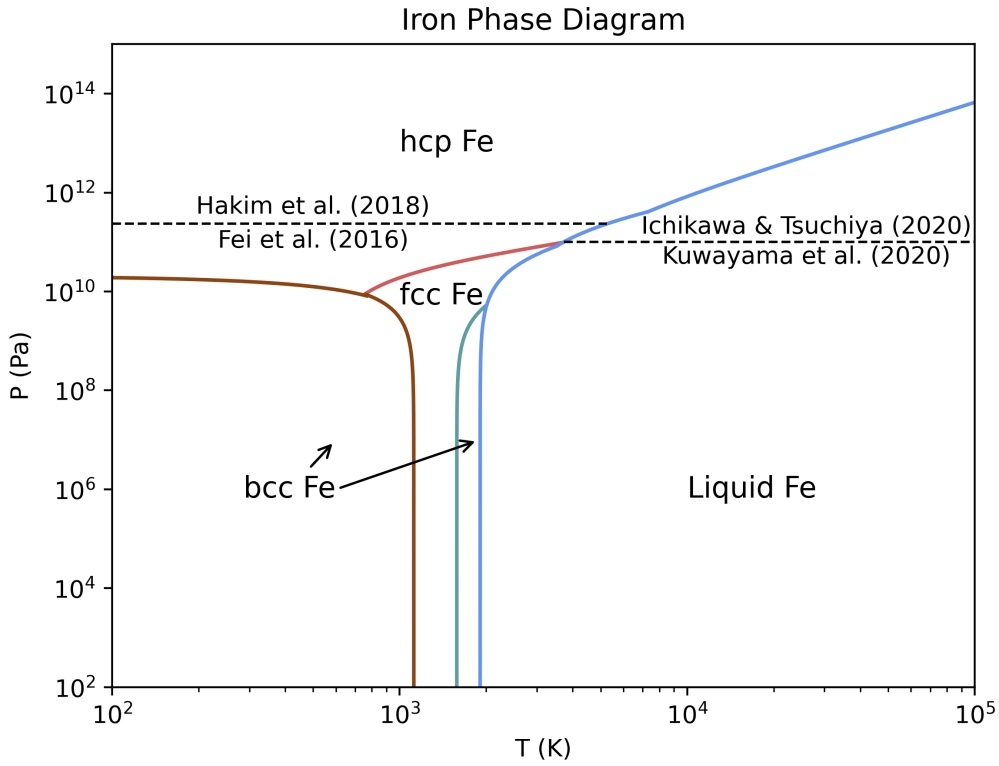

FIGURE 2.2: The phase diagram of iron employed in our model. Solid lines indicate phase transitions while dashed lines represent transitions between using different EOS for the same phase. EOS labels indicate the isothermal portion only, see text and Table 2.5 for details. Colours are arbitrary. Note that solid Fe of all phases coexists with solid FeS VI/VII and liquid Fe coexists with liquid FeS and liquid FeO. The case shown is for $x_S^s = 0$, the blue melting curve would move to lower temperatures with greater x_S^s. See text for details.

and O continue to partition into planetary cores up to $\sim$ 800 GPa while Schaefer et al. (2017) find that Si and O stop partitioning into planetary cores at $\sim$100 GPa.

The light element composition of planetary cores thus depends on the pressures at which the metals and silicates of planets equilibrated (Wade and Wood; 2005), which requires an understanding of the microphysics of metals in planetary primordial magma oceans and the history of giant melting impacts still in development for Earth (Schaefer et al.; 2017; Lichtenberg et al.; 2023), making an exact determination of the light elements within the cores of super-Earths beyond the scope of this work. We thus use reasonable parameters for the light elements in the core, approximating all light elements as FeO– for which we already have EOS for the mantle–and FeS, which is uncontroversially in Earth's core (albeit at a lower concentration than in our model).

We include liquid FeO but not solid FeO in the core because our liquid FeO EOS is of the better-extrapolating Vinet form while our solid FeO EOS are all BM3. We note that Earth's core, which we use to constrain core element fractions, is mostly liquid (McDonough; 2014; Moulik and Ekström; 2025b).

A key constraint on the composition of the core comes from the observed density jump between Earth's liquid and solid cores of $4.5 \pm 0.5\%$ (Dziewonski and Anderson; 1981; Alfè et al.; 2002; Ichikawa and Tsuchiya; 2020). This jump is larger than expected solely from the transition between liquid and solid (1.5% in our model for Earth core with 0.15 molar mass fraction S), implying that lighter elements preferentially partition into the liquid core, as also found via experiment and simulation (Alfè et al.; 2002; Zhang et al.; 2020; Sakai et al.; 2023).

In support of this effect, Alfè et al. (2002) find that a molar mass fraction of $8 \pm 2.5\%$ of O in the liquid core, negligible O in the solid core, $10 \pm 2.5\%$ S in the liquid core, and $8.5 \pm 2.5\%$ S in the solid core reproduces Earth's density jump well[9]. Hirose et al. (2013) conducted a literature review of proposed light core elements, combining density constraints and geochemical constraints, and preferred weight fractions of Si of $\sim 6\%$, of O of $\sim 3\%$, and of S of $1 - 2\%$. This corresponds to a molar fraction of O of $\sim 9\%$ and a non-Fe-non-O mass fraction of $\sim 8\%$, corresponding to a S molar fraction of $\sim 13\%$ assuming that all non-Fe-non-O mass fraction in the core is S (i.e we approximate Si and all other less abundant elements as S, justified by S's close molar mass to Si).

[9]Alfè et al. (2007) revise their estimates for a density jump of 6.5% rather than 4.5% following the revised Earth interior density jump of Masters and Gubbins (2003), we refer to their results derived from a comparison with PREM here as the upwards-revised density jump is not universally agreed, see Koper and Dombrovskaya (2005).

Umemoto and Hirose (2020) give best fits to PREM for a Fe-Ni-H-Si-O-S-C system for various assumed solid-inner core boundary temperatures, with the most likely T_{ICB} of 5400 K giving $x_{\mathrm{O}} = 0.08$ and $x_{\mathrm{S}} = 0.01$ and the somewhat higher T_{ICB} of 6000 K giving $x_{\mathrm{O}} = 0.22$ and $x_{\mathrm{S}} = 0.005$. Hirose et al. (2021) combine density, geochemical, and cosmochemical constraints to get $x^l_{\mathrm{O}} = 0.03 - 0.17$ and $x^l_{\mathrm{S}} = 0.03$ with up to $x^l_{\mathrm{Si}} = 0.07$, $x^l_{\mathrm{H}} = 0.13$, and $x^l_{\mathrm{C}} = 0.01$ for the outer core and $x^s_{\mathrm{O}} < 0.01$ $x^s_{\mathrm{S}} = 0 - 0.02$ with up to $x^s_{\mathrm{Si}} = 0.04$, $x^s_{\mathrm{H}} = 0.12$, and $x^s_{\mathrm{C}} = 0.06$ for the inner core.

We find that $x^l_{\mathrm{O}} = 0.08$ and $x^l_{\mathrm{S}} = 0.09$ in the liquid core and $x^s_{\mathrm{S}} = 0.115$ in the solid core best matches our model and Earth's interior (see section 2.3.1) and thus select these values as fiducial. These values are within the uncertainties of those reported by Alfè et al. (2002) and Hirose et al. (2013) (note that the liquid core is much larger than the solid core and thus the bulk core composition is near to the liquid core composition) but lower than those reported by Umemoto and Hirose (2020); Hirose et al. (2021). These discrepancies are to be expected because (1) we use a different set of EOS from previous attempts to identify the light element in Earth's core and thus have no reason to replicate their results and (2) we neglect several elements included in their calculations and thus our values represent effective values resulting from fitting a simplified mineralogy to Earth's core. Additionally, planetary cores are volumetrically small and thus have relatively little impact on planetary radii (see Figure 2.4), minimizing the impact of the assumption of the light element in the core. We emphasize that these values represent effective values for the limited chemical inventory of our cores.

We also emphasize that these values are selected to fit the density structure within Earth's mantle and not to reproduce Earth's radius, so our replication of Earth's radius shown in section 2.3.1 is not a product of actively selecting core parameters to replicate Earth's radius. Due to our close replication of Earth in the rest of our model, alterations to x^l_S, x^l_O, and x^s_S could be employed to replicate Earth's radius to arbitrary precision. This high precision would merely be the product of canceling out any errors in the mantle with an arbitrary core structure and thus would have no reason to extrapolate to other bodies. We note that S in Earth's core is stratified and not uniformly mixed in each layer as assumed here (Ganguly; 2025; Alfè et al.; 2002).

We determine the melting temperature using Eq. 2.39 combined with Eq. 2.22, with x^s_{Fe} being the species of interest. The lowest-pressure piece corresponds to the melting temperature of fcc Fe (see below for solid phases) while the higher two pressure pieces correspond to the melting temperature of hcp Fe. Note that as our phase changes and melting temperatures come from different sources, there is no fcc-hcp-liquid triple point

(see Figure 2.2). We thus allow some hcp Fe to melt following the fcc hcp phase curve to ensure continuity in the melting Temperature.

The first two pieces of Eq. 2.39 come from Dong, Fischer, Stixrude, Brennan, Daviau, Suer, Turner, Meng and Prakapenka (2025); Dong, Mardaru, Asimow, Stixrude and Fischer (2025)'s machine learning classification of literature phase experimental or computational observations, constraining the slope of $T^{\text{Fe}}_{\text{hcp/Liquid}}$ to 5-12$\frac{\text{K}}{\text{GPa}}$ and the slope of $T^{\text{Fe}}_{\text{fcc/Liquid}}$ to 16-23$\frac{\text{K}}{\text{GPa}}$. Dong, Fischer, Stixrude, Brennan, Daviau, Suer, Turner, Meng and Prakapenka (2025); Dong, Mardaru, Asimow, Stixrude and Fischer (2025) do not report separate melting slopes for bcc Fe and thus we assume that bcc Fe has the same melting curve as fcc Fe (the lowest-pressure pirce of 2.39). We choose our slope in the middle piece of 2.39 to reproduce the radius of Earth's liquid-solid core boundary (see Section 2.3.1), which we caution may not accurately reflect reality as the crystallization of the Earth's core is a temporal process not captured by the static model presented here; our slope in the low-pressure piece of Eq. 2.39 is chosen to be the middle of the provided distribution of plausible values. We caution that values of the slope of Eq. 2.39 consistent with Dong, Fischer, Stixrude, Brennan, Daviau, Suer, Turner, Meng and Prakapenka (2025); Dong, Mardaru, Asimow, Stixrude and Fischer (2025) both allow for a completely liquid and completely solid Earth core (changing a model Earth's radius by $\sim$0.5%) and thus our slope is strongly dependent on geological constraints that might not be universally applicable outside of Earth. The highest-pressure piece of Eq. 2.39 comes from González-Cataldo and Militzer (2023), who perform simulations at high pressures. The results of González-Cataldo and Militzer (2023) and Dong, Fischer, Stixrude, Brennan, Daviau, Suer, Turner, Meng and Prakapenka (2025); Dong, Mardaru, Asimow, Stixrude and Fischer (2025) do not cleanly intersect, we swap the equation in use at the pressure where they intersect.

$$T^{Fe}_{Solid/Liquid} = \begin{cases} \left(2100 + 19.5(\frac{P}{\text{Pa}} - 10 * 10^9)\right) \text{K} & P < 82.8\text{GPa} \\ \left(3950 + 11.6(\frac{P}{\text{Pa}} - 120 * 10^9)\right) \text{K} & 82.8\text{GPa} < P < 409.8\text{GPa} \\ \left(6469(1 + (\frac{P - 300 * 19^9\text{Pa}}{434.82 * 10^9\text{Pa}}\right)^{\frac{1}{1.839}} \text{K} & P \geq 409.8\text{GPa} \end{cases} \quad (2.39)$$

We calculate the phase of solid Fe using Equations 2.40-2.43 from Dorogokupets et al. (2017), as extracted by Haldemann et al. (2024). There are two fcc/bcc transitions in Equations 2.41 and 2.42 because bcc is the most stable phase of Fe in two non-contiguous

regions of P-T parameter space (see Figure 2.2).

$$T^{Fe}_{hcp/fcc} = 575 + 18.7\left(\frac{P}{\text{GPa}}\right) + 0.213\left(\frac{P}{\text{GPa}}\right)^2 - 0.000817\left(\frac{P}{\text{GPa}}\right)^3 \text{ K} \tag{2.40}$$

$$T^{Fe}_{fcc/bcc1} = 1120 - 300\left(\frac{P}{\text{GPa}}\right) \text{ K} \tag{2.41}$$

$$T^{Fe}_{fcc/bcc2} = 1580 + 418\left(\frac{P}{\text{GPa}}\right) \text{ K} \tag{2.42}$$

$$T^{Fe}_{hcp/bcc} = 820 - 520\left(\frac{P - 7.3 \text{ GPa}}{8.5 \text{ GPa}}\right) \text{ K} \tag{2.43}$$

The EOS for the liquid core are shown in Table 2.4. We use two separate EOS for liquid Fe as Ichikawa and Tsuchiya (2020) and Kuwayama et al. (2020) reported EOS fits over different pressure regimes. We caution that these two EOS do not meet cleanly, with Ichikawa et al. (2014)'s result ∼4% denser at 5000 K and 100 GPa than Kuwayama et al. (2020). However, as the higher-density EOS is found at greater pressures, this does not result in an unphysical density decrease and thus we find it acceptable. We do not use the more recent isothermal Fe EOS from Luo et al. (2024) or Xie et al. (2025) because they are fit with BM3 and thus extrapolate poorly to high pressures, however we do augment Ichikawa and Tsuchiya (2020)'s isothermal pressure with Xie et al. (2025)'s thermal pressure.

The liquid FeS EOS from Ichikawa and Tsuchiya (2020) is for $Fe_{0.81}S_{0.19}$, placing an upper bound on x^l_S of 0.19, as above this value there is not sufficient Fe to form the alloy whose EOS we use. Similarly, we cannot have $x^l_O > 0.5$ as it would require an EOS for free Fe in the liquid core that we do not have. As the latter would likely correspond to a denser mantle than core, it is unphysical. In contrast, the restriction on x^l_S rules out plausible values (see the required low values to accomodate a greater x^l_O in Section 2.3.2).

We do not use the same liquid FeO EOS for the mantle and core because the low-pressure EOS of Morard et al. (2022) was derived for $P \lesssim 120$ GPa and does not meet cleanly with the EOS of Ichikawa and Tsuchiya (2020) derived for higher pressures. The structure of Earth's liquid core cannot be recovered by extrapolating Morard et al. (2022)'s low-P FeO EOS to high pressures (its $\frac{\partial r}{\partial \rho}$ is too large), motivating our switch between the EOS at the mantle-core boundary. As is the case for liquid Fe, the two EOS do not meet cleanly, causing a density jump of $\sim 7\%$ at 100 GPa and 5000 K.

TABLE 2.4: The EOS used within the liquid core. AE is short for anharmonic & electronic. Vinet is short for Vinet-Rydberg..

Compound	Phase	Isothermal EOS	Thermal EOS	AE EOS	γ_{th}	Reference
Fe	Liquid (P > 100 GPa)	Vinet	Linear	Quadratic	Constant	Ichikawa and Tsuchiya (2020); Xie et al. (2025)
Fe	Liquid (P < 100 GPa)	Vinet	Linear	Quadratic	$\gamma_\infty = 0$	Kuwayama et al. (2020)
FeO	Liquid	Vinet	Einstein	Quadratic	$\gamma_\infty = 0$	Ichikawa and Tsuchiya (2020); Haldemann et al. (2024)
FeS	Liquid	Vinet	Linear	Quadratic	Constant	Ichikawa and Tsuchiya (2020)

The EOS used for the solid core are shown in Table 2.5. At high pressures within Earth and the cores of more massive planets, the density difference between Fe phases is $\lesssim$1% and decreases with pressure, so our results are insensitive to the exact phase transitions assumed (Hakim et al.; 2018; Cottenier et al.; 2011). This justifies our non-inclusion of the reported phase transition of hcp Fe back into fcc and bcc Fe at $P \gtrsim 8$ TPa (Pickard and Needs; 2009; Cottenier et al.; 2011; Stixrude; 2012). Hakim et al. (2018) calculate their Fe EOS without thermal effects and thus use the results of Bouchet et al. (2013) to calculate thermal pressures; we use the more recent results of Zhang et al. (2025) to calculate the thermal pressure of Fe, which has θ_0 $\gtrsim$20 times larger than Bouchet et al. (2013) due to the inclusion of experimental data in Zhang et al. (2025) and approximations in the theory of Bouchet et al. (2013). We use Fit #5 of Zhang et al. (2025) because it is the lowest-residual fit using an isothermal Vinet formulation, more closely matching the isothermal formulation used in our model than the BM3 Fit #1 with a slightly lower residual.

Zhang et al. (2025) do not include an anharmonic/electronic term. We have found that including the anharmonic/electronic term of Bouchet et al. (2013) with the thermal term of Zhang et al. (2025) leads to $\nabla_{\rm ad}$ values near the pressure-temperature regime of Earth's core that are higher than the $\nabla_{\rm ad}$ values for liquid Fe at those same pressures and temperatures, leading to our solutions being unable to enter the solid phase. This is because as our solutions move toward the planetary center, the crossing of the liquid-solid transition increases the temperature gradient, causing higher temperatures that return the solution to the liquid state. We thus do not use the anharmonic/electronic term of Bouchet et al. (2013). We found that combining the anharmonic/electronic term of Dorogokupets et al. (2017) with the thermal term of Zhang et al. (2025) causes densities to increase with temperature at $P \gtrsim 2$ TPa because Dorogokupets et al. (2017)'s g is negative. As neither of these anharmonic/electronic terms are compatible with our formalism and to our knowledge no EOS with anharmonic/electronic terms derived using data up to a TPa exists besides that of Bouchet et al. (2013), we include no anharmonic/electronic term for Fe hcp.

The closed-form EOS provided by Hakim et al. (2018) is only valid above 234.4 GPa, necessitating that the EOS of Fei et al. (2016) be used below that pressure. We use the thermal expression from Zhang et al. (2025) and no anharmonic/electronic expression for Fei et al. (2016)'s data for consistency with our update to Hakim et al. (2018)'s data. Hakim et al. (2018)'s EOS was designed to cleanly match Fei et al. (2016)'s EOS, but our update to the thermal terms slightly breaks this clean meeting, introducing an artificial density jump (∼0.5% at 5500 K). As the artificial density jump is positive, our model still produces a gravitationally stable interior structure.

We use a single EOS for FeS as we prioritize the superior high-pressure extrapolation of the Holzapfel form over the accuracy of including a phase transition that occurs at ∼180 GPa, a lower pressure than the ∼330 GPa at which Earth's core becomes solid and thus a pressure unlikely to be encountered in the solid cores of super-Earths or sub-Neptunes (Ohfuji et al.; 2007; Sata et al.; 2008). Only six data points in the FeS fit are for the higher pressure Fe VII, so our fit is dominated by the lower pressure Fe VI even though the core will be composed mostly of Fe VII, however, the authors are unaware of a study with sufficient measurements of Fe VII to remedy this issue (Sata et al.; 2010). The FeS VI/VII data were only collected at one temperature and thus have no thermal fit (Sata et al.; 2010; Ohfuji et al.; 2007; Sata et al.; 2008), so we calculate $\nabla_{\rm ad}$ for the solid core as if it is pure Fe. This is motivated by the fact that although the density of Earth's solid core is highly discrepant with that expected for pure hcp Fe, its K_S is in line with that of a pure hcp core (Dorogokupets et al.; 2017).

TABLE 2.5: The EOS used within the solid core. AE is short for anharmonic & electronic. Vinet is short for Vinet-Rydberg. BM3 is short for third-order Birch-Murnaghan. Debye is short for Mie-Grüneisen-Debye. hcp is short for hexagonal close-packed. bcc is short for body-centered cubic. fcc is short for face-centered cubic. FeS undergoes a phase transition from VI to VII at ∼180 GPa (Ohfuji et al.; 2007; Sata et al.; 2008, 2010), but the EOS used fits all FeS data with one form.

Compound	Phase	Isothermal EOS	Thermal EOS	AE EOS	γ_{th}	Reference
Fe	hcp (P > 234.4 GPa)	Holzapfel	Debye	None	$\gamma_\infty = 0$	Hakim et al. (2018); Zhang et al. (2025)
Fe	hcp (P < 234.4 GPa)	BM3	Debye	None	$\gamma_\infty = 0$	Fei et al. (2016); Zhang et al. (2025)
Fe	bcc	Vinet	Einstein	Quadratic	$\gamma_\infty = 0$	Dorogokupets et al. (2017)
Fe	fcc	Vinet	Debye	Quadratic	$\gamma_\infty = 0$	Dorogokupets et al. (2017)
FeS	VI/VII	Holzapfel	Einstein	None	$\gamma_\infty = 0$	See a

[a] Hakim et al. (2018) refit of data reported in Sata et al. (2010) from experiments conducted in Sata et al. (2008); Ohfuji et al. (2007) with thermal term from Zhang et al. (2025)

In the high core pressure regimes of planets with masses greater than Earth, the EOS of Hakim et al. (2018) dominates. Hakim et al. (2018) finds high-pressure densities

using density functional theory that are higher than predicted from extrapolations from low-pressure experimental results and uses the EOS formulation of Holzapfel (1996) that is more suited to high pressures. These effects combine to generate radii $\sim 6\%$ smaller than Zeng et al. (2019) for pure Fe bodies. However, the introduction of light elements into the core counteracts this effect, increasing planetary radii. Allowing the core to melt also increases planetary radii compared to the assumption of a solid interior. Our inclusion of low-pressure Fe phases increases the radii of small planets with large cores but has no effect on larger planets ($\gtrsim 1 M_{\oplus}$) whose entire solid cores' iron are in the hcp state.

2.2.7 Thermal Structure

The irradiated atmospheric layer extends from the outer boundary of the planet to the high optical depth ($\tau \gg 1$) region where no more solar flux is absorbed, which we approximate as an optical depth of $\tau = 1000$. We calculate τ using Eq. 2.44.

$$\frac{\partial \tau}{\partial m} = -\frac{\kappa}{4\pi r^2} \tag{2.44}$$

Eq. 2.44 comes from integrating the definition of τ, $d\tau \equiv -\rho \kappa dz$, in a plane-parallel hydrostatic atmosphere (Guillot; 2010). The plane-parallel assumption is justified by the irradiated atmosphere composing a relatively small fraction of the total planetary radii, for example, the irradiated atmosphere only comprises 0.005% of the radius of an Earth-mass planet comprised of half water and half Earth-like composition with an equilibrium temperature of 1000 K.

Within the irradiated atmospheric layer, we calculate the temperature profile using the fits provided by Parmentier and Guillot (2014); Parmentier et al. (2015) to radiative transfer models, which rely on values for κ, $T_{\rm eq}$, $L_{\rm int}$, and A_B.

We assume that Within the irradiated atmospheric layer, we calculate the temperature profile using the fits provided by Parmentier and Guillot (2014); Parmentier et al. (2015)'s model D fit to radiative transfer models, which rely on values for κ, $T_{\rm eq}$, $L_{\rm int}$, and A_B. We caution that these analytical solutions were derived around a sun-like star and thus are not strictly valid for stars with significantly different radiation profiles (Parmentier and Guillot; 2014; Parmentier et al.; 2015).

We assume that κ arises from an equilibrium composition of metals arising from the stellar temperature $T_{\rm eff}$ and calculate κ using the Rosseland mean opacities provided by

Freedman et al. (2014). We set $T_{\rm eff} = 6000$ K throughout this work as it is the closest value to the sun among those offered (opacities are only provided in 1000 K intervals for stellar temperature).

Observations of exoplanetary upper atmospheric metallicity as probed by H_2O have revealed substantial scatter from $\sim$0.3 to $\sim$100 times solar while solar system C/H spectroscopy and extrasolar interior structure models have given mass-metallicity relations implying $Z \gtrsim 50$ for the $M < 25M_\oplus$ planets of our sample (Edwards et al.; 2023; Thorngren et al.; 2016; Guillot et al.; 2023; Kreidberg et al.; 2014; Swain et al.; 2024). Keeping in mind the large uncertainties in observed and theoretical planetary atmospheric metallicities, we assume $Z = 50Z_\odot$ ($[M/H] = 1.7$), the highest metallicity provided by the Freedman et al. (2014) tables and roughly in line with Uranus and Neptune's atmospheres.

We calculate $T_{\rm eq}$ by assuming that a planet is in thermal equilibrium and we calculate $L_{\rm int}$ following the analytical fits provided by Mordasini (2020)[10]. These analytical fits account for internal heating generated by radiogenic luminosity as well as the cooling and contraction of the core and envelope (Mordasini; 2020; Mordasini et al.; 2012; Linder et al.; 2019).

We note that these fits are derived for a smaller parameter space than explored in this study ($1 < \frac{M}{M_\oplus} < 40$,$w_{H_2O} < 0.1$) so innacuracies due to extrapolation may occur at high masses or water mass fractions. Mordasini (2020)'s fits underestimate Jupiter's modern luminosity by a factor of 2.78, indicating that even far outside the fitted parameter space the estimates are the correct order of magnitude. Haldemann et al. (2024) find that variations in the parameters reported by Mordasini (2020) tend to result in $\lesssim 1\%$ changes in exoplanetary radii. We also note that Mordasini (2020)'s estimate for modern Earth's luminosity is 0.6 times the actual value (Kamland Collaboration et al.; 2011), indicating that these fits may not be accurate for old planets with low envelope masses. These planets have low internal luminosities, making the impact of this effect minor.

Additionally, our prescription for temperature jumps (see below) means that the thermal structures of rocky planet interiors are dominated by the melting temperatures of their outermost mantle rather than their equilibrium temperatures. For modern Earth, the inclusion of internal luminosity causes a change in radius ($\sim 10^{-9} R_\oplus$) indistinguishable from numerical inaccuracies.

[10]By incorporating the internal energy source into our outer temperature boundary condition, we forego the need to explicitly include the energy conservation equation in our solution, i.e we can set $\epsilon = 0$ in $\frac{\partial L}{\partial m} = \epsilon$.

We do not use the albedos calculated by the radiative structure model of Parmentier et al. (2015); Parmentier and Guillot (2014) as they do not incorporate clouds, instead we assume an Earth-like A_B of 0.3 (Stephens et al.; 2015), which is also within 0.05 of the A_B of Mars (Statella et al.; 2015), Titan (Li et al.; 2011), Uranus (Irwin et al.; 2025), and Neptune (Pearl and Conrath; 1991), while being consistent with ∼half of hot Jupiters for which measurements exist (Fortney et al.; 2021)[11].

Usage of this internal luminosity prescription relies on the assumption that planets have mantle abundances of the key long-lived radiogenic isotopes ^{40}K, ^{238}U, and ^{232}Th matching Earth's. Stellar abundances of ^{232}Th vary by a factor of two in solar twins while the abundances of the other isotopes have yet to be directly measured, implying that radiogenic heating could differ by a factor of a few from this estimate, especially considering that K on Earth is depleted by a factor of five relative to solar abundances for unknown reasons (Unterborn et al.; 2015; Botelho et al.; 2019; Unterborn et al.; 2020). We emphasize that our results are relatively insensitive to a factor of a few difference in radiogenic heating.

Within the interior layer of $\tau > 1000$, the temperature gradient ∇ is calculated as

$$\nabla = \max\left(\frac{3}{16\pi acG}\frac{\kappa L_{\rm int} P}{mT^4}, \nabla_{\rm ad}\right), \tag{2.45}$$

where a is the radiation constant, c is the speed of light, κ is opacity, $L_{\rm int}$ is the internal luminosity of the planet, and $\nabla_{\rm ad}$ is the adiabatic temperature gradient (see 2.2.2.2). The first term represents the radiative temperature gradient and the second term represents the adiabatic temperature gradient.

In the solid and liquid portion of the planet below these layers, we set a universal adiabatic temperature gradient. We impose a temperature jump to the mantle melting temperature at the top and bottom of the mantle. This is because planetary interiors form molten and rapidly cool until the temperature of the outermost regions of a layer reach the melting temperature and solidify, making further cooling much more inefficient and thus leaving the temperature immediately below the boundary relatively constant at the melting temperature throughout time (Stixrude; 2014; Gaidos et al.; 2010). We note that this justification is only valid if the interior was above the melting temperature

[11] As well as the out-of-date values for Jupiter by Hanel et al. (1981) and Saturn by Hanel et al. (1983) that have recently been revised upward by Li et al. (2018) and Wang, Li, Jiang, Fry, West, Nixon, Guan, Karandana G, Albright, Colwell, Guillot, Hofstadter, Kenyon, Mallama, Perez-Hoyos, Sanchez-Lavega, Simon, Wenkert and Zhang (2024), respectively.

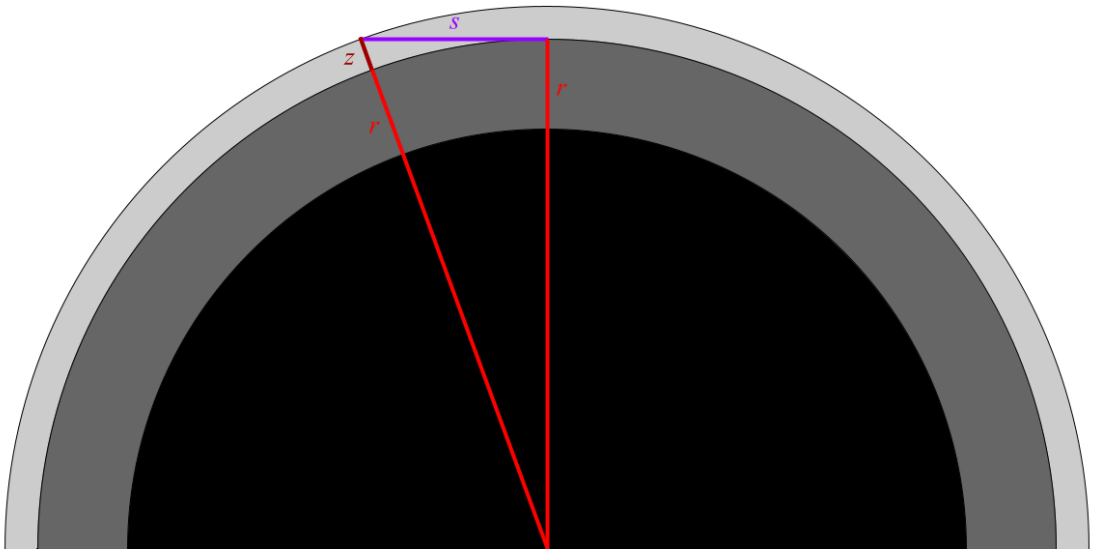

FIGURE 2.3: A diagram showing the variables r (light red lines) and z (dark red line) in relation to s (purple line), the length along which $\tau = \frac{2}{3}$. The darkest circle represents the solid surface of the planet, the lighter circle the transit radius of the planet, and the lightest circle the outermost layer of the atmosphere, defined here to be where $P = 100$ Pa.

when it formed and that interiors do cool with time, making this prescription an upper limit.

2.2.8 Transit Radii

We report our final planetary radii not as $r_{\rm out}$, corresponding to the outermost radial layer of a planet in our model, but rather as the radius at which a light ray traveling along a grazing chord would reach an optical depth of $\tau_{chord} = \frac{2}{3}$. This approximates the radius actually obtained via transit exoplanet detections (Guillot; 2010). To do so, we follow Guillot (2010) and use Eq. 2.46:

$$\tau_{chord}(r) = 2\int_0^\infty \rho\kappa \frac{z+r}{\sqrt{z^2+2rz}} dz, \tag{2.46}$$

where r is the distance from the center of the planet at which $\tau_{\rm chord}$ is measured and z is a distance above r with $r \parallel z$ (add Guillot 2010 Fig. 8). For $r = r_{\rm trans}$, the transit radius of the planet, Eq. 2.46 evaluates to $\frac{2}{3}$.

We get $\rho(z)$[12] and $\kappa(z)$ from a valid solution to the interior structure equations 2.1-2.3. The chord over which the optical depth is measured, s, froms a right triangle with the radius of the planet at which the optical depth is measured, r, and $r + z$ is the hypotenuse of that triangle (see Figure 2.3).

The iteration proceeds as follows: first guess a value $r_{\text{guess}} = r$, then integrate Eq. 2.46 from the outer pressure boundary, where z is some high number approximating ∞, to the radius at which the total optical depth is $\frac{2}{3}$. When the total optical depth is $\frac{2}{3}$, z should be 0 and thus r should be r_{trans}. We thus minimize the z for which $\tau_{\text{chord}} = \frac{2}{3}$ via the Newton-Raphson method. We iterate guesses until r_{guess} and $r(\tau_{\text{chord}} = \frac{2}{3})$ agree within a factor of 10^{-4}.

2.2.9 Rotational Effects

We do not assume that planets are perfectly spherical and employ an analytical approximation for the effects of planetary rotation by multiplying Eq. 2.2 by f_P and Eq. 2.3 by $\frac{f_T}{f_P}$, where f_P and f_T are derived by Paxton et al. (2013, 2019) for rigidly rotating bodies in hydrostatic equilibrium. In this formalism, r does not represent a physical radius and instead represents the radius of a sphere enclosing an equivalent volume to the volume within the physical mass enclosed m. f_P and f_T are functions solely of $\omega \equiv \Omega/\Omega_{crit}$, where Ω is the rotation rate and Ω_{crit} is the critical rotation rate. The critical rotation rate depends on the equatorial rather than the equivalent volume radius and thus depends itself on ω via Eq. 2.47 (Paxton et al.; 2013, 2019). We solve Eq. 2.47 via rootfinding with the Newton-Raphson method. For a planetary rotation period of ∞, $f_P = f_T = 1$.

$$\omega = \frac{\Omega(r(1 - \frac{\omega^2}{6} + 0.01726\omega^4 - 0.03569\omega^6))^{\frac{3}{2}}}{\sqrt{Gm}} \tag{2.47}$$

The effects of rotation are small but noticable, varying a model Earth's radii by $\sim 0.02\%$ compared to a case where rotation is not taken into account.

2.2.10 Brief Summary

We include much more physics than the basic model of a H/He envelope, a water layer, a $MgSiO_3$ mantle, and a Fe core. We briefly point out the improvements that cause systematic differences.

[12] We use ρ from Freedman et al. (2014) for this purpose rather than ρ from Howard and Guillot (2023); Chabrier and Debras (2021); Chabrier et al. (2019) or Haldemann et al. (2020) so that our optical depth calculations rely on EOS from the same source.

The inclusion of Fe in the planetary mantle systematically increases planetary densities, while the inclusion of S and O in the planetary core systematically decreases planetary densities. The inclusion of high pressure phases in the mantle systematically increases densities for high mass planets. The inclusion of temperature jumps at the core/mantle and mantle/core barriers, inclusion of melting in the mantle and core, and inclusion of thermal terms in our solid EOS all systematically increase planetary densities. The new EOS we use for H/He and Fe are systematically denser than the majority of the literature. The calculation of transit radii rather than 100 Pa surface radii results in systematically lower planetary radii (of order %).

2.3 Model Validation

The internal composition of a body can be obtained via seismology, measuring the time that mechanical waves such as those generated by quakes take to move through interior structures (Moulik and Ekström; 2025a). Seismology can also measure the eigenfrequencies of a planet (c.f spherical harmonics) (Montagner and Roult; 2008). These seismographic constraints as well as bulk properties such as masses, radii, moments of intertia, and love numbers can be used to constrain the interior compositions of planets (Moulik and Ekström; 2025a; Garcia et al.; 2019).

There are three bodies in hydrostatic equilibrium in the universe for which humans have obtained seismographic readings and thus direct observations of interior structure profiles have been attained: the Earth, Mars, and the Moon. Here we demonstrate our model's acceptable treatment of all of them.

Three additional solar system bodies have non-seismographic but relatively strong constraints on their interior structures from their moments of inertia and additional geophysical arguments. We also demonstrate our model's acceptable treatment of all of them.

We particularly note the importance of replicating planetary Moment of Inertia (MoI) coefficients (C), which summarize the mass distribution of planetary interiors. Solely focusing on reproducing planetary radii can lead to cases wherein a model that systematically overpredicts densities in one region and underpredicts them in another appears to perform well, but such a model would likely not extrapolate beyond the mass regimes of the planets that it was validated on (typically Earth). We derive our model C as well as MoI coefficients (MoIC) for planets with available seismographic profiles by numerically integrating Eq. 2.48 (derived by combining the differential MoI of a spherical shell and

Eq. 2.1) using `scipy.integrate.trapezoid` for our computed $r(\rho)$ profile of Earth's interior.

$$C = \frac{8\pi}{3M_p R_p^2} \int_0^{R_p} r^4 \rho(r) dr \tag{2.48}$$

The lower C is, the more mass is concentrated toward the planetary center and thus the more differentiated the planet is. In the edge case of a constant-density sphere, $C = 0.4$.

MoI and thus C can be attained without a seismographic constraint on the interior structure of a body either by precisely measuring its precession (as for Venus (Margot et al.; 2021) and Mars (Konopliv et al.; 2020)), using spacecraft-derived constants related to the shape of its gravitational field and measuring its libration (C_{22} and J_2, as for the Moon (Williams et al.; 2014)), or by using the Darwin–Radau equation to infer C from a spacecraft-derived constant related to the shape of its gravitational field and the relationships between MoI about different axis (as for Europa (Anderson et al.; 1998); the constant is C_{22}; requires that the object is in the Cassini state, where the spin axis, orbit precessional axis, and normal to its orbital plane are all in the same plane (Peale et al.; 2002); MoI about different axis determined via flattening as in Anderson et al. (1998) or from obliquity as in Genova et al. (2019)).

Throughout this Section, we will be using the notation X (Y%; Z) to notate a value of X with an error of Y from the real value ($Y\% = 100(X_{\text{Model}} - X_{\text{Observed}})/X_{\text{Observed}}$) that is Z σ from the real value. We only list Z if the uncertainty in the true value is high, as is the case for the latter three bodies in our validation sample but not the first three.

2.3.1 Earth

In Figure 2.4 we compare our model constructed using Earth's known composition to the interior of the Earth as reported in the one-dimensional Reference Earth Model (REM1D), a model representing the consensus of the seismographic community (Moulik and Ekström; 2025a,b). REM1D is a spherically-averaged model of the interior structure of Earth derived from wave travel times, Earth's normal modes, and its bulk properties (e.g mass, radius, moment of inertia) (Moulik and Ekström; 2025a,b). REM1D is an update to PREM by Dziewonski and Anderson (1981). PREM has found extremely wide use in the geophysics community (Stacey and Davis; 2008), with extrapolations from it being used in previous super-Earth mass-radius relations (Zeng et al.; 2016, 2019). The $\frac{\chi^2}{N}$ (where N is the number of parameters in the model) of REM1D's model Earth mass, moment of intertia, and C compared to observations is 0.12, making it the only reference

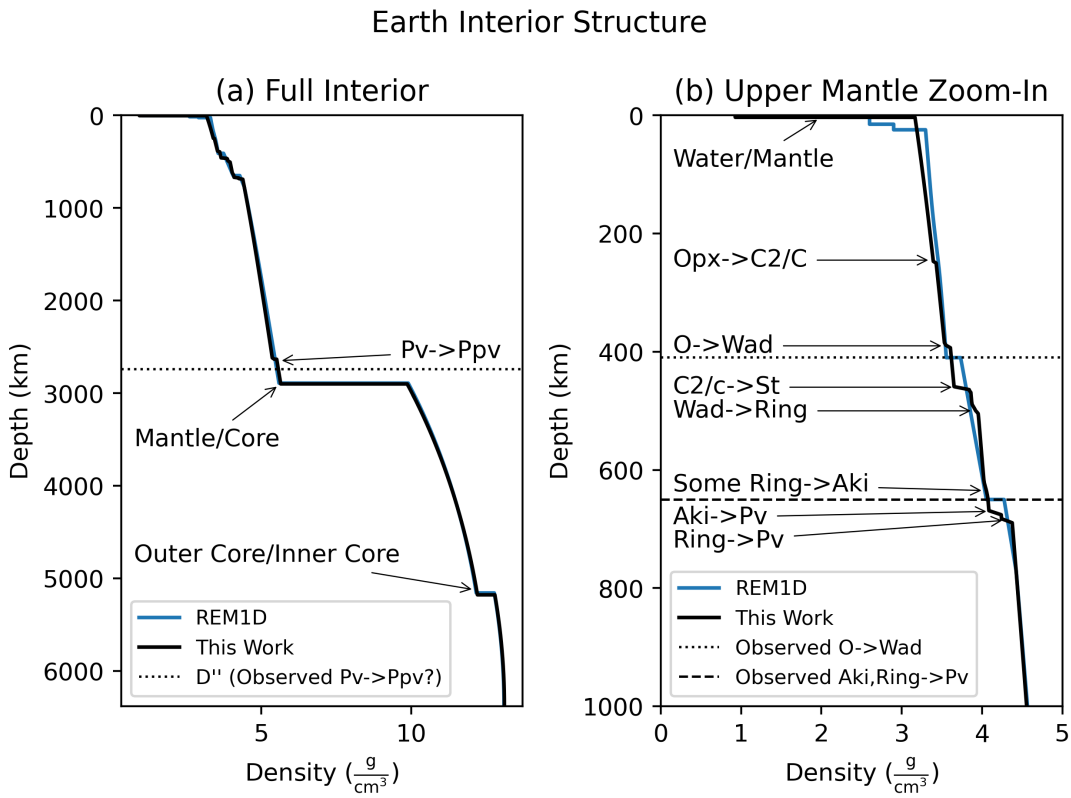

FIGURE 2.4: The internal r-ρ profile of Earth as determined by the model in this work as compared to REM1D, a reference model for the Earth derived from seismology and other constraints. Horizontal lines indicate the observed locations of phase transitions in Earth's interior (although note that the association of D'' with the Pv->Ppv transition is not universally accepted). More controversially observed phase transitions are discussed in the text. Annotations indicate phase transitions and boundaries between layers. For phase transitions, the format is lower pressure phase -> higher pressure phase. For boundaries between layers, the format is lower pressure layer/higher pressure layer. Note that multiple phases coexist throughout the mantle, the labeled phases represent a transition only for some subset of mantle material. Opx is short for Orthopyroxene. C2/c is short for Clinopyroxene. O is short for Olivine. Wad is short for Wadsleysite. St is short for Stishovite. Ring is short for Ringwoodite. Aki is short for Akimotoite. Pv is short for Perovskite. Ppv is short for Post-Perovskite. Note that this is for a spherically averaged Earth and both the density profile and mineralogy may change with latitude and longitude. All mantle EOS above the Pv->Ppv transition are from HeFESTo solved using Perple_X (Stixrude and Lithgow-Bertelloni; 2024; Connolly; 2009). See text for in-depth discussion.

Earth model consistent with these parameters at the 1σ level (c.f PREM 21 (Dziewonski and Anderson; 1981), AK135 117 (Kennett et al.; 1995), AK135F 195 (Montagner and Kennett; 1996)), motivating our adoption of it (Moulik and Ekström; 2025b). The difference between the densities of REM1D and PREM is small but nonzero (a maximum of 0.5%, generally much lower) (Moulik and Ekström; 2025b). REM1D reports the density of the Earth as a series of piecewise functions between several discontinuities (discussed below) (Moulik and Ekström; 2025a).

Our model Earth has a radius of 1.0015 $R_\oplus$ (0.15% error v. actual Earth). If we set $w_{\mathrm{H_2O}} = 0$ and neglect rotation to compare our model to those in the literature, we get an Earth radius of 1.0006 $R_\oplus$ (0.06% error v. actual Earth). To the best of our knowledge, this is the closest replication of Earth's radius in any interior structure model built for application to exoplanets that is not explicitly constructed using Earth's interior structure[13] (see Section 2.5.2 for more comparison to the literature). It is thus clear that our model's replication of Earth's radius is nearing the level of accuracy at which uncertainty in its input parameters dominate.

We find $C = 0.33018$, giving -0.160% error compared to Earth (Moulik and Ekström; 2025a). If we used the rounded values typical of the literature of $w_{Core} = 0.325$ and $w_{H_2O} = 0$, we would have a model Earth MoIC of 0.33040 (-0.094%). For comparison, the Preliminary Earth Reference Model (PREM) has an Earth $C = 0.33090$ (0.055%) (Dziewonski and Anderson; 1981). Our MoIC is thus of comparable accuracy to that derived from seismology. The uncertainty in the measurement of Earth's MoIC itself is 0.007%, dominated by uncertainty in the value of G (Moulik and Ekström; 2025a). The error in our replication of the distribution of Earth's interior structure is thus only an order of magnitude from its theoretical floor. We emphasize that this was achieved with no explicit attempts to fit this variable.

The bulk composition of the silicate Earth (core+mantle)–also known as the primitive mantle (primitive referring to the mantle composition before the crust is differentiated)– is not exactly constrained (Palme and O'Neill; 2014). We follow Palme and O'Neill (2014)'s literature review, which constrains x_{FeO}, x_{MgO}, and x_{SiO_2} from measurements of rocks from the upper mantle as well as cosmochemical abundances. We account for our non-inclusion of Ca, Al, and other elements by forcing the molar ratios of Mg/Si and Mg/Fe to reflect reality. The resulting fractions are $x_{MgO} = 0.512$, $x_{SiO_2} = 0.425$, and $x_{FeO} = 0.063$ (c.f $x_{MgO} = 0.521$, $x_{SiO_2} = 0.417$, and $x_{FeO} = 0.062$ from McDonough

[13]Zhang and Rogers (2022) report a $< 0.1\%$ discrepancy and cannot be correctly compared to this study as no exact number is quoted.

and Sun (1995); $x_{MgO} = 0.528$, $x_{SiO_2} = 0.409$, and $x_{FeO} = 0.063$ from Workman and Hart (2005); $x_{MgO} = 0.519$, $x_{SiO_2} = 0.423$, and $x_{FeO} = 0.058$ from Haldemann et al. (2024)) (McDonough; 2016).

We now compare the density jumps in our model to those observed on Earth. Density jumps arise from phase and composition transitions. Rapid increases in density in REM1D at less than 25 km correspond to the transition from the water layer to the mantle, modeled here, and the crust, not modeled here. The largest density jump corresponds to the transition between Earth's mantle and core and great agreement can be observed between our model and REM1D. The second largest density jump at a greater depth corresponds to the transition between Earth's liquid outer core and solid inner core, where we again find agreement between our model and REM1D (although note that our melting temperature of Fe was selected for this purpose, see Section 2.2.6).

Earth's mantle has two widely-accepted density jumps included in REM1D (Moulik and Ekström; 2025a,b). The first is at a depth of 410 km and corresponds to the transition between $(Mg,Fe)_2SiO_4$ olivine and $(Mg,Fe)_2SiO_4$ wadsleyite (Helffrich; 2000; Cormier et al.; 2023; Moulik and Ekström; 2025b). The second is at a depth of 650 km and corresponds to the transition between between $(Mg,Fe)_2SiO_4$ ringwoodite (wadsleyite transitions to ringwoodite at intermediate depths but this does not cause a large density jump, see below) and $(Mg,Fe)SiO_3$ perovskite Helffrich (2000); Shim et al. (2001); Cormier et al. (2023); Moulik and Ekström (2025b). Both of these transitions are recovered in our model, with the 410 km jump at 390 km and the 650 km jump at 685 km.

Between these two jumps, our model finds three additional mantle density jumps not included in REM1D. The shallowest and largest at 460 km is caused by SiO_2 transitioning from the coesite to stishovite phase, which is invoked as the cause of a phase transition observed at varying depths around 300 km in some locations known as the X-discontinuity (Revenaugh and Jordan; 1991; Kemp et al.; 2019; Srinu et al.; 2021). Given the distance between the location of our model jump and the X-discontinuity, we believe that this transition is at the wrong depth and invoke the non-treatment of the Earth's crust, our simplified chemical inventory, and Earth's heterogeneous interior as reasons for this.

The next upper mantle density jump at 500 km is associated in our model with the phase transition from wadsleyite to ringwoodite, which must occur between the 410 km olivine to wadsleyite transition and 650 km ringwoodite to perovskite transition to

supply the ringwoodite for that transition. A jump at this depth is found in some regions on Earth (Shearer; 1996; Zhang et al.; 2022; Tian et al.; 2020; Cormier et al.; 2020).

The deepest of these jumps at 635 km is caused in our model by the appearance of (Mg,Fe)SiO_3 akimotoite. Cormier et al. (2023) have found that heterogeneities in Earth's mantle peak at around this depth and attribute this to the topography of a phase transition (i.e waves are bouncing off a surface of the phase transition with a depth that varies with latitude and longitude due to varying composition and temperature profiles).

Our model contains one mantle density jump above the 410 km jump at 245 km due to the transition of (Mg,Fe)SiO_3 from the opx to C2/c phase (Stixrude and Lithgow-Bertelloni; 2005; Woodland; 1998). This location is consistent with the ∼300 km X-discontinuity observed at varying depths at some locations, however, the depth variability and the fact that such a transition would be difficult to detect indicate that the X-discontinuity is likely caused by either a non-phase-transition mechanism or the transition of SiO_2 from the coesite to stishovite phase (which occurs at greater depths in our model), so this is likely coincidental (Revenaugh and Jordan; 1991; Kemp et al.; 2019; Srinu et al.; 2021).

Our deep mantle contains a density jump at 2650 km associated with the transition of (Mg,Fe)SiO_3 perovskite to (Mg,Fe)SiO_3 post-perovskite that is not included in REM1D. Although no observed density jump occurs at this depth, it is near the top of the well-attested D'' layer, a region where the slope of wave velocities with depth abruptly changes (Moulik and Ekström; 2025b). This change in velocities has been associated with the perovskite to post-perovskite phase transition (Tsuchiya et al.; 2004), although it has also been associated with a magma ocean at the base of Earth's mantle that either still exists or has since solidified and left behind a layer enriched in light elements (Labrosse et al.; 2007; Hu et al.; 2024).

There are three reasons that our model may contain a density jump in the lowermost mantle while REM1D does not. The first is that the lowermost mantle appears chemically stratified as evidenced by its changing value of K' and thus a change in chemical composition not included in our model depresses densities in the real Earth's lowermost mantle (Moulik and Ekström; 2025b). The second is that post-perovskite could not be a universal feature in the lowermost mantle and only appears at certain locations (Moulik and Ekström; 2025b; Houser; 2007). The third is that post-perovskite does not form in Earth's lowermost mantle or forms less readily than we predict for one of two reasons: (1) elements such as Al that are not considered here push the pressure at

which a system becomes pure post-perovskite higher (Catalli et al.; 2009; Stixrude and Lithgow-Bertelloni; 2024) and/or (2) the increase in temperature in our model between the mantle and the core happens instantaneously at the top of the core, whereas in reality the lowermost regions of the mantle have a super-adiabatic temperature curve, making it more difficult for post-perovskite to form, potentially causing a double transition in which post-perovskite forms at some depth and then returns to perovskite at even greater depths (Hernlund and Labrosse; 2007).

To conclude, our model replicates Earth's radius and C from its known mass and composition with extreme accuracy (<0.2%). It also includes jumps in density at the correct locations for Earth's mantle-outer core and inner core-outer core boundary as well as phase transitions occurring within the mantle.

2.3.2 Mars

We compare our model Mars to Mars' profile derived from the InSight seismometer– which landed on the Martian surface in 2018–in Figure 2.5 (Banerdt et al.; 2020; Khan et al.; 2023). We present a profile (1) using a mantle minerology with a composition derived from Martian meteorites following Yoshizaki and McDonough (2020) ($x_{MgO} = 0.444$, $x_{SiO_2} = 0.438$, and $x_{FeO} = 0.118$, broadly consistent with other estimates of Mars' mantle composition such as Khan et al. (2022), see review by Kuskov et al. (2024)) and a Martian core with abundances selected to match InSight's results ($x_s^l = 0.03$, $x_O^l = 0.42$)[14]; (2) using a Martian mantle composition and core abundances fit to Earth's core; (3) using Earth's mantle composition and core abundances fit to Mars' core; and (4) using Earth's mantle composition and core abundances. In all cases, we use a Martian core mass fraction from Khan et al. (2023) of 0.21. This is lower than the previously accepted value of 0.25 as in Le Maistre et al. (2023); Khan et al. (2022) due to Khan et al. (2023)'s discovery of a molten layer at the base of the Martian mantle that was previously identified with Mars' liquid outer core. We get Martian radii of $0.5333R_\oplus$ (0.24%), $0.5288R_\oplus$ (-0.60%), $0.5371R_\oplus$ (0.95%), and $0.5327R_\oplus$ (0.13%), respectively. We get Martian Moment of Inertia coefficients of 0.36195 (-0.398%), 0.35476 (-2.377%), 0.36199 (-0.387%), and 0.35489 (-2.341%), respectively. In all cases, we find an entirely liquid core–as is currently understood to be the case for Mars (Le Maistre et al.; 2023; Khan et al.; 2023)–and a core radius near the results from InSight (for the fiducial case 1, it is fully consistent with seismographic results). Mars' lack of a magnetic field despite its entirely liquid core has been explained by a lack of convection within its interior and

[14] As our EOS for liquid FeS is for $Fe_{81}S_{19}$, high values of x_s^l deplete all free Fe. Thus, for planets with high light element compositions like Mars, x_S^l must be lowered to accommodate high x_O^l.

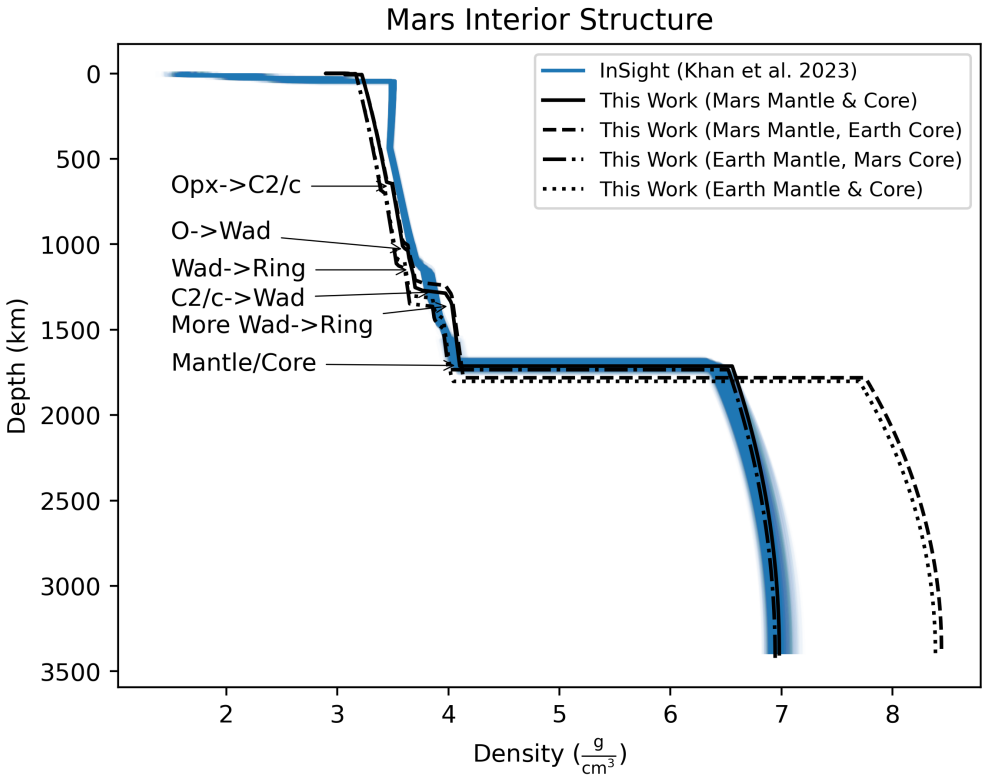

FIGURE 2.5: The internal r-ρ profile of the Mars as determined by the model in this work compared to the inversion of InSight seismic data from Khan et al. (2023). Khan et al. (2023) provide 1000 models consistent with Martian observations, all of which are plotted with some transparency such that darker shades of blue represent regions where more models agree. We plot four Mars models with each possible combination of Mars/Earth Mantle/Core chemical abundances (see text). See Figure 2.4 caption for abbreviations and formatting of annoations. Annotations are for the fiducial Mars Mantle & Core Case (Case 1).

a stratification between H-rich and S-rich layers of the core, effects not included within our model (Hemingway and Driscoll; 2021; Yokoo et al.; 2022; Yokoo and Hirose; 2024). We do not recover a molten liquid mantle layer as our model's simplified prescription for the temperature jump at the mantle-core boundary does not increase temperatures in the lowermost mantle as occurs in reality.

That all details of the differences between Earth and Mars' compositions lead to radii differences $\lesssim 1\%$ indicates the ability to extrapolate Earth-like compositions as broadly indicative of terrestrial planets in simple estimates like mass-radius diagrams while simultaneously illustrating the difficulty of inferring planet compositions from their bulk densities.

It is of interest that using the chemical composition of Earth reproduces Mars' radius better than using the chemical composition of Mars. An investigation of the MoIC reveals that using Mars' chemical composition yields an order of magnitude more accurate result, indicating that the replication of Mars' mantle when using Earth's composition is the result of a systematic underprediction in mantle density being counteracted by a systematic overprediction in core density.

The light element fractions we require in the Martian core correspond to a Fe weight abundance of 80%, $\sim 5\%$ lower than the lower bound provided by Khan et al. (2023). This is likely a product of our limited chemical inventory as well as a simplified mantle structure leading to an inaccurate outer pressure boundary condition for the core. The density of our model's core moving with increasing depth from being on the denser to lighter end of Khan et al. (2023)'s retrievals is a potential sign of our inaccurate elemental abundances.

Our model's systematic underprediction of density in the upper $\sim$500 km of the Martian interior corresponds to the Martian lithosphere, which has a conductive profile starting from the temperature of the Martian surface rather than an adiabatic profile starting at the melting temperature of the Martian mantle and is thus much colder (and therefore denser) in reality than in our model (Khan et al.; 2022, 2023). As planets increase in mass, their Rayleigh numbers increase, shrinking the size of their lithospheres (Foley et al.; 2020; Valencia et al.; 2007; Howard; 1966), so the inaccuracy of our simplified temperature prescription becomes increasingly small. The cancelling out of errors when assuming an Earth-like composition for Mars thus disappears, illustrating the importance of constructing models that replicate planetary interior structures broadly rather than just their radii.

2.3.3 The Moon

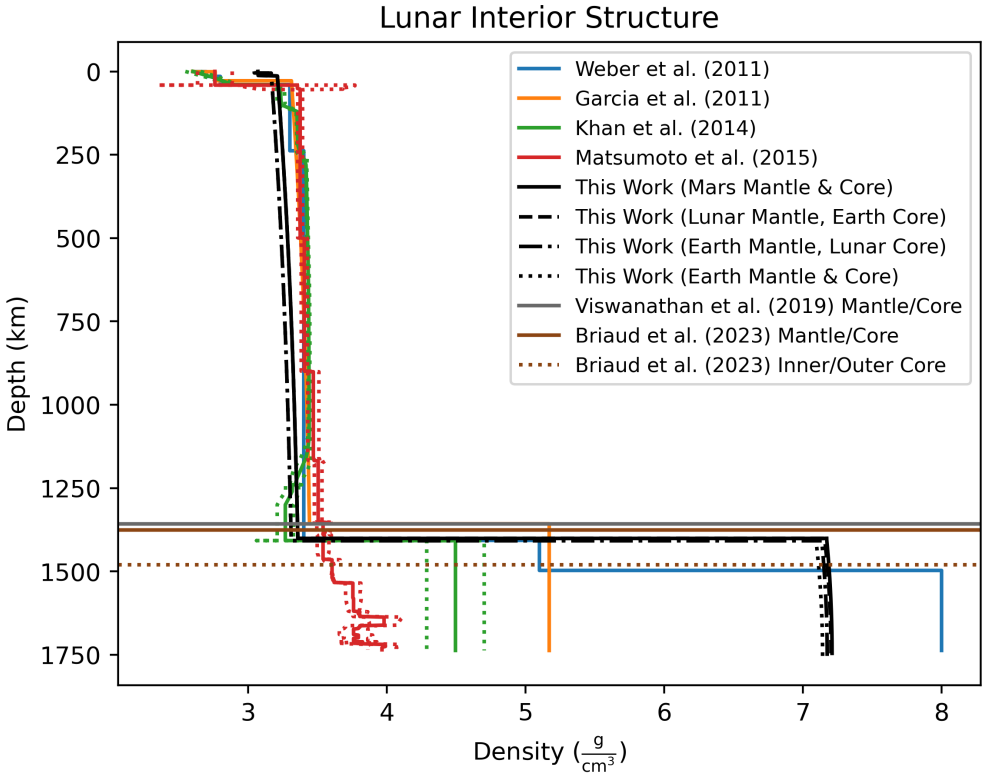

FIGURE 2.6: The internal r-ρ profile of the Moon as determined by the model in this work and found in various models of the lunar interior informed by seismology. Dotted lines indicate errors where applicable. Horizontal lines correspond to lunar core radii from other considerations (Viswanathan et al. (2019): the oblateness of the lunar core, Briaud et al. (2023): lunar tidal deformation). The format of boundaries between layers is lower pressure layer/higher pressure layer. Colours are arbitrary.

Seismic data on the moon has been collected by seismometers placed by the Apollo space program that were active until 1977 (Nunn et al.; 2020). A new seismometer was recently placed on the Moon as part of the Chandrayaan-3 mission but has not yet collected adequate signals to construct an interior structure model (John et al.; 2024). The Moon has no widely-accepted internal structure model like PREM or REM1D and thus we compare our model to a range of lunar interior structure models in Figure 2.7 We do not recover this liquid mantle layer as our model's simplified prescription for the temperature jump at the mantle-core boundary does not increase temperatures in

the lowermost mantle as occurs in reality.(Weber et al.; 2011; Garcia et al.; 2011; Khan et al.; 2014; Matsumoto et al.; 2015; Garcia et al.; 2019), each model differing in data analysis and input data. We note that Weber et al. (2011) does not include data on the bulk Moon and thus we disfavor it, however its inclusion of a solid core is supported by Briaud et al. (2023), who argue that a solid inner core is needed to reproduce the moon's observed tidal deformation. Constraining the lunar interior at depths greater than ∼1200 km with seismology is difficult, hence the divergence of our reference models at this depth (Nunn et al.; 2020). We take the Moon's core mass fraction as 1.68%, the median of values reported by Viswanathan et al. (2019) derived from the oblateness of the Moon's core inferred from lunar laser ranging (precisely measuring distances to locations on the lunar surface using laser round-trip travel times). This value is slightly above the 1.5% core mass fraction that had been reported as an upper bound from analysis of data from the GRAIL spacecraft (Williams et al.; 2014).

We obtain the bulk FeO and MgO of The Moon from Taylor et al. (2006)'s estimates from geochemistry and the seismographically-derived lunar mantle density. We then assume that all non-Feo non-MgO material is SiO_2 as the Mg/Si of the Moon is poorly constrained (Taylor et al.; 2006). This results in $x_{MgO} = 0.468$, $x_{SiO_2} = 0.428$, and $x_{FeO} = 0.104$. These values are broadly consistent with other geophysical as well as geochemical lunar mantle composition estimates (Khan et al.; 2014; Kuskov et al.; 2024; Sossi et al.; 2024), with the exception of $x_{SiO_2} = 0.428$, which is an overestimate due to it representing all non-MgO-non-FeO materials.

In Figure 2.7, we present lunar profiles (1) using the lunar mantle mineralogy of Taylor et al. (2006) and a lunar core with Earth-like abundances in the liquid and a sufficiently high x_s^s to be entirely liquid ($x_s^s = 0.3$, $x_s^l = 0.3$,$x_O^l = 0.09$); (2) using the lunar mantle composition and the core abundances fit to Earth's core; (3) using Earth's mantle composition and core abundances fit to the lunar core as in case 1; and (4) using the Moon's mantle composition and core abundances. We get lunar radii of $0.2740R_\oplus$ (0.49%), $0.2740R_\oplus$ (0.49%), $0.2752R_\oplus$ (0.94%), and $0.2752R_\oplus$ (0.94%), respectively. We get lunar Moment of Inertia coefficients of 0.39424 (0.286%), 0.39424 (0.288%), 0.39441 (0.329%), and 0.39442 (0.334%), respectively.

We set core parameters to obtain purely liquid cores because all models we consult find at least a partially liquid core. We do not attempt to recreate an outer/inner core transition because the slope of the temperature in the core is generally steeper than the slope of the melting curve. This would indicate that our model moon would have an outer solid core and liquid inner core. In our model, this would result in a higher-density

layer overlying a lower-density layer, an unphysical situation that we avoid, so we restrict x^s_S to values where this does not occur; however, this result does have physical meaning that we discuss in Appendix A5.

Our model underpredicts densities throughout the lunar mantle even when accounting for its higher Fe content than the Earth, indicating either an inaccurate temperature profile as for Mars, the use of an inaccurate composition of the mantle, or the mantle being in the wrong phase, potentially due to elements not included in our formalism. The solutions with lunar cores have liquid cores and the solutions with Earth cores have solid cores. The extremely close densities of the liquid and solid phases likely indicates that Ichikawa and Tsuchiya (2020)'s EOS for liquid FeS and FeO do not extrapolate down to the few GPa pressures of the Moon's mantle well.

We recover a core radius of 345 km, which is only -1.15σ from the 362 km radius reported by Briaud et al. (2023), and is thus consistent with the true lunar radii, if not in the middle of plausible values.

2.3.4 Venus

Current constraints on Venus' C are consistent with Earth's but too weak to further constrain interior structure models (Margot et al.; 2021; Shah et al.; 2022). We thus assume a composition of Venus' mantle and core identical Earth's, but a slightly lower w_{Core} of 0.3 near the median of the distribution reported by Shah et al. (2022). We calculate a Venus radius of $0.9497R_\oplus$ (-0.016%) and a Venus MoIC of 0.33468 (-0.097%), within 0.1σ of Venus' measured MoI. As Shah et al. (2022) derived Venus' interior from Venus' MoI, this good fit is not the result of an independent constraint as is the case for planets with seismographic constraints. Following this concern, we also tested Venus as having the exact same parameters as Earth besides its rotational period and mass. This resulted in a radius of $0.9447R_\oplus$ (-0.55%) and MoIC of 0.33247 (-1.343%), within 0.2σ of the measured MoIC.

The comparison of these two answers serves as an important constraint: Venus is the planet with the most Earth-like composition for which we have in situ measurements that is not itself the Earth. Venus is thus a test case for the broad extrapolatory power of the Earth. Although our results assuming an Earth-like composition for Venus are close to reality, it should be kept in mind that the smallest compositional difference between planets for which we have in situ measurements represents a radius change at the half-%

level. As Earth and Venus orbit the same star, this reflects a minimum scatter in radius arising from concerns beyond the host star and planetary mass.

Better measurements of Venus' MoIC from the EnVision and VERITAS missions–with planned launches between 2028 and 2031–are expected to provide stronger constraints on how well our model replicates Venus and how close Venus' composition is to Earth's (Cascioli et al.; 2021; Rosenblatt et al.; 2021; Widemann et al.; 2022).

2.3.5 Mercury

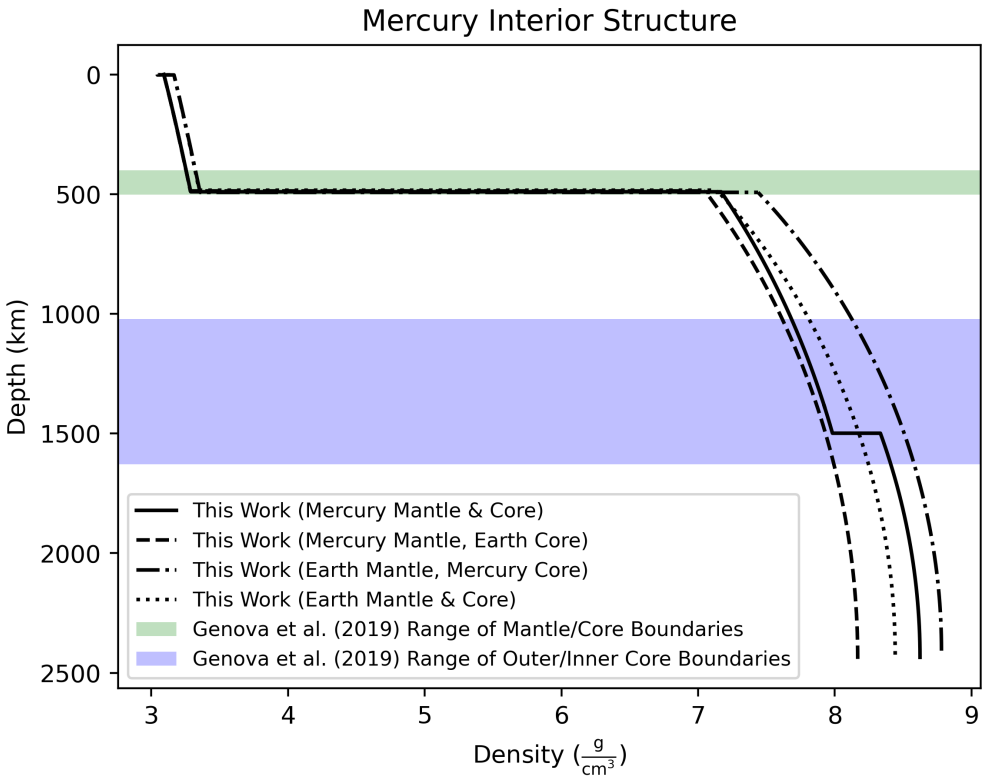

FIGURE 2.7: The internal r-ρ profile of Mercury as determined by the model in this work compared to the plausible locations of Mercury's mantle/core and inner/outer core transitions from Genova et al. (2019), indicated by horizontal shaded regions. The format of boundaries between layers is lower pressure layer/higher pressure layer. The inner/outer core transition boundary is 0.4-0.7 times the core radius following Genova et al. (2019), the core radius comes from their Figure S9d, the closest model to ours. Note that the shaded region indicates a 3σ spread. Colors are arbitrary.

Although no seismic data exists for Mercury, Mercury's core does not librate due to solar torques while Mercury's mantle does, allowing MoIC for the mantle and core to be determined separately, giving a constraint on its interior (Peale et al.; 2002; Margot et al.; 2012). Additionally, surface features on Mercury such as ridges indicate that the planet has contracted (Byrne et al.; 2014). These pieces of evidence and Mercury's low MoIC provide evidence for a a solid inner core (Genova et al.; 2019).

We take $x_{\mathrm{MgO}} = 0.532$, $x_{\mathrm{SiO_2}} = 0.466$, and $x_{\mathrm{FeO}} = 0.002$ following Fischer and Parman (2025), which assumes that Mercury has a composition similar to Enstatite chondrite but with somewhat lower Si fractions.

We take the core mass fraction of Mercury as 0.7136, resulting from taking a Mercury core radius of 1975 km and bulk density of 7300 kg/m^3. The core radius is that inferred by Genova et al. (2019)'s interior structure models built to match Mecrury's MoIC and fractional MoIC from the core. The core density is within the plausible range retrieved by Genova et al. (2019).

We present density profiles of Mercury (1) using the Mercury mantle mineralogy of Fischer and Parman (2025) and a core with the right composition ($x^s_{\mathrm{S}} = 0.06$, $x^l_{\mathrm{S}} = 0.19$, indicative of extreme partitioning) to result in a liquid/solid core transition within the radii predicted by Genova et al. (2019) (0.4-0.7 times the favored outer core radius of $\sim$1988 km from their supplemental Figure S9d which most directly matches our interior model, a slightly larger radius than their overall preferred radius); (2) using Mercury's mantle composition and core abundances fit to Earth's core; (3) using Earth's mantle composition and core abundances fit to Mercury's core; and (4) using Mercury's mantle composition and core abundances. We get Mercurian radii of $0.3822R_\oplus$ (-0.17%), $0.3833R_\oplus$ (0.11%), $0.3779R_\oplus$ (-1.31%), and $0.3805R_\oplus$ (-0.62%), respectively. We get Mercurian Moment of Inertia coefficients of 0.33575 (0.826%; 1.65), 0.33744 (1.332%; 2.661), 0.33392 (0.277%; 0.554), and 0.3369 (1.172%; 2.341), respectively.

Experiments at conditions similar to Mercury's core indicate that nearly all S partitions into the liquid core while Si partitions nearly evenly into the liquid and solid cores (Pommier; 2025; Tao and Fei; 2021), indicating that our model's S in the solid core is actually representing another light element. This light element is likely not Si, as Si reduces core melting temperatures inefficiently and our required light element abundance arises from the need to reduce the core melting temperature (Knibbe et al.; 2025).

Our finding of a partitioning between Mercury's inner and outer cores is in apparent

contradiction with Mercury's observed magnetic field, which gives no hint of the compositional convection that would be anticipated from such a scenario (Knibbe et al.; 2025; Manglik et al.; 2010; Takahashi et al.; 2019).

The BepiColombo spacecraft, which is scheduled to arrive in orbit around Mercury in November 2026 (Sánchez-Cano et al.; 2025), will provide a stronger constraint on Mercury's MoIC (Benkhoff et al.; 2021), helping to shine light on the exact makeup of Mercury's interior and advance the understanding of its unique-in-the-solar-system high core mass fraction regime.

2.3.6 Europa

Although no seismic data exists for Europa, measurements of its moment of inertia from the Galileo spacecraft coupled with its low gravity leading to a relatively constant density water (solid and liquid) layer allows some constraints to be placed on its interior composition (Petricca et al.; 2025; Gomez Casajus et al.; 2021). Europa's small inferred core (see below) also reduces the available parameter space, allowing compositional inferences from MoIC (Petricca et al.; 2025). We follow the interior structure model results of Petricca et al. (2025) and adopt for Europa $w_{H_2O} = 0.074$, $x_{MgO} = 0.375$, $x_{SiO_2} = 0.353$, and $x_{FeO} = 0.272$. This results in a very low $MgSiO_3$ fraction that causes Eq. 2.22 to break, so we set our melting temperatures to what they would be for an Earth-like mantle composition. Petricca et al. (2025) do not find a strong constraint on w_{Core}, we take their approximate median core radius and density to find $w_{Core} = 0.0045$ and use Earth's core's chemical composition. Using Europa's measured A_B of 0.68 (Grundy et al.; 2007), we find a Europa radius of $0.2486 R_\oplus$ (1.48%) and MoIC of 0.35617 (0.416%; 0.615σ) when calculating Europa's surface temperature from its solar instellation (as would be the case for an exoplanet). We do not produce a liquid ocean, likely due to the neglect of tidal heating, assuming a purely convective thermal structure in the ice layer, and ignoring the impact of any impurities on the melting temperature. If we instead use the insight that Europa's ice shell has a radius of $\lesssim$ 25 km (Nimmo and Giese; 2005; Schenk et al.; 2008; Cox and Bauer; 2015; Vilella et al.; 2020), comparable to the radius of Earth's neglected crust, and set the outer boundary of the water layer to the melting point of water–similar to how we treat the mantle–we get a radius of $0.2472 R_\oplus$ (0.89%) and MoIC of 0.36011 (1.526%; 2.256σ). We take the latter case as fiducial while emphasizing that our failure to replicate a subsurface ocean in the first case indicates that our model is not applicable for detailed characterization of small icy bodies. The relatively high error even when forcing the water layer into the right state is also likely a

reflection of our inability to calculate a proper melting temperature, potentially leading to an interior that is far too hot.

The Europa Clipper mission will reach an orbit around Jupiter in April 2030 and will collect measurements of Europa's induced magnetic field and love number (Pappalardo et al.; 2024; Roberts et al.; 2023). Love numbers determine the response of a body to tidal forcing and are thus particularly effective for Europa due to Jupiter's extreme tidal forcing (Pappalardo et al.; 2024). These will provide better constraints on Europa's interior that could be compared against the predictions presented here.

2.3.7 Summary

Our model generates radii and moment of inertia coefficients within 0.5% or 2σ of the true values for Earth, Mars, the Moon, Venus, and Mercury. We replicate Europa's radius and moment of inertia to within 1% or 3σ. In addition, the core radii of Earth, Mars, the Moon, and Mercury are completely consistent with reality, only off by 1.16σ from other estimates at worst. The outer/inner core transitions of Earth and Mercury (but not of the Moon) are replicated. Both unambiguous density jumps within Earth's mantle are replicated to within 35 km, and several other density jumps consistent with at least some theories of the Earth's interior are present. Where our model is discrepant with seismographic constraints, the chief explanation tends to relate to physics and geophysics occurring at masses below Earth's, so the small errors that are found in the model will be unimportant for the vast majority of the exoplanetary population.

Having demonstrated our model's accuracy, we apply it to calculate mass-radius relations for the exoplanet population.

2.4 Mass-Radius Curves

2.4.1 New Mass-Radius Relations

The isocompositional mass-radius (MR) relations from our new interior structure model are presented and compared to the exoplanetary population in Figure 2.8. We consider seven compositions, from least dense to most dense for Earth-like masses and temperatures: H/He-enveloped (1% H/He+99% Earth-like), Water world (50% H_2O+50% Earth-like), pure mantle (100% mantle with Earth-like abundances), Earth-like, Mercury-like (see section 2.3.5), Earth-like core (100% core mass fraction) with Earth-like abundances, and a 100% pure iron core. Curves for different temperatures are provided

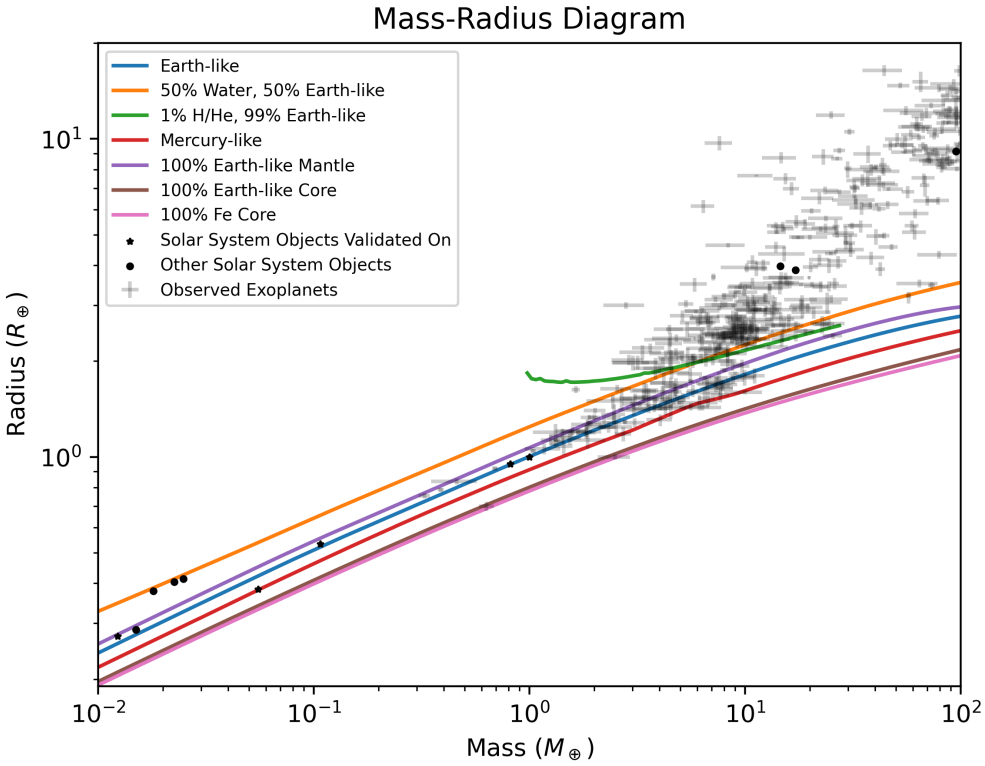

FIGURE 2.8: The isocomposition curves in mass-radius space for several planetary compositions. See text for further elaboration on compositions. The background error bars are the observed exoplanet population via `https://exoplanetarchive.ipac.caltech.edu/`, retrieved on August 29, 2025. The dots are solar system objects (both moons and planets), with stars being the six objects within our validation sample. Note a discrepancy: solar system planetary radii are actual radii while exoplanet radii are transit radii (see section 2.2.8 for the difference).$M \sin i$ is converted into M by assuming an average i where applicable. No debiasing is applied. Radii and mass uncertainties restricted to below 8% and 25%, respectively, following Otegi et al. (2020). Our observed planet sample contains no planets consistent with extended gaseous envelopes with masses below $M_\oplus$ so we do not generate H/He-rich isocompition curves to such low masses. All of our model data used to make this figure is available at `https://github.com/Bennett-Skinner/SkinnerPudritzCloutier2025-MR-curves/`.

below. All mass-radius datapoints are available for download at `https://github.com/Bennett-Skinner/SkinnerPudritzCloutier2025-MR-curves/`.

For consolidated compositions, we generated 200 model planets for these compositions log-uniformly spaced between 0.01 and 100 $M_\oplus$ and thus our mass resolution is only as high as any two model planets are far apart in mass space ($0.04M_\oplus$ at the low end of this mass range and $0.37M_\oplus$ at the high end of this mass range). For compositions with extended envelopes, we only generate curves above $M_\oplus$, where surface gravities are generally within the range appropriate for application of the temperature profiles of Parmentier and Guillot (2014); Parmentier et al. (2015) (see section 2.2.7). We consider these compositions to bracket the parameter space of super-Earths and sub-Neptunes. We include higher-mass versions of terrestrial objects only for Earth and Mercury because those are the only objects with constrained liquid and solid core compositions, whereas for most solar system objects only liquid core compositions are known.

We immediately note that–as demonstrated in Section 2.3–the Earth-like compositional curve passes very close to Earth, Venus, and Mars, the Mercury-like compositional curve passes very close to Mercury, and the pure mantle curve passes nearby the Moon, as expected from its very low core mass fraction. Beyond the validation sample, Io is consistent with a rocky interior, while Ganymede, Titan, and Callisto are consistent with half-water interiors, in agreement with observation and with theories of Galilean moon formation (Heller and Pudritz; 2015; Shibaike et al.; 2019).

Broadly, isocomposition curves for predominantly solid bodies follow power laws $M = aR^b$ at masses a few times Earth's. These curves are roughly parallel. As mass increases, compression within the planetary interior becomes increasingly important, resulting in an increasingly flat power law. All power-law M-R curves thus eventually degrade. Planets with significant gaseous envelopes–be they H/He or steam–experience a flattening of the M-R relationship at masses $\lesssim 2M_\oplus$ as the total mass of the planet becomes inadequate to hold onto the surrounding tenuous atmosphere. Planets with masses and radii consistent with being in this flattening region are rare (and none meet the mass and radius precision cutoff we set in our figures), indicating that such a scenario is not viable long-term, with either such tenuous materials never being accreted, rapidly being lost, or the planet cooling to sufficient temperatures. Planets with masses above $\sim 10-20\,M_\oplus$ always have densities less than a planet of that mass made of pure Earth composition mantle material, indicating that they are highly likely to be volatile-enhanced. This is in agreement with predictions of gas accretion and pebble isolation masses from planet formation theory and conforms to the apparent masses of the cores of Jupiter and Saturn (Bitsch et al.;

2019; Lambrechts et al.; 2019; Wahl et al.; 2017; Mankovich and Fuller; 2021; Howard and Guillot; 2023).

At the sub-Earth masses mostly probed by solar system objects, we see a clear differentiation between the broadly Earth-like compositions of Earth and Venus, the higher-density composition of Mercury, and the half-water compositions of Callisto, Ganymede, and Titan. The Moon, Io, and Mars are all close to the Earth-like curve but noticeably above it, indicating lower core mass fractions and/or cores that are enhanced in light elements, as is the case for Mars (see section 2.3.2).

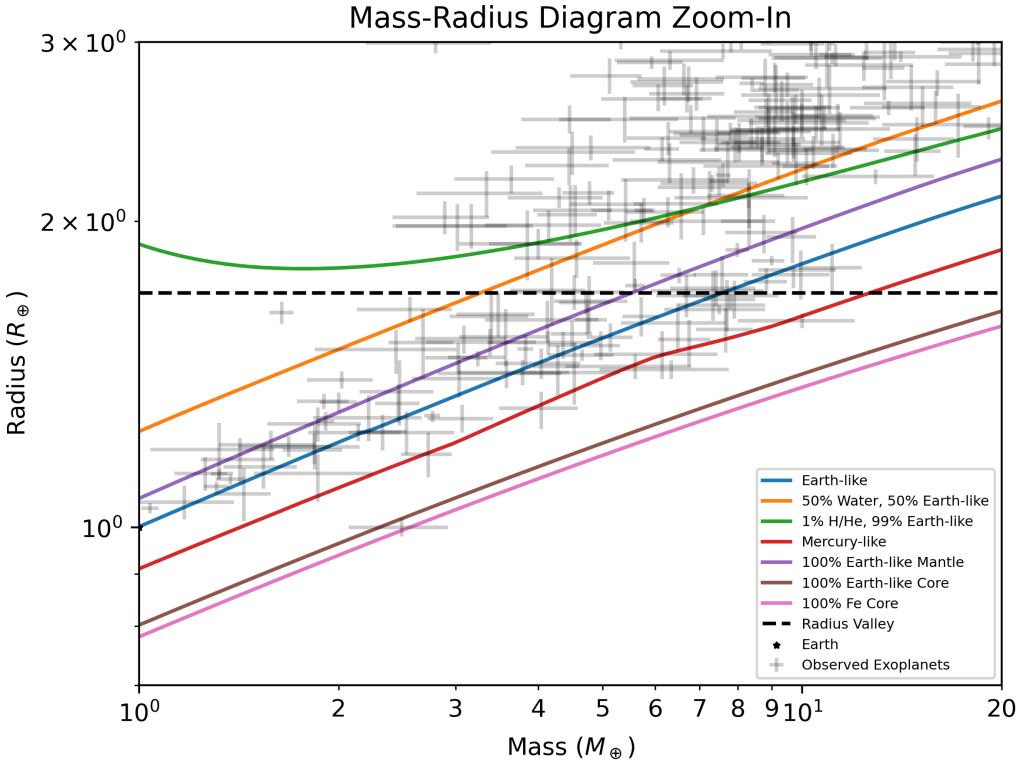

FIGURE 2.9: The same as Figure 2.8 but zoomed in on the parameter space of super-Earths and sub-Neptunes. The kink in the curve of the Mercury-like core is caused by a narrow region of parameter space in which the core becomes purely liquid. Mercury's core melting temperature in our model lies very close to the core temperature throughout its interior(see Appendix A5), allowing small changes in planetary structure to have noticable effects on M-R diagrams as shown here.

In Figure 2.9, we zoom into masses between 1 and 20 $M_\oplus$, the super-Earth to sub-Neptune regime. The radius valley, located at $\sim$1.7 $R_\oplus$ (with variance with instellation and stellar type), is indicated with a horizontal dashed line (e.g. Fulton et al.; 2017; Fulton and Petigura; 2018; Cloutier and Menou; 2020). At masses less than $\sim 8M_\oplus$, a radius of $1.7R_\oplus$ (the nominal center of the radius valley) is greater than that of a planet with an Earth-like composition, indicating either a core mass fraction much lower than Earth's or some amount of H/He (<%) or H_2O (up to 50%). At these same lower masses, lying above the radius valley requires a more significant amount of H/He (>%) or an extended steam atmosphere. Below the intersection of the half-water, half-Earth-like curve with the radius valley at $\sim 3.7M_\oplus$, all but two planets with reliable mass and radius measurements have compositions between purely a pure iron core and a water world, indicating a relative lack of volatile-enriched planets.

Mass and radius are not the only available parameters, as most exoplanets have known $T_{\rm eq}$ as well. In Figure 2.10, we plot mass-radius curves for varying equilibrium temperatures and compare to the exoplanet population at those temperatures. From this view, we see that planets with a H/He envelope have radii more sensitive to heat than water-rich planets, so the mass at which a water world and H/He-enriched planet have the same radius increases with increasing equilibrium temperature.

2.4.2 Power-Law Fits to the M-R Relation

We present $M = aR^b$ curves for fits to the condensed worlds in our dataset derived via `scipy.optimize.curve_fit` in Table 2.6. We model these curves as piecewise functions with breaks at the masses at which new phases appear or disappear from the planetary interior. These fits are only for intermediate masses, as high- and low-pressure physics at high and low masses cause deviations from a power-law curve (see Figure 2.11 and discussion below). We found that a low-mass limit of $0.89M_\oplus$–the mass at which post-perovskite appears in an Earth-like composition–and a high-mass limit of $8.21M_\oplus$ following Zeng et al. (2016)[15] was appropriate. The gaps in the fit for Mercury-like planets are due to two mass regimes in which one transition happens and then another transition happens at the immediately next most massive planet, leaving inadequate data to fit a curve. In these cases, we exclude the lower mass of the two model planets from all fits.

Inspection of Table 2.6 reveals that the power-law exponent generally increases with increasing planetary mass and increasing planetary bulk density, both of which cause

[15]Rounded up from $8M_\oplus$ to include a model planet at the mass of $8.21M_\oplus$.

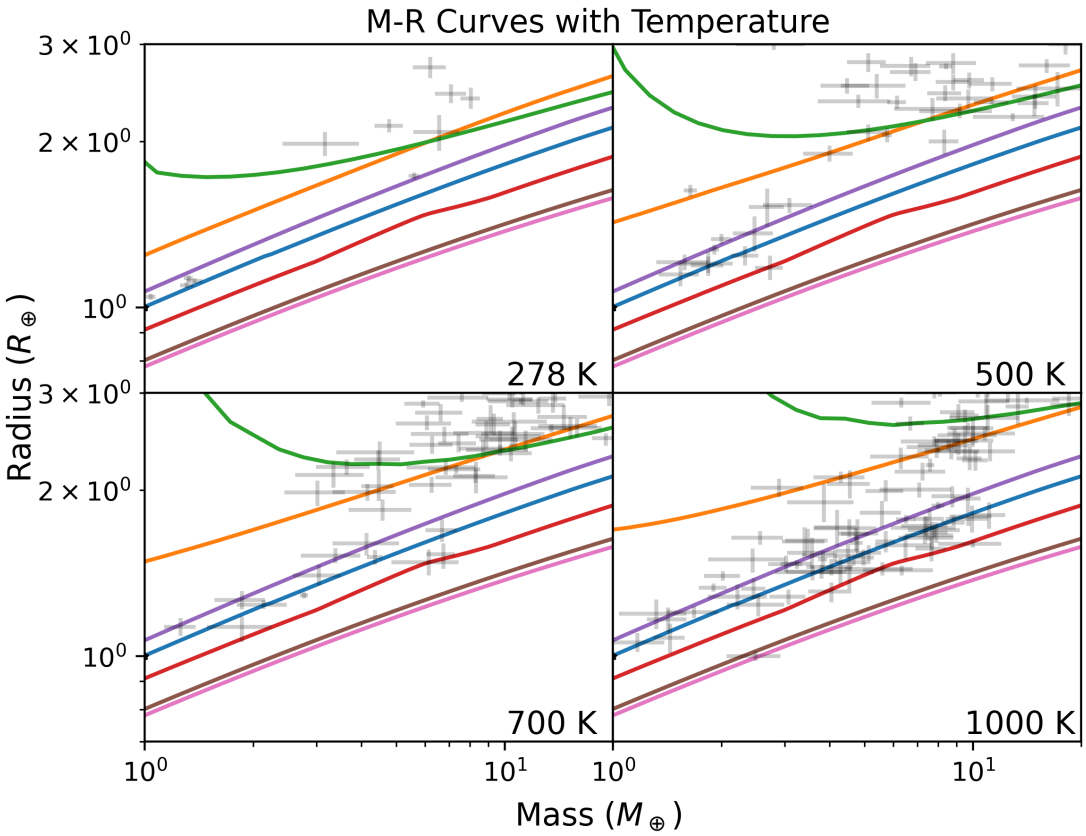

FIGURE 2.10: The same as Figure 2.9 but with planetary equilibrium temperatures (as defined for $A_B = 0$, note that our planets have an assumed $A_B = 0.3$, so the actual outer layer temperature is approximately $(1 - 0.3)^{0.25}$ times the listed temperature) varied. Curve colours are the same as Figure 2.8. background exoplanet populations are the planets with equilibrium temperatures reported by the exoplanet archive to be closest to the temperature of the models in a panel. Note that the exoplanet does not have homogeneously-assumed albdeos, so this comparison is instructive only. The noticeable kink at $\sim 4 M_\oplus$ at 1000 K for a H/He-enveloped planet corresponds to the majority of the mantle becoming liquid.

greater compression within the interior. Notably, the power laws of water worlds and Earth-like planets are within a few % at masses where both are expected to have the same state of core; similarly, the power laws of Earth-like and Iron cores are within 1% of each other. Our pure core worlds are always fully solid as the mantle material melting point at zero pressure is much lower than the core material melting point at zero pressure, explaining the lack of kinks in their M-R relationship. The slightly higher compression

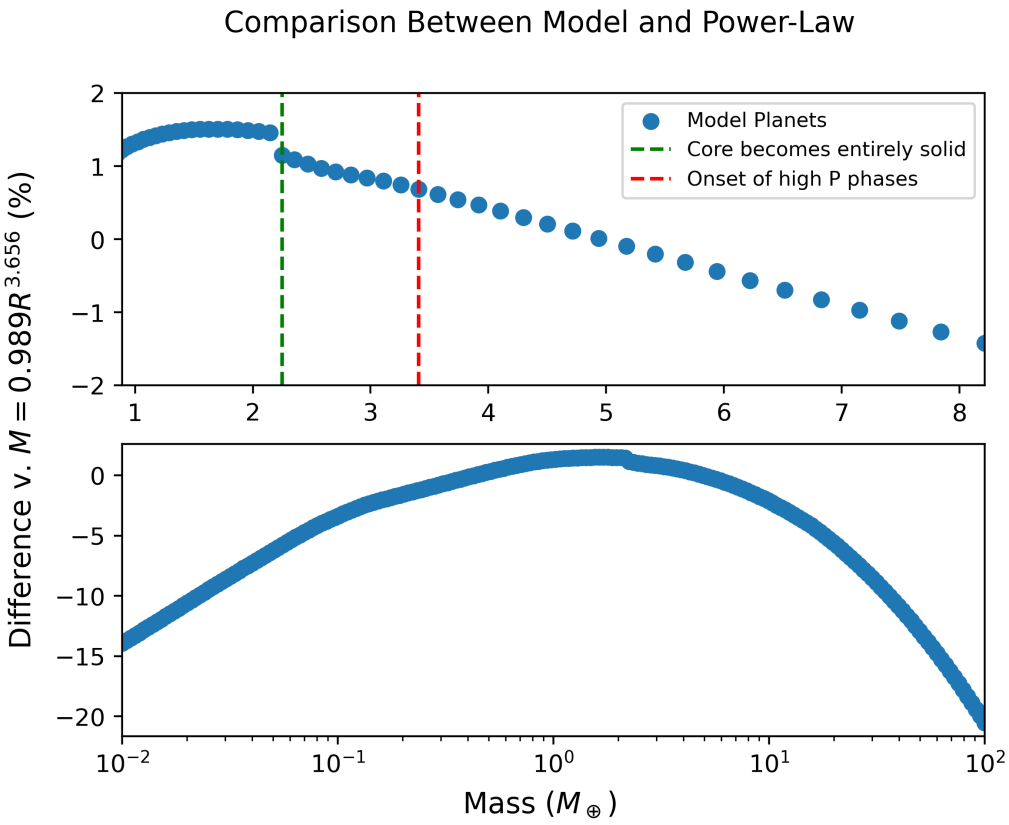

FIGURE 2.11: The relative difference between our calculated planetary radii for an Earth-like composition and the $M = 0.989R^{3.656}$ power law that best-fits it for masses between 0.89 and 2.25 Earth masses (see Table 2.6). Two kinks corresponding to changes in the planetary interior structure are labeled with vertical lines. (Top) Masses between 1 and 8.21 $M_\oplus$ on a linear scale. (Bottom) Masses between 0.01 and 100 $M_\oplus$ on a log scale.

of a pure Fe core causes its curve to increasingly separate from the Earth-like core at higher masses (see Figure 2.8).

In Figure 2.11, we compare the model radii of Earth-like planets with the power-law fit for masses between 0.89 and 2.25 $M_\oplus$ from Table 2.6. We observe that the inaccuracy of the radii of the power-law fit reaches tens of % at the lowest and highest masses. We also observe that jumps or kinks appear in the mass-radius curve at the locations at which the state of the interior changes, indicating that the power law is no longer appropriate, justifying our prescription of changing power laws at these masses. This indicates that it is not possible to capture planetary mass-radii relations with a simple

power law, however the inaccuracy from doing so is $\lesssim 2\%$ for planets in the 0.89-8.21 $M_\oplus$ range, which may be acceptable in many circumstances but in other circumstances is comparable to the level of observational uncertainty.

TABLE 2.6: Power-Law fit to the isocomposition curves of every consolidated composition considered in our sample.

Mass Range ($M_\oplus$)	Change to the interior at minimum of mass range	Best-Fit Equation
	Water World	
0.89-1.18	-	$M = 0.457R^{3.599}$
1.18-1.29	Post-Perovskite appears	$M = 0.445R^{3.698}$
1.29-1.63	Ice X appears	$M = 0.436R^{3.773}$
1.63-3.26	Core becomes purely solid	$M = 0.424R^{3.846}$
3.26-8	High Pressure Mantle Phases	$M = 0.395R^{3.973}$
	Earth-Like Mantle	
0.89-2.47	-	$M = 0.787R^{3.576}$
2.47-8	Post-perovskite appears	$M = 0.7R^{3.903}$
	Earth-Like	
0.89-2.25	Post-perovskite appears	$M = 0.989R^{3.656}$
2.25-3.41	Core becomes purely solid	$M = 0.967R^{3.803}$
3.41-8	High Pressure Mantle Phases	$M = 0.887R^{4.037}$
	Mercury-Like	
0.89-1.78	-	$M = 1.419R^{3.763}$
1.78-5.67	Post-Perovskite Appears	$M = 1.465R^{3.64}$
5.94-6.83	Solid Inner Core Re-Appears	$M = 0.641R^{5.796}$
7.15-8	Dissociated Mantle & Core becomes purely solid	$M = 0.625R^{5.872}$
	Earth-Like Core	
0.89-8	-	$M = 2.299R^{4.127}$
	Pure Iron Core	
0.89-8	-	$M = 2.569R^{4.157}$

2.5 Discussion

2.5.1 Comparison to Empirical Fits

Our M-R power laws can be compared against terrestrial planet empirical M-R relationships. Our low-mass power law is consistent with the empirical power laws from Chen and Kipping (2017)–whose fit is dominated by solar system objects–and Müller et al. (2024)–whose fit includes no solar system objects (although our fit is slightly higher than that reported by Otegi et al. (2020)), indicating that up to $\sim 2\ M_\oplus$, planets behave much like Earth and Venus. Beyond this mass, our R exponent increases beyond the empirical mass-radius relation. However, the empirical mass-radius relation beyond 2 $M_\oplus$ in Chen and Kipping (2017) and 4.4 $M_\oplus$ in Müller et al. (2024) becomes contaminated with volatile-enriched worlds, so a statement on whether this divergence truly represents a diverging behavior of rocky worlds is difficult to assess. Nonetheless, a search for a kink in the empirical exoplanet mass-radius relation at $\sim 3.4\ M_\oplus$ could be a powerful observational test for high pressure phase transitions in the mantle.

There is, however, reason for our mass-radius relations to diverge from the empirical relations for super-Earths for reasons unrelated to the phase changes considered here: hot

super-Earths may sequester a significant portion of their primordial H/He atmospheres, resulting in a higher density deficit in the core and thus mass increasing less strongly with radius than it otherwise would (Schlichting and Young; 2022).

2.5.2 Comparison to the Literature

Having presented our model, validated it, and presented its results, it is worthwhile to consider the alternatives in the literature and evaluate the relative strengths of different models.

The largest difference in radii between our model and those in the literature is between our pure-core planets (both with elements following Earth's and a pure Iron composition) and those of Zeng et al. (2016), which have radii several % larger than ours, as is visible in Figure 2.12. We note that there are no planets that fall below the radius of a pure Fe object in our model–although four are consistent with one–unlike the curves of Zeng et al. (2016), indicating that our model is the more physical one. This is because Zeng et al. (2016) use a poorly extrapolating BM2 EOS (Eq. 2.4 with $K_0' = 0$) for the core material. Zeng et al. (2016) justify the usage of this EOS by its good extrapolation to ultrahigh pressures ($\sim$ 12 TPa), but these pressures are only achieved at $\sim$ 100 $M_\oplus$, a mass beyond the parameter space of interest for Fe-rich planets. Additionally, Zeng et al. (2016) extrapolate using the liquid outer core of the Earth and thus underestimate densities for more massive planets due to neglecting the phase transition to solid and the decreased presence of light elements in the solid. The curves of Zeng et al. (2016, 2019) are thus not appropriate for application to objects with high core mass fractions, overestimating their radii by several %.

The BICEPS model of Haldemann et al. (2024) is the most similar work in the literature to this one, including mantle gibbs free energy minimization, a correction for transit radii, an irradiated atmospheric temperature profile using the same prescriptions as here, and using approximately half of the same EOS used here. Our model uniquely includes more transitions in the high-pressure mantle, preferential partitioning of light elements into the liquid core, and rotation while BICEPS uniquely includes H_2O-H/He mixing (among many other smaller differences). These effects are small ($\sim$ 0.5%) for our validation sample and thus it is likely that the BICEPS model would reproduce the radii that we validate on to within 1%. These effects are not necessarily small in parts of parameter space not probed in the solar system. Haldemann et al. (2024) likely slightly overestimate super-Earth radii by not including the high-pressure phase

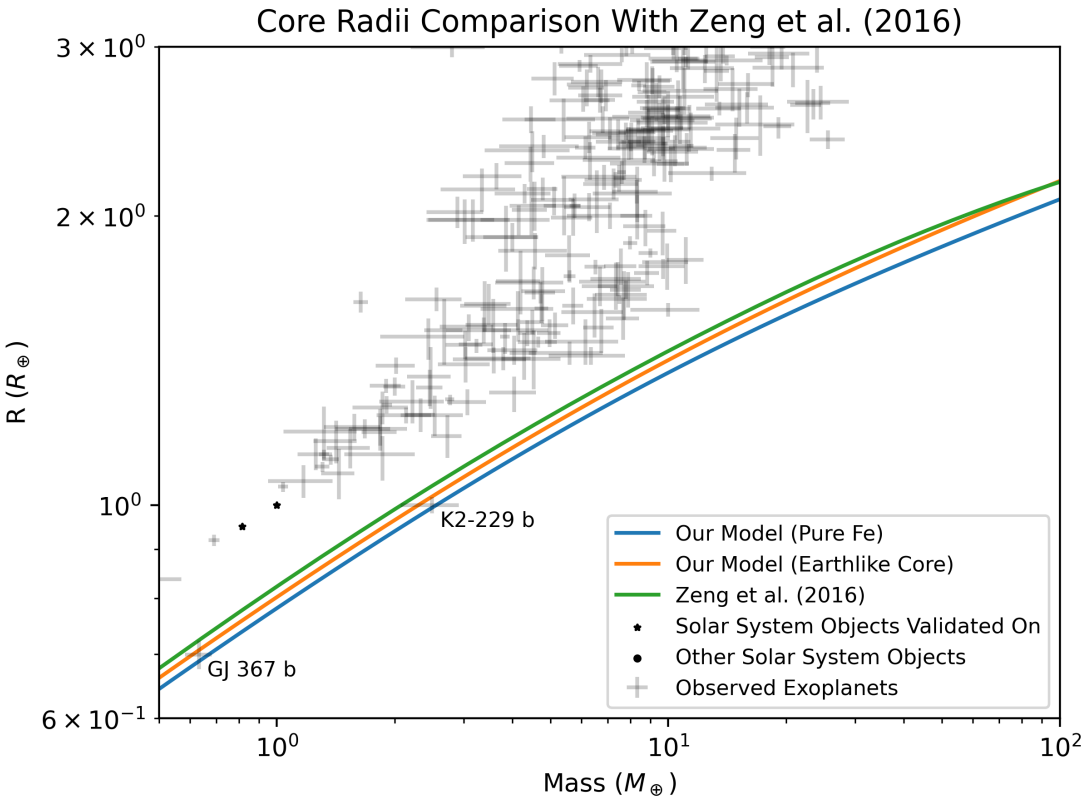

FIGURE 2.12: The mass-radius relations for planets with a 100% core mass fraction in our model, both composed of pure Fe and an Earth-like chemical inventory, compared to the findings of Zeng et al. (2016).

transitions considered here, while this work would moderately underestimate planetary radii for planets with significant H_2O and H/He, if the two are indeed miscible.

The other modern model that includes Gibbs free energy minimization of the mantle using HeFESTo is ExoPlex (Unterborn, Desch, Hinkel and Lorenzo; 2018; Unterborn, Hinkel and Desch; 2018; Unterborn and Panero; 2019; Schulze et al.; 2021; Unterborn et al.; 2023). ExoPlex assumes a fully liquid core and thus systematically underestimates planetary densities (overestimates planetary raii) for planets with solid cores, especially above the mass at which planetary cores may be entirely solid ($\gtrsim 2.24 M_\oplus$ in this model). ExoPLEX does not currently include Ice X and thus is not appropriate for use on planets with very high water contents, however this issue has already been identified and will be remedied in future ExoPLEX releases (Unterborn et al.; 2023). Unlike our model and BICEPS (Haldemann et al.; 2024), ExoPLEX does include Al and Ca in the planetary mantle and thus is the planetary interior structure model that currently models Earth-like mantles most accurately. This is reflected in ExoPLEX's 0.1% (-0.22% in an earlier version (Unterborn, Desch, Hinkel and Lorenzo; 2018)) error on their model Earth radii, only slightly larger than that found by our model(Unterborn et al.; 2023).

The model of Dorn et al. (2015, 2017) includes Gibbs free energy minimization of the mantle with Al and Ca as well. It also solves for an atmosphere in chemical equilibrium of H, He, C, and O Dorn et al. (2015, 2017), giving it the most expansive non-core chemical inventory in the literature we have reviewed. However, it does not include light elements in the core, melting, or the newer EOS released since its publication (Dorn et al.; 2015, 2017).

ExoPie does not include Gibbs free energy minimization in the mantle but does include the EOS for olivine, wadsleysite, ringwoodite, perovskite, and post-perovskite, as well as the ability to put Fe in the mantle (Plotnykov and Valencia; 2020, 2024; Valencia et al.; 2006, 2007). ExoPie does include Ni in the core and uses Si instead of S as the dominant light element–which likely reflects reality, see section 2.3.1 (Plotnykov and Valencia; 2020). ExoPie's model Earth radius has an error of ∼-0.44% (from their Fig. 2).

The model of Brugger et al. (2016, 2017); Acuña et al. (2021) also does not include Gibbs free energy minimization, instead including olivine, enstatite, perovskite, and the ability to put Fe in the mantle. This is a slightly more limited inventory than the other mantle models, but the effect of the transition zone (in Earth, the mantle at depths between 420 and 650 km, see Figure 2.4) is relatively minor. More significantly, the

exclusion of post-perovskite leads to a systematic (if minor, post-perovskite is only ∼1.5% denser than perovskite in mantle conditions) underestimation of planetary densities (and thus overestimation of their radii). Acuña et al. (2021) do not include a H/He envelope but do include a coupled atmospheric model for which radiative transfer profiles are computed that includes CO_2, a potential advance upon our model for planets with secondary atmospheres (Marcq; 2012; Marcq et al.; 2017). Brugger et al. (2017)'s model Earth has a radius error of -0.8%.

The MAGRATHEA model of Huang et al. (2022); Rice et al. (2025) also does not include Gibbs free energy minimization, instead including olivine, enstatite, perovskite, and a silicate melt. Crucially, MAGRATHEA does not include Fe in the mantle, although Rice et al. (2025) does discuss a basic prescription to account for this by modifying the $MgSiO_3$ EOS that is not in the default model. MAGRATHEA also does not include light elements in the core by default, although Rice et al. (2025) discuss the addition of a light element in the core. Huang et al. (2022)'s model Earth has a radius of $0.967R_\oplus$ by default and 0.9884 $R_\oplus$ if temperature jumps are included.

Aguichine et al. (2021) also does not include Gibbs free energy minimization, but include an upper mantle made of olivine and enstatite and a lower mantle made of $MgSiO_3$ and MgO. Aguichine et al. (2021) also include S in the planetary core but assume a purely solid core. Aguichine et al. (2021)'s mode Earth has a radius of 0.992 $R_\oplus$. Unlike this model, Aguichine et al. (2021, 2025) is part of a planetary evolutionary model and thus explicitly accounts for the thermal history of a planet. It thus may be more appropriate for young planets than our model as it treats their thermal structures self-consistently (Aguichine et al.; 2021, 2025).

Lopez and Fortney (2014) also present a planetary evolution model, albeit focused on H/He-enveloped worlds rather than the water worlds of Aguichine et al. (2021). Lopez and Fortney (2014) use the older H/He EOS of Saumon et al. (1995) that do not include the more recently published impact of non-ideal mixing between H and He of Chabrier and Debras (2021), resulting in systematically lower densities and thus larger radii. Lopez and Fortney (2014) also approximate planetary cores with EOS for olivine and iron. The simplified nature of the prescription for the core and mantle makes the model unfit for application to Earth-like planets.

The model of van den Berg et al. (2019) neglects low-pressure phases in the mantle but does include the high-pressure phase transitions of Umemoto et al. (2017) as in our model. van den Berg et al. (2019) do not include Fe in the mantle or light elements in

the core. These simplifications are reflected in van den Berg et al. (2019)'s −1.30% error model Earth radius, although we do note that van den Berg et al. (2019) is the only other publication to include Umemoto et al. (2017)'s high-pressure mantle phase transitions and thus is not subject to the systematic overprediction of super-Earth radii elsewhere in the literature. van den Berg et al. (2019) also numerically model convection, allowing a more realistic interior temperature evolution than modeled here.

Boujibar et al. (2020) do not include Fe in the mantle, but do include a mantle presciption composed of peridotite, perovskite, post-perovskite, and the fictitious phases post-post-perovskite 1 and 2, which have EOS calculated assuming that the EOS jumps between peroskite and post-perovskite and replicated once and twice, respectively. Boujibar et al. (2020) do not include Fe in the mantle or light elements in the core but do allow for both a solid and liquid core.

The APPLE model of Sur et al. (2024) is built for application to giant planets and thus has an extremely simplified rock prescription assuming pure post-perovskite. APPLE includes semi-convection, helium rain, and metallicity gradients in envelopes (Sur et al.; 2024). APPLE is thus appropriate for application to planets either above our 100 $M_{\oplus}$ cutoff or that are majority H/He such as Saturn (Sur et al.; 2024; Tejada Arevalo et al.; 2024; Sur et al.; 2025).

Finally, we return to the interior structure model with the widest use in the community, that of Zeng et al. (2019, 2016); Zeng and Sasselov (2013). It is constructed by extrapolating the density profiles of Earth to pressure regimes beyond the Earth and thus is not a model based on mineral physics, making a direct comparison difficult as a model Earth's radius has no error by construction Zeng et al. (2016). This does have the effect of avoiding the systematic mantle density underprediction (radius overprediction) from excluding Fe in the mantle. As planets around different stars (and even different planets around our own sun) have different compositions, such an extrapolation is not strictly valid. Additionally, as composition besides the core, mantle, and water mass fractions is not input into the model, it cannot be used to make any inferences about those parameters.

In sum, our model recovers the Earth's radius more accurately than any other model in the literature because it includes more core and mantle phases and more up-to-date EOS than any other model in the literature (to the author's knowledge). The other models that include Gibbs free energy minimization and light elements in the core,

BICEPS and ExoPlex, have comparable model Earth radii but do not include high-pressure mantle EOS and thus grow less reliable with increasing planet mass (Haldemann et al.; 2024; Unterborn et al.; 2023). The most commonly used model in the literature, (Zeng et al.; 2019), is inappropriate for planets with large cores, significantly non-Earth-like chemical compositions, or with large enough masses that an extrapolation from Earth's conditions is inappropriate.

2.5.3 Water Outside the Water Layer

2.5.3.1 Water in the interior

Our model does not include volatile sequestration within planetary interiors, which can significantly reduce the radii of planets ($3 - 25\%$) (Shah et al.; 2021; Dorn and Lichtenberg; 2021; Luo et al.; 2024). This effect is particularly pronounced for planets with magma oceans, into which water partitions much more readily than solids (Dorn and Lichtenberg; 2021; Elkins-Tanton; 2008). The details of where water can be partitioned relies on the pressures and thus depths at which water equilibrated with the surrounding material, requiring a planetary evolutionary model rather than a static model as presented here (Luo et al.; 2024). A particular process of interest is chemical equilibration with the atmosphere, which can destroy the vast majority (up to $\sim 95\%$) of accreted water (Werlen et al.; 2025). The interplay of these processes as well as atmospheric escape is necessary to fully capture the distribution of water within the planet population.

Our model serves as a useful endmember that includes no water sequestration. If sequestration induces a systematic reduction of planetary radii, it would appear as a discrepancy between our model's predicted radius of the planet and its actual radius, with our radius being larger than the planet's true radius. Thus, if we obtained independent observational constraints on the free parameters of Table 2.1–such as by assuming that planets inherit elemental abundance ratios from their stars to set mantle abundance ratios–and inferred a planet's core mass fraction using our model, it would be lower than reality. This discrepancy could be used for evidence of water sequestration, as has been done (using a different interior structure model) in D. Weisserman et al. (2025, in prep.).

2.5.3.2 Water in the H/He envelope

Our model also does not account for the miscibility of H/He and water resulting in a mixed H/He-water layer, as is included in the models of Haldemann et al. (2024). Burn et al. (2024) find that this effect is crucial in replicating the radius valley with their model of planet formation. Limited experimental studies have been conducted to

determine H/He and water's miscibility, and only at pressures up to a few GPa. At very low (< 0.2 GPa) pressures, Seward and Franck (1981) find H/He and water completely immiscible. At $\sim$ GPa pressures, Bali et al. (2013); Vlasov et al. (2023) find that H/He and water are miscible within silicate material at temperatures above ~ 900 K, with the temperature at which miscibility is possible moving to higher temperatures with higher pressures, implying high-pressure immiscibility of H/He and water, although such an extrapolation cannot continue indefinitely (Bergermann et al.; 2024).

Given the uncertainty of extrapolations from and lack of direct high-pressure probing by experimentation, the high-pressure miscibility of H/He and water is determined by simulation. Soubiran and Militzer (2015) find H/He and water are always miscible between 2 and 70 GPa and 1000 and 6000 K, while Bergermann et al. (2024) use a similar methodology but include nuclear quantum effects and find that at pressures above 10 GPa, H/He and water become immiscible for $T < 2000$ K (Bethkenhagen et al.; 2013). Some reasonable planet parameters within our model (e.g 1% H/He 99% Earth-like, $10 M_{\oplus}$, surface T of 300 K) have temperature profiles lying on the immiscible side of this line while others (e.g 1% H/He 99% Earth-like, $10 M_{\oplus}$, surface T of 1000 K) have temperature profiles that cross into the miscible region.

Given the current disagreement in the literature, the sparse sampling in P-T space of miscibility studies, and the complex consequences of the process of demixing, we do not include any H/He mixing with water and thus our model can be taken as a no H/He-water mixing endmember. If H/He-water mixing is indeed significant, our model underestimates radii by placing water at systematically higher pressures than it would be in if it was mixed (Burn et al.; 2024).

2.6 Conclusion

2.6.1 Summary

We have constructed a new interior structure model that covers the entire parameter space of exoplanets besides gas giants. This interior structure model improves upon the literature by incorporating the following physics simultaneously:

- A Gibbs free energy minimization equilibrium mineralogy inside the upper mantle
- High-pressure phases of mantle material
- Low-pressure phases of iron

- Light elements in the liquid and solid core and partitioning between the two
- Temperature jumps at the top and bottom of the mantle
- A prescription to calculate transit radii instead of radii at a set pressure surface
- An upper atmospheric temperature profile from radiative transfer equations
- Thermal terms in all EOS
- H/He non-ideal mixing
- EOS for Iron that extrapolates well to high pressures
- Rotation

We validate this model by creating forward models for solar system objects using parameters derived from constraints independent of interior structure models (where possible) in the literature. Our validation sample consists of Earth, Mars, and the Moon– the only three planetary bodies in the universe that humans have installed seismometers on–as well as Venus, Mercury, and Europa. For the first half of the validation sample, we find radii and moment of inertia coefficients within 0.5% or 1σ of reality; for the second half of the validation sample, we find radii and moment of inertia coefficients within 1% or 3σ of reality. We encourage authors of interior structure model publications targeting Earth-like planets to include their model Earth's $r - \rho$ profile, radius and moment of inertia to allow assessment of its accuracy.

We generate mass-radius curves H/He-enveloped, water world , pure mantle , Earth-like, Mercury-like, Earth-like core, and pure iron core compositions at equilibrium temperatures between Earth's and 1000 K. We fit new $M = aR^b$ relations to these curves as piecewise functions, breaking each piece at the masses wherein the planetary properties change, inducing kinks in the mass-radius curve. For an Earth-like composition, these breaks occur at 2.24 $M_\oplus$ and 3.41 $M_\oplus$, related to the solidification of the core and the appearance of high pressure phases in the mantle, respectively. We find that planets of all compositions get denser with mass than can be described by a simple power law, meaning that the power law for each progressively more massive piece is larger. We find that planetary cores have higher scaling coefficients than Earth-like or water world planets, while Earth-like and water world planets have coefficients that agree when their core states are the same.

We find that the iron-rich EOS of Zeng et al. (2016) extrapolate poorly to the planetary core pressure regime, leading to systematic overestimates of planetary radii for a pure iron core.

Our mass-radius relations are available at `https://github.com/Bennett-Skinner/SkinnerPudritzCloutier2025-MR-curves/`.

2.6.2 Future Work

The forward model presented here will be the foundation for a code to retrieve planetary compositions from measured masses and radii in a forthcoming publication. The use of this model to recalculate radii from the planet population synthesis model of Alessi et al. (2017); Alessi and Pudritz (2018); Alessi et al. (2020); Alessi and Pudritz (2022) is also forthcoming. Future improvements to the model will include an expansion of the chemical inventory in the planetary mantle and core, including the sequestration of water within the planetary interior (Haldemann et al.; 2024). Finally, future versions of this model will move beyond the simple melting curve of Eq. 2.22 and incorporate the experimentally-derived melting temperatures of mixtures.

REP and RC are supported by the Natural Sciences and Engineering Council of Canada (NSERC) through the Discovery Grants program. BNS thanks the following for scientific discussions on interior structure models and physics impacting them: Artyom Aguichine, Komal Bali, Caroline Dorn, Jonas Haldemann, Laura Schaefer, Ankan Sur, and Emerson Tao. Exoplanet Archive (DOI: 10.26133/NEA12) (Christiansen et al.; 2025) `NumPy` (Harris et al.; 2020), `pandas` (pandas development team; 2025), `Matplotlib` (Hunter; 2007), `SciPy` (Virtanen et al.; 2020)

Bibliography

Acuña, L., Deleuil, M., Mousis, O., Marcq, E., Levesque, M. and Aguichine, A. (2021). Characterisation of the hydrospheres of TRAPPIST-1 planets, **647**: A53.

Adams, E. R., Jackson, B., Johnson, S., Ciardi, D. R., Cochran, W. D., Endl, M., Everett, M. E., Furlan, E., Howell, S. B., Jayanthi, P., MacQueen, P. J., Matson, R. A., Partyka-Worley, C., Schlieder, J., Scott, N. J., Stanton, S. M. and Ziegler, C. (2021). Ultra-short-period Planets in K2. III. Neighbors are Common with 13 New Multiplanet Systems and 10 Newly Validated Planets in Campaigns 0-8 and 10, **2**(4): 152.

Aguichine, A., Batalha, N., Fortney, J. J., Nettelmann, N., Owen, J. E. and Kempton, E. M. R. (2025). Evolution of Steam Worlds: Energetic Aspects, **988**(2): 186.

Aguichine, A., Mousis, O., Deleuil, M. and Marcq, E. (2021). Mass-Radius Relationships for Irradiated Ocean Planets, **914**(2): 84.

Ahrens, T. J. (1979). Equations of state of iron sulfide and constraints on the sulfur content of the earth, **84**: 985–998.

Alessi, M., Inglis, J. and Pudritz, R. E. (2020). Formation of planetary populations - III. Core composition and atmospheric evaporation, **497**(4): 4814–4833.

Alessi, M. and Pudritz, R. E. (2018). Formation of planetary populations - I. Metallicity and envelope opacity effects, **478**(2): 2599–2617.

Alessi, M. and Pudritz, R. E. (2022). Combined effects of disc winds and turbulence-driven accretion on planet populations, **515**(2): 2548–2577.

Alessi, M., Pudritz, R. E. and Cridland, A. J. (2017). On the formation and chemical composition of super Earths, **464**(1): 428–452.

Alfè, D., Gillan, M. J. and Price, G. D. (2002). Composition and temperature of the Earth's core constrained by combining ab initio calculations and seismic data, *Earth and Planetary Science Letters* **195**(1-2): 91–98.

Alfè, D., Gillan, M. J. and Price, G. D. (2007). Temperature and composition of the Earth's core, *Contemporary Physics* **48**(2): 63–80.

Al'Tshuler, L., Kormer, S., Bakanova, A. and Trunin, R. (1960). Equation of state for aluminum, copper, and lead in the high pressure region, *Sov. Phys. JETP* **11**(3): 573–579.

Al'tshuler, L. V., Brusnikin, S. E. and Kuz'menkov, E. A. (1987). Isotherms and Grüneisen functions for 25 metals, *Journal of Applied Mechanics and Technical Physics* **28**(1): 129–141.

Anderson, D. L. (2005). *New Theory of the Earth*.

Anderson, J. D., Schubert, G., Jacobson, R. A., Lau, E. L., Moore, W. B. and Sjogren, W. L. (1998). Europa's Differentiated Internal Structure: Inferences from Four Galileo Encounters, *Science* **281**: 2019.

Anderson, O. L. (1979). Evidence supporting the approximation $\gamma\rho$ = const for the Grüneisen parameter of the Earth's lower mantle, **84**(B7): 3537–3542.

Anderson, W. W. (2019). An analytic expression approximating the Debye heat capacity function, *AIP Advances* **9**(7): 075108.

Andrault, D., Bolfan-Casanova, N., Nigro, G. L., Bouhifd, M. A., Garbarino, G. and Mezouar, M. (2011). Solidus and liquidus profiles of chondritic mantle: Implication for melting of the Earth across its history, *Earth and Planetary Science Letters* **304**(1-2): 251–259.

Badro, J. (2014). Spin Transitions in Mantle Minerals, *Annual Review of Earth and Planetary Sciences* **42**(1): 231–248.

Bali, E., Audétat, A. and Keppler, H. (2013). Water and hydrogen are immiscible in earth's mantle, *Nature* **495**(7440): 220–222.

Banerdt, W. B., Smrekar, S. E., Banfield, D., Giardini, D., Golombek, M., Johnson, C. L., Lognonné, P., Spiga, A., Spohn, T., Perrin, C., Stähler, S. C., Antonangeli, D., Asmar, S., Beghein, C., Bowles, N., Bozdag, E., Chi, P., Christensen, U., Clinton, J., Collins, G. S., Daubar, I., Dehant, V., Drilleau, M., Fillingim, M., Folkner, W., Garcia, R. F., Garvin, J., Grant, J., Grott, M., Grygorczuk, J., Hudson, T., Irving, J. C. E., Kargl, G., Kawamura, T., Kedar, S., King, S., Knapmeyer-Endrun, B., Knapmeyer, M., Lemmon, M., Lorenz, R., Maki, J. N., Margerin, L., McLennan, S. M., Michaut, C., Mimoun, D., Mittelholz, A., Mocquet, A., Morgan, P., Mueller, N. T., Murdoch, N., Nagihara, S., Newman, C., Nimmo, F., Panning, M., Pike, W. T., Plesa, A.-C., Rodriguez, S., Rodriguez-Manfredi, J. A., Russell, C. T., Schmerr, N., Siegler, M., Stanley, S., Stutzmann, E., Teanby, N., Tromp, J., van Driel, M., Warner, N., Weber, R. and Wieczorek, M. (2020). Initial results from the InSight mission on Mars, *Nature Geoscience* **13**(3): 183–189.

Bedell, M., Bean, J. L., Meléndez, J., Spina, L., Ramírez, I., Asplund, M., Alves-Brito, A., dos Santos, L., Dreizler, S., Yong, D., Monroe, T. and Casagrande, L. (2018). The Chemical Homogeneity of Sun-like Stars in the Solar Neighborhood, **865**(1): 68.

Belonoshko, A. B., Dorogokupets, P. I., Johansson, B., Saxena, S. K. and Koči, L. (2008). Ab initio equation of state for the body-centered-cubic phase of iron at high pressure and temperature, **78**(10): 104107.

Belonoshko, A. B., Skorodumova, N. V., Rosengren, A., Ahuja, R., Johansson, B., Burakovsky, L. and Preston, D. L. (2005). High-Pressure Melting of $MgSiO_3$, **94**(19): 195701.

Benkhoff, J., Murakami, G., Baumjohann, W., Besse, S., Bunce, E., Casale, M., Cremonese, G., Glassmeier, K. H., Hayakawa, H., Heyner, D., Hiesinger, H., Huovelin, J., Hussmann, H., Iafolla, V., Iess, L., Kasaba, Y., Kobayashi, M., Milillo, A., Mitrofanov, I. G., Montagnon, E., Novara, M., Orsini, S., Quemerais, E., Reininghaus, U., Saito, Y., Santoli, F., Stramaccioni, D., Sutherland, O., Thomas, N., Yoshikawa, I. and Zender, J. (2021). BepiColombo - Mission Overview and Science Goals, **217**(8): 90.

Bergermann, A., French, M. and Redmer, R. (2024). Ab initio calculation of the miscibility diagram for mixtures of hydrogen and water, **109**(17): 174107.

Bergin, E. A., Kempton, E. M. R., Hirschmann, M., Bastelberger, S. T., Teal, D. J., Blake, G. A., Ciesla, F. J. and Li, J. (2023). Exoplanet Volatile Carbon Content as a Natural Pathway for Haze Formation, **949**(1): L17.

Bethkenhagen, M., French, M. and Redmer, R. (2013). Equation of state and phase diagram of ammonia at high pressures from ab initio simulations, **138**(23): 234504–234504.

Birch, F. (1947). Finite Elastic Strain of Cubic Crystals, *Physical Review* **71**(11): 809–824.

Birch, F. (1952). Elasticity and Constitution of the Earth's Interior, **57**(2): 227–286.

Birch, F. (1964). Density and Composition of Mantle and Core, **69**(20): 4377–4388.

Bitsch, B., Izidoro, A., Johansen, A., Raymond, S. N., Morbidelli, A., Lambrechts, M. and Jacobson, S. A. (2019). Formation of planetary systems by pebble accretion and migration: growth of gas giants, **623**: A88.

Bitsch, B., Morbidelli, A., Johansen, A., Lega, E., Lambrechts, M. and Crida, A. (2018). Pebble-isolation mass: Scaling law and implications for the formation of super-Earths and gas giants, **612**: A30.

Boehler, R. and Ramakrishnan, J. (1980). Experimental results on the pressure dependence of the Grüneisen parameter: A review, **85**(B12): 6996–7002.

Botelho, R. B., Milone, A. d. C., Meléndez, J., Bedell, M., Spina, L., Asplund, M., dos Santos, L., Bean, J. L., Ramírez, I., Yong, D., Dreizler, S., Alves-Brito, A. and Yana

Galarza, J. (2019). Thorium in solar twins: implications for habitability in rocky planets, **482**(2): 1690–1700.

Bouchet, J., Mazevet, S., Morard, G., Guyot, F. and Musella, R. (2013). Ab initio equation of state of iron up to 1500 GPa, **87**(9): 094102.

Boujibar, A., Driscoll, P. and Fei, Y. (2020). Super-Earth Internal Structures and Initial Thermal States, *Journal of Geophysical Research (Planets)* **125**(5): e06124.

Bradley, P. A., Loomis, E. N., Merritt, E. C., Guzik, J. A., Denne, P. H. and Clark, T. T. (2018). Experimental validation of thermodynamic mixture rules at extreme pressures and densities, *Physics of Plasmas* **25**(1): 012710.

Briaud, A., Ganino, C., Fienga, A., Mémin, A. and Rambaux, N. (2023). The lunar solid inner core and the mantle overturn, **617**(7962): 743–746.

Brown, J. M. (2018). Local basis function representations of thermodynamic surfaces: Water at high pressure and temperature as an example, *Fluid Phase Equilibria* **463**: 18–31.

Brugger, B., Mousis, O., Deleuil, M. and Deschamps, F. (2017). Constraints on Super-Earth Interiors from Stellar Abundances, **850**(1): 93.

Brugger, B., Mousis, O., Deleuil, M. and Lunine, J. I. (2016). Possible Internal Structures and Compositions of Proxima Centauri b, **831**(2): L16.

Burn, R., Mordasini, C., Mishra, L., Haldemann, J., Venturini, J., Emsenhuber, A. and Henning, T. (2024). A radius valley between migrated steam worlds and evaporated rocky cores, *Nature Astronomy* **8**: 463–471.

Byrne, P. K., Klimczak, C., Celâl Şengör, A. M., Solomon, S. C., Watters, T. R. and Hauck, II, S. A. (2014). Mercury's global contraction much greater than earlier estimates, *Nature Geoscience* **7**(4): 301–307.

Cascioli, G., Hensley, S., De Marchi, F., Breuer, D., Durante, D., Racioppa, P., Iess, L., Mazarico, E. and Smrekar, S. E. (2021). The Determination of the Rotational State and Interior Structure of Venus with VERITAS, **2**(6): 220.

Catalli, K., Shim, S.-H. and Prakapenka, V. (2009). Thickness and clapeyron slope of the post-perovskite boundary, *Nature* **462**(7274): 782–785.

Chabrier, G. and Debras, F. (2021). A New Equation of State for Dense Hydrogen-Helium Mixtures. II. Taking into Account Hydrogen-Helium Interactions, **917**(1): 4.

Chabrier, G., Mazevet, S. and Soubiran, F. (2019). A New Equation of State for Dense Hydrogen-Helium Mixtures, **872**(1): 51.

Chakrabarty, A. and Mulders, G. D. (2024). Where Are the Water Worlds? Identifying Exo-water-worlds Using Models of Planet Formation and Atmospheric Evolution, **966**(2): 185.

Chen, J. and Kipping, D. (2017). Probabilistic Forecasting of the Masses and Radii of Other Worlds, **834**(1): 17.

Christiansen, J. L., McElroy, D. L., Harbut, M., Ciardi, D. R., Crane, M., Good, J., Hardegree-Ullman, K. K., Kesseli, A. Y., Lund, M. B., Lynn, M., Muthiar, A., Nilsson, R., Oluyide, T., Papin, M., Rivera, A., Swain, M., Susemiehl, N. D., Tam, R., van Eyken, J. and Beichman, C. (2025). The NASA Exoplanet Archive and Exoplanet Follow-up Observing Program: Data, Tools, and Usage, **6**(8): 186.

Christiansen, J. L., Zink, J. K., Hardegree-Ullman, K. K., Fernandes, R. B., Hopkins, P. F., Rebull, L. M., Boley, K. M., Bergsten, G. J. and Bhure, S. (2023). Scaling K2. VII. Evidence For a High Occurrence Rate of Hot Sub-Neptunes at Intermediate Ages, **166**(6): 248.

Cloutier, R. and Menou, K. (2020). Evolution of the Radius Valley around Low-mass Stars from Kepler and K2, **159**(5): 211.

Cohen, R. E., Gülseren, O. and Hemley, R. J. (2000). Accuracy of equation-of-state formulations, *American Mineralogist* **85**(2): 338–344.

Connolly, J. A. (2017). A primer in gibbs energy minimization for geophysicists, *Petrology* **25**(5): 526–534.

Connolly, J. A. D. (2009). The geodynamic equation of state: What and how, *Geochemistry, Geophysics, Geosystems* **10**(10): Q10014.

Cormier, V. F., Lithgow-Bertelloni, C., Stixrude, L. and Zheng, Y. (2023). Mantle Phase Changes Detected From Stochastic Tomography, *Journal of Geophysical Research (Solid Earth)* **128**(2): e2022JB025035.

Cormier, V., Tian, Y. and Zheng, Y. (2020). Heterogeneity spectrum of earth's upper mantle obtained from the coherence of teleseismic p waves, *Communications in Computational Physics* **28**(1): 74–97.

Cottenier, S., Probert, M. I. J., Van Hoolst, T., Van Speybroeck, V. and Waroquier, M. (2011). Crystal structure prediction for iron as inner core material in heavy terrestrial planets, *Earth and Planetary Science Letters* **312**(1): 237–242.

Cox, R. and Bauer, A. W. (2015). Impact breaching of Europa's ice: Constraints from numerical modeling, *Journal of Geophysical Research (Planets)* **120**(10): 1708–1719.

Dai, F., Masuda, K., Winn, J. N. and Zeng, L. (2019). Homogeneous Analysis of Hot Earths: Masses, Sizes, and Compositions, **883**(1): 79.

Debye, P. (1912). Zur Theorie der spezifischen Wärmen, *Annalen der Physik* **344**(14): 789–839.

Dewaele, A., Loubeyre, P., Occelli, F., Mezouar, M., Dorogokupets, P. I. and Torrent, M. (2006). Quasihydrostatic Equation of State of Iron above 2Mbar, **97**(21): 215504.

Dong, J., Fischer, R. A., Stixrude, L. P., Brennan, M. C., Daviau, K., Suer, T.-A., Turner, K. M., Meng, Y. and Prakapenka, V. B. (2025). Nonlinearity of the post-spinel transition and its expression in slabs and plumes worldwide, *Nature Communications* **16**(1): 1039.

Dong, J., Mardaru, G.-D., Asimow, P. D., Stixrude, L. P. and Fischer, R. A. (2025). Structure and Melting of Fe, MgO, SiO_2, and $MgSiO_3$ in Planets: Database, Inversion, and Phase Diagram, **6**(4): 103.

Dorn, C., Harrison, J. H. D., Bonsor, A. and Hands, T. O. (2019). A new class of Super-Earths formed from high-temperature condensates: HD219134 b, 55 Cnc e, WASP-47 e, **484**(1): 712–727.

Dorn, C., Khan, A., Heng, K., Connolly, J. A. D., Alibert, Y., Benz, W. and Tackley, P. (2015). Can we constrain the interior structure of rocky exoplanets from mass and radius measurements?, **577**: A83.

Dorn, C. and Lichtenberg, T. (2021). Hidden Water in Magma Ocean Exoplanets, **922**(1): L4.

Dorn, C., Venturini, J., Khan, A., Heng, K., Alibert, Y., Helled, R., Rivoldini, A. and Benz, W. (2017). A generalized Bayesian inference method for constraining the interiors of super Earths and sub-Neptunes, **597**: A37.

Dorogokupets, P. I. (2010). P-V-T equations of state of MgO and thermodynamics, *Physics and Chemistry of Minerals* **37**(9): 677–684.

Dorogokupets, P. I. and Dewaele, A. (2007). Equations of state of MgO, Au, Pt, NaCl-B1, and NaCl-B2: Internally consistent high-temperature pressure scales, *High Pressure Research* **27**(4): 431–446.

Dorogokupets, P. I., Dymshits, A. M., Litasov, K. D. and Sokolova, T. S. (2017). Thermodynamics and Equations of State of Iron to 350 GPa and 6000 K, *Scientific Reports* **7**: 41863.

Doyle, A. E., Young, E. D., Klein, B., Zuckerman, B. and Schlichting, H. E. (2019). Oxygen fugacities of extrasolar rocks: Evidence for an Earth-like geochemistry of exoplanets, *Science* **366**(6463): 356–359.

Dressing, C. D., Charbonneau, D., Dumusque, X., Gettel, S., Pepe, F., Collier Cameron, A., Latham, D. W., Molinari, E., Udry, S., Affer, L., Bonomo, A. S., Buchhave, L. A., Cosentino, R., Figueira, P., Fiorenzano, A. F. M., Harutyunyan, A., Haywood, R. D., Johnson, J. A., Lopez-Morales, M., Lovis, C., Malavolta, L., Mayor, M., Micela, G., Motalebi, F., Nascimbeni, V., Phillips, D. F., Piotto, G., Pollacco, D., Queloz, D., Rice, K., Sasselov, D., Ségransan, D., Sozzetti, A., Szentgyorgyi, A. and Watson, C. (2015). The Mass of Kepler-93b and The Composition of Terrestrial Planets, **800**(2): 135.

Dutta, R., Tracy, S. J. and Cohen, R. E. (2023). High-pressure order-disorder transition in $Mg_2Si\ O_4$: Implications for super-Earth mineralogy, **107**(18): 184112.

Dutta, R., Tracy, S. J., Cohen, R. E., Miozzi, F., Luo, K., Yang, J., Burnley, P. C., Smith, D., Meng, Y., Chariton, S., Prakapenka, V. B. and Duffy, T. S. (2022). Ultrahigh-pressure disordered eight-coordinated phase of Mg_2GeO_4: Analogue for super-Earth mantles, *Proceedings of the National Academy of Science* **119**(8): e2114424119.

Dziewonski, A. M. and Anderson, D. L. (1981). Preliminary reference Earth model, *Physics of the Earth and Planetary Interiors* **25**(4): 297–356.

Edwards, B., Changeat, Q., Tsiaras, A., Yip, K. H., Al-Refaie, A. F., Anisman, L., Bieger, M. F., Gressier, A., Shibata, S., Skaf, N., Bouwman, J., Cho, J. Y. K., Ikoma, M., Venot, O., Waldmann, I., Lagage, P.-O. and Tinetti, G. (2023). Exploring the Ability of Hubble Space Telescope WFC3 G141 to Uncover Trends in Populations of Exoplanet Atmospheres through a Homogeneous Transmission Survey of 70 Gaseous Planets, **269**(1): 31.

Einstein, A. (1906). Die Plancksche Theorie der Strahlung und die Theorie der spezifischen Wärme, *Annalen der Physik* **327**(1): 180–190.

Elkins-Tanton, L. T. (2008). Linked magma ocean solidification and atmospheric growth for Earth and Mars, *Earth and Planetary Science Letters* **271**(1-4): 181–191.

Faik, S., Tauschwitz, A. and Iosilevskiy, I. (2018). The equation of state package FEOS for high energy density matter, *Computer Physics Communications* **227**: 117–125.

Fei, Y. and Mao, H.-K. (1994). In Situ Determination of the NiAs Phase of FeO at High Pressure and Temperature, *Science* **266**(5191): 1678–1680.

Fei, Y., Murphy, C., Shibazaki, Y., Shahar, A. and Huang, H. (2016). Thermal equation of state of hcp-iron: Constraint on the density deficit of Earth's solid inner core, **43**(13): 6837–6843.

Fei, Y., Seagle, C. T., Townsend, J. P., McCoy, C. A., Boujibar, A., Driscoll, P., Shulenburger, L. and Furnish, M. D. (2021). Melting and density of $MgSiO_3$ determined by shock compression of bridgmanite to 1254GPa, *Nature Communications* **12**: 876.

Feistel, R. and Wagner, W. (2006). A New Equation of State for H_2O Ice Ih, *Journal of Physical and Chemical Reference Data* **35**(2): 1021–1047.

Fermi, E. (1928). Eine statistische Methode zur Bestimmung einiger Eigenschaften des Atoms und ihre Anwendung auf die Theorie des periodischen Systems der Elemente, *Zeitschrift fur Physik* **48**(1-2): 73–79.

Fernandes, R. B., Bergsten, G. J., Mulders, G. D., Pascucci, I., Hardegree-Ullman, K. K., Giacalone, S., Christiansen, J. L., Rogers, J. G., Gupta, A., Dawson, R. I., Koskinen, T. T., Boley, K. M., Curtis, J. L., Cunha, K., Mamajek, E. E., Sagynbayeva, S., Bhure, S. S., Ciardi, D. R., Karpoor, P. R., Pearson, K. A., Zink, J. K. and Feiden, G. A. (2025). Signatures of Atmospheric Mass Loss and Planet Migration in the Time Evolution of Short-period Transiting Exoplanets, **169**(4): 208.

Fiquet, G., Auzende, A. L., Siebert, J., Corgne, A., Bureau, H., Ozawa, H. and Garbarino, G. (2010). Melting of Peridotite to 140 Gigapascals, *Science* **329**(5998): 1516.

Fischer, E. L. and Parman, S. W. (2025). The bulk composition and initial size of Mercury, **439**: 116664.

Fischer, R. A., Campbell, A. J., Shofner, G. A., Lord, O. T., Dera, P. and Prakapenka, V. B. (2011). Equation of state and phase diagram of FeO, *Earth and Planetary Science Letters* **304**(3-4): 496–502.

Fischer, R. A., Nakajima, Y., Campbell, A. J., Frost, D. J., Harries, D., Langenhorst, F., Miyajima, N., Pollok, K. and Rubie, D. C. (2015). High pressure metal-silicate partitioning of Ni, Co, V, Cr, Si, and O, **167**: 177–194.

Foley, B. J., Houser, C., Noack, L. and Tosi, N. (2020). The heat budget of rocky planets, *Planetary Diversity: Rocky planet processes and their observational signatures*, IOP Publishing Bristol, UK, pp. 4–1.

Fontaine, G., Graboske, Jr., H. C. and van Horn, H. M. (1977). Equations of State for Stellar Partial Ionization Zones, **35**: 293.

Fortney, J. J., Dawson, R. I. and Komacek, T. D. (2021). Hot Jupiters: Origins, Structure, Atmospheres, *Journal of Geophysical Research (Planets)* **126**(3): e06629.

Freedman, R. S., Lustig-Yaeger, J., Fortney, J. J., Lupu, R. E., Marley, M. S. and Lodders, K. (2014). Gaseous Mean Opacities for Giant Planet and Ultracool Dwarf Atmospheres over a Range of Metallicities and Temperatures, **214**(2): 25.

French, M. and Redmer, R. (2015). Construction of a thermodynamic potential for the water ices VII and X, **91**(1): 014308.

Fulton, B. J. and Petigura, E. A. (2018). The California-Kepler Survey. VII. Precise Planet Radii Leveraging Gaia DR2 Reveal the Stellar Mass Dependence of the Planet Radius Gap, **156**(6): 264.

Fulton, B. J., Petigura, E. A., Howard, A. W., Isaacson, H., Marcy, G. W., Cargile, P. A., Hebb, L., Weiss, L. M., Johnson, J. A., Morton, T. D., Sinukoff, E., Crossfield, I. J. M. and Hirsch, L. A. (2017). The California-Kepler Survey. III. A Gap in the Radius Distribution of Small Planets, **154**(3): 109.

Gaidos, E., Conrad, C. P., Manga, M. and Hernlund, J. (2010). Thermodynamic Limits on Magnetodynamos in Rocky Exoplanets, **718**(2): 596–609.

Ganguly, J. (2025). Thermodynamics of light elements stratification in the earth's outer core and implications, *Earth and Planetary Science Letters* **659**: 119333.

Garcia, R. F., Gagnepain-Beyneix, J., Chevrot, S. and Lognonné, P. (2011). Very preliminary reference Moon model, *Physics of the Earth and Planetary Interiors* **188**(1): 96–113.

Garcia, R. F., Khan, A., Drilleau, M., Margerin, L., Kawamura, T., Sun, D., Wieczorek, M. A., Rivoldini, A., Nunn, C., Weber, R. C., Marusiak, A. G., Lognonné, P., Nakamura, Y. and Zhu, P. (2019). Lunar Seismology: An Update on Interior Structure Models, **215**(8): 50.

Gendre, H., Badro, J., Wehr, N. and Borensztajn, S. (2022). Martian core composition from experimental high-pressure metal-silicate phase equilibria, *Geochemical Perspectives Letters* **21**: 42–46.

Genova, A., Goossens, S., Mazarico, E., Lemoine, F. G., Neumann, G. A., Kuang, W., Sabaka, T. J., Hauck, S. A., Smith, D. E., Solomon, S. C. and Zuber, M. T. (2019). Geodetic Evidence That Mercury Has A Solid Inner Core, **46**(7): 3625–3633.

Gilvarry, J. J. (1954a). Solution of the Temperature-Perturbed Thomas-Fermi Equation, *Physical Review* **96**(4): 944–948.

Gilvarry, J. J. (1954b). Thermodynamics of the Thomas-Fermi Atom at Low Temperature, *Physical Review* **96**(4): 934–943.

Gilvarry, J. J. (1956). Grüneisen's Law and the Fusion Curve at High Pressure, *Physical Review* **102**(2): 317–325.

Glasser, L. (2013). Ambient heat capacities and entropies of ionic solids: a unique view using the debye equation, *Inorganic Chemistry* **52**(11): 6590–6594.

Goffo, E., Gandolfi, D., Egger, J. A., Mustill, A. J., Albrecht, S. H., Hirano, T., Kochukhov, O., Astudillo-Defru, N., Barragan, O., Serrano, L. M., Hatzes, A. P., Alibert, Y., Guenther, E., Dai, F., Lam, K. W. F., Csizmadia, S., Smith, A. M. S., Fossati, L., Luque, R., Rodler, F., Winther, M. L., Rørsted, J. L., Alarcon, J., Bonfils, X., Cochran, W. D., Deeg, H. J., Jenkins, J. M., Korth, J., Livingston, J. H., Meech, A., Murgas, F., Orell-Miquel, J., Osborne, H. L. M., Palle, E., Persson, C. M., Redfield, S., Ricker, G. R., Seager, S., Vanderspek, R., Van Eylen, V. and Winn, J. N. (2023). Company for the Ultra-high Density, Ultra-short Period Sub-Earth GJ 367 b: Discovery of Two Additional Low-mass Planets at 11.5 and 34 Days, **955**(1): L3.

Gomez Casajus, L., Zannoni, M., Modenini, D., Tortora, P., Nimmo, F., Van Hoolst, T., Buccino, D. and Oudrhiri, K. (2021). Updated Europa gravity field and interior structure from a reanalysis of Galileo tracking data, **358**: 114187.

González-Cataldo, F., Davis, S. and Gutiérrez, G. (2016). Melting curve of SiO_2 at multimegabar pressures: implications for gas giants and super-Earths, *Scientific Reports* **6**: 26537.

González-Cataldo, F. and Militzer, B. (2023). Ab initio determination of iron melting at terapascal pressures and Super-Earths core crystallization, *Physical Review Research* **5**(3): 033194.

Goodstein, D. L. (1985). *States of matter*, Courier Corporation.

Gordon, S. and McBride, B. J. (1994). Computer program for calculation of complex chemical equilibrium compositions and applications. part 1: Analysis, *Technical report*, NASA Lewis Research Center.

Grande, Z. M., Huang, C., Smith, D., Smith, J. S., Boisvert, J. H., Tschauner, O., Steffen, J. H. and Salamat, A. (2019). Bond strengthening in dense H2O and implications to planetary composition, *arXiv e-prints* p. arXiv:1906.11990.

Greenberg, E., Nazarov, R., Landa, A., Ying, J., Hood, R. Q., Hen, B., Jeanloz, R., Prakapenka, V. B., Struzhkin, V. V., Rozenberg, G. K. and Leonov, I. V. (2023). Phase transitions and spin state of iron in FeO under the conditions of Earth's deep interior, **107**(24): L241103.

Grundy, W. M., Buratti, B. J., Cheng, A. F., Emery, J. P., Lunsford, A., McKinnon, W. B., Moore, J. M., Newman, S. F., Olkin, C. B., Reuter, D. C., Schenk, P. M., Spencer, J. R., Stern, S. A., Throop, H. B. and Weaver, H. A. (2007). New Horizons Mapping of Europa and Ganymede, *Science* **318**(5848): 234.

Grüneisen, E. (1912). Theorie des festen Zustandes einatomiger Elemente, *Annalen der Physik* **344**(12): 257–306.

Guignot, N., Andrault, D., Morard, G., Bolfan-Casanova, N. and Mezouar, M. (2007). Thermoelastic properties of post-perovskite phase MgSiO $_3$ determined experimentally at core-mantle boundary P- T conditions, *Earth and Planetary Science Letters* **256**(1-2): 162–168.

Guillot, T. (2010). On the radiative equilibrium of irradiated planetary atmospheres, **520**: A27.

Guillot, T., Fletcher, L. N., Helled, R., Ikoma, M., Line, M. R. and Paramentier, V. (2023). Giant Planets from the Inside-Out, *in* S. Inutsuka, Y. Aikawa, T. Muto, K. Tomida and M. Tamura (eds), *Protostars and Planets VII*, Vol. 534 of *Astronomical Society of the Pacific Conference Series*, p. 947.

Gupta, A. and Schlichting, H. E. (2019). Sculpting the valley in the radius distribution of small exoplanets as a by-product of planet formation: the core-powered mass-loss mechanism, **487**(1): 24–33.

Hakim, K., Rivoldini, A., Van Hoolst, T., Cottenier, S., Jaeken, J., Chust, T. and Steinle-Neumann, G. (2018). A new ab initio equation of state of hcp-Fe and its implication on the interior structure and mass-radius relations of rocky super-Earths, **313**: 61–78.

Haldemann, J., Alibert, Y., Mordasini, C. and Benz, W. (2020). AQUA: a collection of H_2O equations of state for planetary models, **643**: A105.

Haldemann, J., Dorn, C., Venturini, J., Alibert, Y. and Benz, W. (2024). BICEPS: An improved characterization model for low- and intermediate-mass exoplanets, **681**: A96.

Hama, J. and Suito, K. (1996). The search for a universal equation of state correct up to very high pressures, *Journal of Physics Condensed Matter* **8**(1): 67–81.

Hanel, R. A., Conrath, B. J., Kunde, V. G., Pearl, J. C. and Pirraglia, J. A. (1983). Albedo, internal heat flux, and energy balance of Saturn, **53**(2): 262–285.

Hanel, R., Conrath, B., Herath, L., Kunde, V. and Pirraglia, J. (1981). Albedo, internal heat, and energy balance of Jupiter: preliminary results of the voyager infrared investigation, **86**(A10): 8705–8712.

Harris, C. R., Millman, K. J., van der Walt, S. J., Gommers, R., Virtanen, P., Cournapeau, D., Wieser, E., Taylor, J., Berg, S., Smith, N. J., Kern, R., Picus, M., Hoyer, S., van Kerkwijk, M. H., Brett, M., Haldane, A., del Río, J. F., Wiebe, M., Peterson, P., Gérard-Marchant, P., Sheppard, K., Reddy, T., Weckesser, W., Abbasi, H., Gohlke, C. and Oliphant, T. E. (2020). Array programming with NumPy, *Nature* **585**(7825): 357–362.
URL: *https://doi.org/10.1038/s41586-020-2649-2*

Helffrich, G. (2000). Topography of the transition zone seismic discontinuities, *Reviews of Geophysics* **38**(1): 141–158.

Helled, R., Stevenson, D. J., Lunine, J. I., Bolton, S. J., Nettelmann, N., Atreya, S., Guillot, T., Militzer, B., Miguel, Y. and Hubbard, W. B. (2022). Revelations on Jupiter's formation, evolution and interior: Challenges from Juno results, **378**: 114937.

Heller, R. and Pudritz, R. (2015). Water Ice Lines and the Formation of Giant Moons around Super-Jovian Planets, **806**(2): 181.

Hemingway, D. J. and Driscoll, P. E. (2021). History and Future of the Martian Dynamo and Implications of a Hypothetical Solid Inner Core, *Journal of Geophysical Research (Planets)* **126**(4): e06663.

Hernlund, J. W. and Labrosse, S. (2007). Geophysically consistent values of the perovskite to post-perovskite transition Clapeyron slope, **34**(5): L05309.

Heuzé, O. (2012). General form of the Mie-Grüneisen equation of state, *Comptes Rendus Mecanique* **340**(10): 679–687.

Hinkel, N. R., Timmes, F. X., Young, P. A., Pagano, M. D. and Turnbull, M. C. (2014). Stellar Abundances in the Solar Neighborhood: The Hypatia Catalog, **148**(3): 54.

Hirose, K., Labrosse, S. and Hernlund, J. (2013). Composition and State of the Core, *Annual Review of Earth and Planetary Sciences* **41**: 657–691.

Hirose, K., Wood, B. and Vočadlo, L. (2021). Light elements in the earth's core, *Nature Reviews Earth & Environment* **2**(9): 645–658.

Hirschmann, M. M., Tenner, T., Aubaud, C. and Withers, A. C. (2009). Dehydration melting of nominally anhydrous mantle: The primacy of partitioning, *Physics of the Earth and Planetary Interiors* **176**(1-2): 54–68.

Holzapfel, W. B. (1996). Physics of solids under strong compression, *Reports on Progress in Physics* **59**(1): 29–90.

Holzapfel, W. B. (1998). Equations of state for solids under strong compression, *High Pressure Research* **16**(2): 81–126.

Holzapfel, W. B. (2002). Equations of State for Regular Solids, *High Pressure Research* **22**(1): 209–216.

Houser, C. (2007). Constraints on the presence or absence of post-perovskite in the lowermost mantle from long-period seismology, *Geophysical Monograph Series* **174**: 191–216.

Howard, L. N. (1966). Convection at high rayleigh number, *Applied Mechanics: Proceedings of the Eleventh International Congress of Applied Mechanics Munich (Germany) 1964*, Springer, pp. 1109–1115.

Howard, S. and Guillot, T. (2023). Accounting for non-ideal mixing effects in the hydrogen-helium equation of state, **672**: L1.

Hu, Q., Deng, J., Zhuang, Y., Yang, Z. and Huang, R. (2024). Earth's core-mantle boundary shaped by the crystallization of a hydrous terrestrial magma ocean, *National Science Review* **11**(7): nwae169.

Huang, C., Rice, D. R., Grande, Z. M., Smith, D., Smith, J. S., Boisvert, J. H., Tschauner, O., Salamat, A. and Steffen, J. H. (2021). Implications of an improved water equation of state for water-rich planets, **503**(2): 2825–2832.

Huang, C., Rice, D. R. and Steffen, J. H. (2022). MAGRATHEA: an open-source spherical symmetric planet interior structure code, **513**(4): 5256–5269.

Huang, D., Badro, J., Brodholt, J. and Li, Y. (2019). Ab Initio Molecular Dynamics Investigation of Molten Fe-Si-O in Earth's Core, **46**(12): 6397–6405.

Hunter, J. D. (2007). Matplotlib: A 2d graphics environment, *Computing in Science & Engineering* **9**(3): 90–95.

Ichikawa, H. and Tsuchiya, T. (2020). Ab Initio Thermoelasticity of Liquid Iron-Nickel-Light Element Alloys, *Minerals* **10**(1): 59.

Ichikawa, H., Tsuchiya, T. and Tange, Y. (2014). The P-V-T equation of state and thermodynamic properties of liquid iron, *Journal of Geophysical Research (Solid Earth)* **119**(1): 240–252.

Irwin, P. G. J., Wenkert, D. D., Simon, A. A., Dahl, E. and Hammel, H. B. (2025). The bolometric Bond albedo and energy balance of Uranus, **540**(2): 1719–1729.

Ita, J. and Stixrude, L. (1992). Petrology, elasticity, and composition of the mantle transition zone, **97**(B5): 6849–6866.

Izidoro, A., Schlichting, H. E., Isella, A., Dasgupta, R., Zimmermann, C. and Bitsch, B. (2022). The Exoplanet Radius Valley from Gas-driven Planet Migration and Breaking of Resonant Chains, **939**(2): L19.

Jeanloz, R. (1979). Properties of iron at high pressures and the state of the core, **84**(B11): 6059–6069.

Johansen, A., Ronnet, T., Schiller, M., Deng, Z. and Bizzarro, M. (2023). Anatomy of rocky planets formed by rapid pebble accretion. I. How icy pebbles determine the core fraction and FeO contents, **671**: A74.

John, J., Thamarai, V., Choudhary, T., Srinivasa, M. N., Jambhalikar, A., Giridhar, M. S., Mehra, M. M., Garg, M., Shila, K. V., Kummari, K., Karantha, S. P., Arvind, K. and Sriram, K. V. (2024). Identification and preliminary characterisation of signals recorded by instrument for lunar seismic activity at the Chandrayaan 3 landing site, **424**: 116285.

Journaux, B., Brown, J. M., Pakhomova, A., Collings, I. E., Petitgirard, S., Espinoza, P., Boffa Ballaran, T., Vance, S. D., Ott, J., Cova, F., Garbarino, G. and Hanfland, M. (2020). Holistic Approach for Studying Planetary Hydrospheres: Gibbs Representation of Ices Thermodynamics, Elasticity, and the Water Phase Diagram to 2,300 MPa, *Journal of Geophysical Research (Planets)* **125**(1): e06176.

Kamland Collaboration, Gando, A., Gando, Y., Ichimura, K., Ikeda, H., Inoue, K., Kibe, Y., Kishimoto, Y., Koga, M., Minekawa, Y., Mitsui, T., Morikawa, T., Nagai, N., Nakajima, K., Nakamura, K., Narita, K., Shimizu, I., Shimizu, Y., Shirai, J., Suekane, F., Suzuki, A., Takahashi, H., Takahashi, N., Takemoto, Y., Tamae, K., Watanabe, H., Xu, B. D., Yabumoto, H., Yoshida, H., Yoshida, S., Enomoto, S., Kozlov, A., Murayama, H., Grant, C., Keefer, G., Piepke, A., Banks, T. I., Bloxham, T., Detwiler, J. A., Freedman, S. J., Fujikawa, B. K., Han, K., Kadel, R., O'Donnell, T., Steiner, H. M., Dwyer, D. A., McKeown, R. D., Zhang, C., Berger, B. E., Lane, C. E., Maricic, J., Miletic, T., Batygov, M., Learned, J. G., Matsuno, S., Sakai, M., Horton-Smith, G. A., Downum, K. E., Gratta, G., Tolich, K., Efremenko, Y., Perevozchikov, O., Karwowski, H. J., Markoff, D. M., Tornow, W., Heeger, K. M. and Decowski, M. P. (2011). Partial radiogenic heat model for Earth revealed by geoneutrino measurements, *Nature Geoscience* **4**(9): 647–651.

Katsura, T. and Tange, Y. (2019). A Simple Derivation of the Birch-Murnaghan Equations of State (EOSs) and Comparison with EOSs Derived from Other Definitions of Finite Strain, *Minerals* **9**(12): 745.

Katz, R. F., Spiegelman, M. and Langmuir, C. H. (2003). A new parameterization of hydrous mantle melting, *Geochemistry, Geophysics, Geosystems* **4**(9): 1073.

Keane, A. (1954). An Investigation of Finite Strain in an Isotropic Material Subjected to Hydrostatic Pressure and its Seismological Applications, *Australian Journal of Physics* **7**: 322.

Kemp, M., Jenkins, J., Maclennan, J. and Cottaar, S. (2019). X-discontinuity and transition zone structure beneath Hawaii suggests a heterogeneous plume, *Earth and Planetary Science Letters* **527**: 115781.

Kennett, B. L. N., Engdahl, E. R. and Buland, R. (1995). Constraints on seismic velocities in the Earth from traveltimes, *Geophysical Journal International* **122**(1): 108–124.

Khan, A., Connolly, J. A. D., Pommier, A. and Noir, J. (2014). Geophysical evidence for melt in the deep lunar interior and implications for lunar evolution, *Journal of Geophysical Research (Planets)* **119**(10): 2197–2221.

Khan, A., Huang, D., Durán, C., Sossi, P. A., Giardini, D. and Murakami, M. (2023). Evidence for a liquid silicate layer atop the Martian core, **622**(7984): 718–723.

Khan, A., Sossi, P. A., Liebske, C., Rivoldini, A. and Giardini, D. (2022). Geophysical and cosmochemical evidence for a volatile-rich Mars, *Earth and Planetary Science Letters* **578**: 117330.

Knibbe, J. S., Rivoldini, A., Zhao, Y. and Van Hoolst, T. (2025). On the thermal evolution and magnetic field generation of planet Mercury, *Physics of the Earth and Planetary Interiors* **363**: 107348.

Konopliv, A. S., Park, R. S., Rivoldini, A., Baland, R.-M., Le Maistre, S., Van Hoolst, T., Yseboodt, M. and Dehant, V. (2020). Detection of the Chandler Wobble of Mars From Orbiting Spacecraft, **47**(21): e90568.

Koper, K. D. and Dombrovskaya, M. (2005). Seismic properties of the inner core boundary from PKiKP / P amplitude ratios, *Earth and Planetary Science Letters* **237**(3-4): 680–694.

Kreidberg, L., Bean, J. L., Désert, J.-M., Line, M. R., Fortney, J. J., Madhusudhan, N., Stevenson, K. B., Showman, A. P., Charbonneau, D., McCullough, P. R., Seager, S., Burrows, A., Henry, G. W., Williamson, M., Kataria, T. and Homeier, D. (2014). A Precise Water Abundance Measurement for the Hot Jupiter WASP-43b, **793**(2): L27.

Kuskov, O., Kronrod, E. and Kronrod, V. (2024). Chemical composition, mineralogy, and physical properties of the moon's mantle: A review, *Geochemistry International* **62**(12): 1227–1290.

Kuwayama, Y., Morard, G., Nakajima, Y., Hirose, K., Baron, A. Q. R., Kawaguchi, S. I., Tsuchiya, T., Ishikawa, D., Hirao, N. and Ohishi, Y. (2020). Equation of State of Liquid Iron under Extreme Conditions, **124**(16): 165701.

Labrosse, S., Hernlund, J. W. and Coltice, N. (2007). A crystallizing dense magma ocean at the base of the Earth's mantle, **450**(7171): 866–869.

Lambrechts, M. and Johansen, A. (2014). Forming the cores of giant planets from the radial pebble flux in protoplanetary discs, **572**: A107.

Lambrechts, M., Morbidelli, A., Jacobson, S. A., Johansen, A., Bitsch, B., Izidoro, A. and Raymond, S. N. (2019). Formation of planetary systems by pebble accretion and migration. How the radial pebble flux determines a terrestrial-planet or super-Earth growth mode, **627**: A83.

Latter, R. (1955). Temperature Behavior of the Thomas-Fermi Statistical Model for Atoms, *Physical Review* **99**(6): 1854–1870.

Le Maistre, S., Rivoldini, A., Caldiero, A., Yseboodt, M., Baland, R.-M., Beuthe, M., Van Hoolst, T., Dehant, V., Folkner, W. M., Buccino, D., Kahan, D., Marty, J.-C., Antonangeli, D., Badro, J., Drilleau, M., Konopliv, A., Péters, M.-J., Plesa, A.-C., Samuel, H., Tosi, N., Wieczorek, M., Lognonné, P., Panning, M., Smrekar, S. and Banerdt, W. B. (2023). Spin state and deep interior structure of Mars from InSight radio tracking, **619**(7971): 733–737.

Li, J., Bergin, E. A., Hirschmann, M. M., Blake, G. A., Ciesla, F. J. and Kempton, E. M. R. (2025). Soot Planets instead of Water Worlds, *arXiv e-prints* p. arXiv:2508.16781.

Li, L., Jiang, X., West, R. A., Gierasch, P. J., Perez-Hoyos, S., Sanchez-Lavega, A., Fletcher, L. N., Fortney, J. J., Knowles, B., Porco, C. C., Baines, K. H., Fry, P. M., Mallama, A., Achterberg, R. K., Simon, A. A., Nixon, C. A., Orton, G. S., Dyudina, U. A., Ewald, S. P. and Schmude, R. W. (2018). Less absorbed solar energy and more internal heat for Jupiter, *Nature Communications* **9**: 3709.

Li, L., Nixon, C. A., Achterberg, R. K., Smith, M. A., Gorius, N. J. P., Jiang, X., Conrath, B. J., Gierasch, P. J., Simon-Miller, A. A., Michael Flasar, F., Baines, K. H., Ingersoll, A. P., West, R. A., Vasavada, A. R. and Ewald, S. P. (2011). The global energy balance of Titan, **38**(23): L23201.

Lichtenberg, T., Schaefer, L. K., Nakajima, M. and Fischer, R. A. (2023). Geophysical Evolution During Rocky Planet Formation, *in* S. Inutsuka, Y. Aikawa, T. Muto, K. Tomida and M. Tamura (eds), *Protostars and Planets VII*, Vol. 534 of *Astronomical Society of the Pacific Conference Series*, p. 907.

Lin, Z. and Seager, S. (2025). Carbon-rich Sub-Neptune Interiors Are Compatible with JWST Observations, **990**(2): L35.

Linder, E. F., Mordasini, C., Mollière, P., Marleau, G.-D., Malik, M., Quanz, S. P. and Meyer, M. R. (2019). Evolutionary models of cold and low-mass planets: cooling curves, magnitudes, and detectability, **623**: A85.

Lopez, E. D. and Fortney, J. J. (2014). Understanding the Mass-Radius Relation for Sub-neptunes: Radius as a Proxy for Composition, **792**(1): 1.

Lopez, E. D. and Rice, K. (2018). How formation time-scales affect the period dependence of the transition between rocky super-Earths and gaseous sub-Neptunesand implications for $\eta_{\oplus}$, **479**(4): 5303–5311.

Luo, H., Dorn, C. and Deng, J. (2024). The interior as the dominant water reservoir in super-Earths and sub-Neptunes, *Nature Astronomy* **8**: 1399–1407.

Lyle, M. J., Pickard, C. J. and Needs, R. J. (2015). Prediction of 10-fold coordinated TiO_2 and SiO_2 structures at multimegabar pressures, *Proceedings of the National Academy of Science* **112**(22): 6898–6901.

Manglik, A., Wicht, J. and Christensen, U. R. (2010). A dynamo model with double diffusive convection for Mercury's core, *Earth and Planetary Science Letters* **289**(3-4): 619–628.

Mankovich, C. R. and Fuller, J. (2021). A diffuse core in Saturn revealed by ring seismology, *Nature Astronomy* **5**: 1103–1109.

Marcq, E. (2012). A simple 1-D radiative-convective atmospheric model designed for integration into coupled models of magma ocean planets, *Journal of Geophysical Research (Planets)* **117**(E1): E01001.

Marcq, E., Salvador, A., Massol, H. and Davaille, A. (2017). Thermal radiation of magma ocean planets using a 1-D radiative-convective model of H_2O-CO_2 atmospheres, *Journal of Geophysical Research (Planets)* **122**(7): 1539–1553.

Margot, J.-L., Campbell, D. B., Giorgini, J. D., Jao, J. S., Snedeker, L. G., Ghigo, F. D. and Bonsall, A. (2021). Spin state and moment of inertia of Venus, *Nature Astronomy* **5**: 676–683.

Margot, J.-L., Peale, S. J., Solomon, S. C., Hauck, II, S. A., Ghigo, F. D., Jurgens, R. F., Yseboodt, M., Giorgini, J. D., Padovan, S. and Campbell, D. B. (2012). Mercury's moment of inertia from spin and gravity data, *Journal of Geophysical Research (Planets)* **117**: E00L09.

Martinez, C. F., Cunha, K., Ghezzi, L. and Smith, V. V. (2019). A Spectroscopic Analysis of the California-Kepler Survey Sample. I. Stellar Parameters, Planetary Radii, and a Slope in the Radius Gap, **875**(1): 29.

Masters, G. and Gubbins, D. (2003). On the resolution of density within the Earth, *Physics of the Earth and Planetary Interiors* **140**(1-3): 159–167.

Matsumoto, K., Yamada, R., Kikuchi, F., Kamata, S., Ishihara, Y., Iwata, T., Hanada, H. and Sasaki, S. (2015). Internal structure of the Moon inferred from Apollo seismic data and selenodetic data from GRAIL and LLR, **42**(18): 7351–7358.

Mazevet, S., Licari, A., Chabrier, G. and Potekhin, A. Y. (2019). Ab initio based equation of state of dense water for planetary and exoplanetary modeling, **621**: A128.

McBride, B. J. and Gordon, S. (1996). Computer program for calculation of complex chemical equilibrium compositions and applications ii. users manual and program description: Users manual and program description-2, *Technical report*, NASA Lewis Research Center.

McDonough, W. (2014). 3.16–compositional model for the earth's core, *Treatise on geochemistry* **2**: 559–577.

McDonough, W. F. (2016). The composition of the lower mantle and core, *Deep earth: Physics and chemistry of the lower mantle and Core* pp. 143–159.

McDonough, W. F. and Sun, S. s. (1995). The composition of the Earth, *Chemical Geology* **120**(3-4): 223–253.

McQueen, R. G. and Marsh, S. P. (1966). Shock-wave compression of iron-nickel alloys and the Earth's core, **71**(6): 1751–1756.

Mie, G. (1903). Zur kinetischen Theorie der einatomigen Körper, *Annalen der Physik* **316**(8): 657–697.

Miller-Ricci, E., Seager, S. and Sasselov, D. (2009). The Atmospheric Signatures of Super-Earths: How to Distinguish Between Hydrogen-Rich and Hydrogen-Poor Atmospheres, **690**(2): 1056–1067.

Montagner, J. P. and Kennett, B. L. N. (1996). How to reconcile body-wave and normal-mode reference earth models, *Geophysical Journal International* **125**(1): 229–248.

Montagner, J.-P. and Roult, G. (2008). Normal modes of the Earth, *Journal of Physics Conference Series*, Vol. 118 of *Journal of Physics Conference Series*, p. 012004.

Morard, G., Antonangeli, D., Bouchet, J., Rivoldini, A., Boccato, S., Miozzi, F., Boulard, E., Bureau, H., Mezouar, M., Prescher, C., Chariton, S. and Greenberg, E. (2022). Structural and Electronic Transitions in Liquid FeO Under High Pressure, *Journal of Geophysical Research (Solid Earth)* **127**(11): e2022JB025117.

Mordasini, C. (2020). Planetary evolution with atmospheric photoevaporation. I. Analytical derivation and numerical study of the evaporation valley and transition from super-Earths to sub-Neptunes, **638**: A52.

Mordasini, C., Alibert, Y., Georgy, C., Dittkrist, K. M., Klahr, H. and Henning, T. (2012). Characterization of exoplanets from their formation. II. The planetary mass-radius relationship, **547**: A112.

Moulik, P. and Ekström, G. (2025a). Radial structure of the Earth: (I) Model concepts and data, *Physics of the Earth and Planetary Interiors* **361**: 107319.

Moulik, P. and Ekström, G. (2025b). Radial structure of the Earth: (II) Model features and interpretations, *Physics of the Earth and Planetary Interiors* **361**: 107320.

Müller, S., Baron, J., Helled, R., Bouchy, F. and Parc, L. (2024). The mass-radius relation of exoplanets revisited, **686**: A296.

Murnaghan, F. D. (1937). Finite deformations of an elastic solid, *American Journal of Mathematics* **59**(2): 235–260.

Murnaghan, F. D. (1944). The Compressibility of Media under Extreme Pressures, *Proceedings of the National Academy of Science* **30**(9): 244–247.

Musella, R., Mazevet, S. and Guyot, F. (2019). Physical properties of MgO at deep planetary conditions, **99**(6): 064110.

Nimmo, F. and Giese, B. (2005). Thermal and topographic tests of Europa chaos formation models from Galileo E15 observations, **177**(2): 327–340.

Niu, H., Oganov, A. R., Chen, X.-Q. and Li, D. (2015). Prediction of novel stable compounds in the Mg-Si-O system under exoplanet pressures, *Scientific Reports* **5**: 18347.

Nomura, R., Hirose, K., Uesugi, K., Ohishi, Y., Tsuchiyama, A., Miyake, A. and Ueno, Y. (2014). Low Core-Mantle Boundary Temperature Inferred from the Solidus of Pyrolite, *Science* **343**(6170): 522–525.

Nunn, C., Garcia, R. F., Nakamura, Y., Marusiak, A. G., Kawamura, T., Sun, D., Margerin, L., Weber, R., Drilleau, M., Wieczorek, M. A., Khan, A., Rivoldini, A., Lognonné, P. and Zhu, P. (2020). Lunar Seismology: A Data and Instrumentation Review, **216**(5): 89.

Oganov, A. (2015). Thermodynamics, phase transitions, equations of state, and elasticity of minerals at high pressures and temperatures, *Treatise on Geophysics: Second Edition* pp. 179–202.

Oganov, A. R. and Dorogokupets, P. I. (2004). Intrinsic anharmonicity in equations of state and thermodynamics of solids, *Journal of Physics Condensed Matter* **16**(8): 1351–1360.

Ohfuji, H., Sata, N., Kobayashi, H., Ohishi, Y., Hirose, K. and Irifune, T. (2007). A new high-pressure and high-temperature polymorph of FeS, *Physics and Chemistry of Minerals* **34**(5): 335–343.

Otegi, J. F., Bouchy, F. and Helled, R. (2020). Revisited mass-radius relations for exoplanets below 120 $M_{\oplus}$, **634**: A43.

Owen, J. E. and Schlichting, H. E. (2024). Mapping out the parameter space for photoevaporation and core-powered mass-loss, **528**(2): 1615–1629.

Owen, J. E. and Wu, Y. (2013). Kepler Planets: A Tale of Evaporation, **775**(2): 105.

Ozawa, H., Hirose, K., Tateno, S., Sata, N. and Ohishi, Y. (2010). Phase transition boundary between B1 and B8 structures of FeO up to 210 GPa, *Physics of the Earth and Planetary Interiors* **179**(3-4): 157–163.

Ozawa, H., Takahashi, F., Hirose, K., Ohishi, Y. and Hirao, N. (2011). Phase Transition of FeO and Stratification in Earth's Outer Core, *Science* **334**(6057): 792.

Palme, H. and O'Neill, H. (2014). Cosmochemical estimates of mantle composition. planets, asteriods, comets and the solar system, volume 2 of treatise on geochemistry . edited by andrew m. davis.

pandas development team, T. (2025). pandas-dev/pandas: Pandas.
URL: *https://doi.org/10.5281/zenodo.16918803*

Pappalardo, R. T., Buratti, B. J., Korth, H., Senske, D. A., Blaney, D. L., Blankenship, D. D., Burch, J. L., Christensen, P. R., Kempf, S., Kivelson, M. G., Mazarico, E., Retherford, K. D., Turtle, E. P., Westlake, J. H., Paczkowski, B. G., Ray, T. L.,

Kampmeier, J., Craft, K. L., Howell, S. M., Klima, R. L., Leonard, E. J., Matiella Novak, A., Phillips, C. B., Daubar, I. J., Blacksberg, J., Brooks, S. M., Choukroun, M. N., Cochrane, C. J., Diniega, S., Elder, C. M., Ernst, C. M., Gudipati, M. S., Luspay-Kuti, A., Piqueux, S., Rymer, A. M., Roberts, J. H., Steinbrügge, G., Cable, M. L., Scully, J. E. C., Castillo-Rogez, J. C., Hay, H. C. F. C., Persaud, D. M., Glein, C. R., McKinnon, W. B., Moore, J. M., Raymond, C. A., Schroeder, D. M., Vance, S. D., Wyrick, D. Y., Zolotov, M. Y., Hand, K. P., Nimmo, F., McGrath, M. A., Spencer, J. R., Lunine, J. I., Paty, C. S., Soderblom, J. M., Collins, G. C., Schmidt, B. E., Rathbun, J. A., Shock, E. L., Becker, T. C., Hayes, A. G., Prockter, L. M., Weiss, B. P., Hibbitts, C. A., Moussessian, A., Brockwell, T. G., Hsu, H.-W., Jia, X., Gladstone, G. R., McEwen, A. S., Patterson, G. W., McNutt, R. L., Evans, J. P., Larson, T. W., Cangahuala, L. A., Havens, G. G., Buffington, B. B., Bradley, B., Campagnola, S., Hardman, S. H., Srinivasan, J. M., Short, K. L., Jedrey, T. C., St. Vaughn, J. A., Clark, K. P., Vertesi, J. and Niebur, C. (2024). Science Overview of the Europa Clipper Mission, **220**(4): 40.

Parmentier, V. and Guillot, T. (2014). A non-grey analytical model for irradiated atmospheres. I. Derivation, **562**: A133.

Parmentier, V., Guillot, T., Fortney, J. J. and Marley, M. S. (2015). A non-grey analytical model for irradiated atmospheres. II. Analytical vs. numerical solutions, **574**: A35.

Paxton, B., Cantiello, M., Arras, P., Bildsten, L., Brown, E. F., Dotter, A., Mankovich, C., Montgomery, M. H., Stello, D., Timmes, F. X. and Townsend, R. (2013). Modules for Experiments in Stellar Astrophysics (MESA): Planets, Oscillations, Rotation, and Massive Stars, **208**(1): 4.

Paxton, B., Smolec, R., Schwab, J., Gautschy, A., Bildsten, L., Cantiello, M., Dotter, A., Farmer, R., Goldberg, J. A., Jermyn, A. S., Kanbur, S. M., Marchant, P., Thoul, A., Townsend, R. H. D., Wolf, W. M., Zhang, M. and Timmes, F. X. (2019). Modules for Experiments in Stellar Astrophysics (MESA): Pulsating Variable Stars, Rotation, Convective Boundaries, and Energy Conservation, **243**(1): 10.

Peale, S. J., Phillips, R. J., Solomon, S. C., Smith, D. E. and Zuber, M. T. (2002). A procedure for determining the nature of Mercury's core, **37**(9): 1269–1283.

Pearl, J. C. and Conrath, B. J. (1991). The albedo, effective temperature, and energy balance of Neptune, as determined from Voyager data, **96**: 18921–18930.

Petricca, F., Castillo-Rogez, J. C., Genova, A., Melwani Daswani, M., Styczinski, M. J., Cochrane, C. J. and Vance, S. D. (2025). Partial differentiation of Europa and implications for the origin of materials in the Jupiter system, *Nature Astronomy* **9**: 501–511.

Pickard, C. J. and Needs, R. J. (2009). FAST TRACK COMMUNICATION: Stable phases of iron at terapascal pressures, *Journal of Physics Condensed Matter* **21**(45): 452205.

Plotnykov, M. and Valencia, D. (2020). Chemical fingerprints of formation in rocky super-Earths' data, **499**(1): 932–947.

Plotnykov, M. and Valencia, D. (2024). Observation uncertainty effects on the precision of interior planetary parameters, **530**(3): 3488–3499.

Poirier, J.-P. (2000). *Introduction to the Physics of the Earth's Interior*, Cambridge University Press.

Pommier, A. (2025). Experimental Investigation of Mercury's Outer Core, **52**(16): e2025GL116595.

Press, W. H., Teukolsky, S. A., Vetterling, W. T. and Flannery, B. P. (1996). Numerical recipes in fortran 90: the art of parallel scientific computing.

Prialnik, D. (2009). *An Introduction to the Theory of Stellar Structure and Evolution*.

Revenaugh, J. and Jordan, T. H. (1991). Mantle layering from ScS reverberations: 3. The upper mantle, **96**(B12): 19,781–19,810.

Rice, D. R., Huang, C., Steffen, J. H. and Vazan, A. (2025). Uncertainties in the Inference of Internal Structure: The Case of TRAPPIST-1 f, **986**(1): 2.

Roberts, J. H., McKinnon, W. B., Elder, C. M., Tobie, G., Biersteker, J. B., Young, D., Park, R. S., Steinbrügge, G., Nimmo, F., Howell, S. M., Castillo-Rogez, J. C., Cable, M. L., Abrahams, J. N., Bland, M. T., Chivers, C., Cochrane, C. J., Dombard, A. J., Ernst, C., Genova, A., Gerekos, C., Glein, C., Harris, C. D., Hay, H. C. F. C., Hayne, P. O., Hedman, M., Hussmann, H., Jia, X., Khurana, K., Kiefer, W. S., Kirk, R., Kivelson, M., Lawrence, J., Leonard, E. J., Lunine, J. I., Mazarico, E., McCord, T. B., McEwen, A., Paty, C., Quick, L. C., Raymond, C. A., Retherford, K. D., Roth, L., Rymer, A., Saur, J., Scanlan, K., Schroeder, D. M., Senske, D. A., Shao, W., Soderlund, K., Spiers, E., Styczinski, M. J., Tortora, P., Vance, S. D., Villarreal, M. N., Weiss, B. P., Westlake, J. H., Withers, P., Wolfenbarger, N., Buratti, B., Korth,

H., Pappalardo, R. T. and The Interior Thematic Working Group (2023). Exploring the Interior of Europa with the Europa Clipper, **219**(6): 46.

Rogers, L. A. (2015). Most 1.6 Earth-radius Planets are Not Rocky, **801**(1): 41.

Rose, J. H., Smith, J. R. and Ferrante, J. (1983). Universal features of bonding in metals, **28**(4): 1835–1845.

Rosenblatt, P., Dumoulin, C., Marty, J.-C. and Genova, A. (2021). Determination of Venus' Interior Structure with EnVision, *Remote Sensing* **13**(9): 1624.

Rydberg, R. (1932). Graphische Darstellung einiger bandenspektroskopischer Ergebnisse, *Zeitschrift fur Physik* **73**(5-6): 376–385.

Sakai, F., Hirose, K. and Morard, G. (2023). Partitioning of silicon and sulfur between solid and liquid iron under core pressures: Constraints on Earth's core composition, *Earth and Planetary Science Letters* **624**: 118449.

Sakai, T., Dekura, H. and Hirao, N. (2016). Experimental and theoretical thermal equations of state of $MgSiO_3$ post-perovskite at multi-megabar pressures, *Scientific Reports* **6**: 22652.

Sánchez-Cano, B., Hadid, L. Z., Aizawa, S., Murakami, G., Bamba, Y., Chiba, S., Hara, T., Heyner, D., Ho, G., Iwai, K., Kilpua, E., Kinoshita, G., Lavraud, B., Miyoshi, Y., Pinto, M., Schmid, D., Shiota, D., Vainio, R., Andre, N., Aronica, A., Asmar, S., Auster, H.-U., Barabash, S., Barthe, A., Baumjohann, W., Benkhoff, J., Bentley, M., Bunce, E., Cappuccio, P., Delcourt, D., di Stefano, I., Doria, I., Dresing, N., Fedorov, A., Fischer, D., Fiethe, B., Fränz, M., Gieseler, J., Giner, F., Giono, G., Harada, Y., Hussmann, H., Iess, L., Imamura, T., Jeszenszky, H., Jones, G., Katra, B., Kazakov, A., Kozyrev, A., Laky, G., Lefevre, C., Lichtenegger, H., Lindsay, S., Lucente, M., Magnafico, C., Magnes, W., Martindale, A., Matsuoka, A., Milillo, A., Mitrofanov, I., Nishiyama, G., Oleynik, P., Orsini, S., Paik, M., Palmroos, C., Plainaki, C., Penou, E., Persson, M., Quarati, F., Quémerais, E., Richter, I., Robidel, R., Rojo, M., Saito, Y., Santoli, F., Stark, A., Stumpo, M., Tian, R., Varsani, A., Verdeil, C., Williamson, H., Witasse, O. and Yokota, S. (2025). BepiColombo cruise science: overview of the mission contribution to heliophysics, *Earth, Planets and Space* **77**(1): 114.

Sata, N., Hirose, K., Shen, G., Nakajima, Y., Ohishi, Y. and Hirao, N. (2010). Compression of FeSi, Fe_3C, $Fe_{0.95}O$, and FeS under the core pressures and implication for light element in the Earth's core, *Journal of Geophysical Research (Solid Earth)* **115**(B9): B09204.

Sata, N., Ohfuji, H., Hirose, K., Kobayashi, H., Ohishi, Y. and Hirao, N. (2008). New high-pressure B2 phase of FeS above 180 GPa, *American Mineralogist* **93**(2-3): 492–494.

Saumon, D., Chabrier, G. and van Horn, H. M. (1995). An Equation of State for Low-Mass Stars and Giant Planets, **99**: 713.

Schaefer, L., Jacobsen, S. B., Remo, J. L., Petaev, M. I. and Sasselov, D. D. (2017). Metal-silicate Partitioning and Its Role in Core Formation and Composition on Super-Earths, **835**(2): 234.

Schenk, P., Matsuyama, I. and Nimmo, F. (2008). True polar wander on Europa from global-scale small-circle depressions, **453**(7193): 368–371.

Schlichting, H. E. and Young, E. D. (2022). Chemical Equilibrium between Cores, Mantles, and Atmospheres of Super-Earths and Sub-Neptunes and Implications for Their Compositions, Interiors, and Evolution, **3**(5): 127.

Schulze, J. G., Wang, J., Johnson, J. A., Gaudi, B. S., Unterborn, C. T. and Panero, W. R. (2021). On the Probability That a Rocky Planet's Composition Reflects Its Host Star, **2**(3): 113.

Scora, J., Valencia, D., Morbidelli, A. and Jacobson, S. (2020). Chemical diversity of super-Earths as a consequence of formation, **493**(4): 4910–4924.

Scora, J., Valencia, D., Morbidelli, A. and Jacobson, S. (2022). Rocky Histories: The Effect of High Excitations on the Formation of Rocky Planets, **940**(2): 144.

Seager, S., Kuchner, M., Hier-Majumder, C. A. and Militzer, B. (2007). Mass-Radius Relationships for Solid Exoplanets, **669**(2): 1279–1297.

Seward, T. and Franck, E. (1981). The system hydrogen-water up to 440 c and 2500 bar pressure, *Berichte der Bunsengesellschaft für physikalische Chemie* **85**(1): 2–7.

Shah, O., Alibert, Y., Helled, R. and Mezger, K. (2021). Internal water storage capacity of terrestrial planets and the effect of hydration on the M-R relation, **646**: A162.

Shah, O., Helled, R., Alibert, Y. and Mezger, K. (2022). Possible Chemical Composition And Interior Structure Models Of Venus Inferred From Numerical Modelling, **926**(2): 217.

Shearer, P. M. (1996). Transition zone velocity gradients and the 520-km discontinuity, **101**(B2): 3053–3066.

Shibaike, Y., Ormel, C. W., Ida, S., Okuzumi, S. and Sasaki, T. (2019). The Galilean Satellites Formed Slowly from Pebbles, **885**(1): 79.

Shim, S.-H., Duffy, T. S. and Shen, G. (2001). The post-spinel transformation in Mg_2SiO_4 and its relation to the 660-km seismic discontinuity, **411**(6837): 571–574.

Sossi, P. A., Nakajima, M. and Khan, A. (2024). Composition, Structure and Origin of the Moon, *arXiv e-prints* p. arXiv:2408.16840.

Sotin, C., Grasset, O. and Mocquet, A. (2007). Mass radius curve for extrasolar Earth-like planets and ocean planets, **191**(1): 337–351.

Soubiran, F. and Militzer, B. (2015). Miscibility Calculations for Water and Hydrogen in Giant Planets, **806**(2): 228.

Srinu, U., Kumar, P., Haldar, C., Kumar, M. R., Srinagesh, D. and Illa, B. (2021). X-Discontinuity Beneath the Indian Shield—Evidence for Remnant Tethyan Oceanic Lithosphere in the Mantle, *Journal of Geophysical Research (Solid Earth)* **126**(8): e2021JB021890.

Stacey, F. D. and Davis, P. M. (2004). High pressure equations of state with applications to the lower mantle and core, *Physics of the Earth and Planetary Interiors* **142**(3-4): 137–184.

Stacey, F. D. and Davis, P. M. (2008). *Physics of the Earth*, Cambridge University Press.

Stacey, F. D. and Hodgkinson, J. H. (2019). Thermodynamics with the Grüneisen parameter: Fundamentals and applications to high pressure physics and geophysics, *Physics of the Earth and Planetary Interiors* **286**: 42–68.

Statella, T., Pina, P. and da Silva, E. A. (2015). Extensive computation of albedo contrast between martian dust devil tracks and their neighboring regions, **250**: 43–52.

Stephens, G. L., O'Brien, D., Webster, P. J., Pilewski, P., Kato, S. and Li, J.-l. (2015). The albedo of Earth, *Reviews of Geophysics* **53**(1): 141–163.

Stewart, S., Davies, E., Duncan, M., Lock, S., Root, S., Townsend, J., Kraus, R., Caracas, R. and Jacobsen, S. (2020). The shock physics of giant impacts: Key requirements for the equations of state, *American Institute of Physics Conference Series*, Vol. 2272 of *American Institute of Physics Conference Series*, p. 080003.

Stixrude, L. (2012). Structure of Iron to 1 Gbar and 40 000 K, **108**(5): 055505.

Stixrude, L. (2014). Melting in super-earths, *Philosophical Transactions of the Royal Society of London Series A* **372**(2014): 20130076–20130076.

Stixrude, L. and Lithgow-Bertelloni, C. (2005). Thermodynamics of mantle minerals - I. Physical properties, *Geophysical Journal International* **162**(2): 610–632.

Stixrude, L. and Lithgow-Bertelloni, C. (2011). Thermodynamics of mantle minerals - II. Phase equilibria, *Geophysical Journal International* **184**(3): 1180–1213.

Stixrude, L. and Lithgow-Bertelloni, C. (2024). Thermodynamics of mantle minerals - III: the role of iron, *Geophysical Journal International* **237**(3): 1699–1733.

Sur, A., Su, Y., Tejada Arevalo, R., Chen, Y.-X. and Burrows, A. (2024). APPLE: An Evolution Code for Modeling Giant Planets, **971**(1): 104.

Sur, A., Tejada Arevalo, R., Su, Y. and Burrows, A. (2025). Simultaneous Evolutionary Fits for Jupiter and Saturn Incorporating Fuzzy Cores, **980**(1): L5.

Swain, M. R., Hasegawa, Y., Thorngren, D. P. and Roudier, G. M. (2024). Planet Mass and Metallicity: The Exoplanets and Solar System Connection, **220**(6): 61.

Takahashi, F., Shimizu, H. and Tsunakawa, H. (2019). Mercury's anomalous magnetic field caused by a symmetry-breaking self-regulating dynamo, *Nature Communications* **10**: 208.

Tao, R. and Fei, Y. (2021). High-pressure experimental constraints of partitioning behavior of Si and S at the Mercury's inner core boundary, *Earth and Planetary Science Letters* **562**: 116849.

Taylor, S. R., Taylor, G. J. and Taylor, L. A. (2006). The Moon: A Taylor perspective, **70**(24): 5904–5918.

Tejada Arevalo, R., Su, Y., Sur, A. and Burrows, A. (2024). Equations of State, Thermodynamics, and Miscibility Curves for Jovian Planet and Giant Exoplanet Evolutionary Models, **274**(2): 34.

Thomas, L. H. (1927). The calculation of atomic fields, *Proceedings of the Cambridge Philosophical Society* **23**(5): 542.

Thorngren, D. P., Fortney, J. J., Murray-Clay, R. A. and Lopez, E. D. (2016). The Mass-Metallicity Relation for Giant Planets, **831**(1): 64.

Tian, D., Lv, M., Wei, S. S., Dorfman, S. M. and Shearer, P. M. (2020). Global variations of Earth's 520- and 560-km discontinuities, *Earth and Planetary Science Letters* **552**: 116600.

Tsuchiya, T. and Tsuchiya, J. (2011). Prediction of a hexagonal SiO_2 phase affecting stabilities of $MgSiO_3$ and $CaSiO_3$ at multimegabar pressures, *Proceedings of the National Academy of Science* **108**(4): 1252–1255.

Tsuchiya, T., Tsuchiya, J., Umemoto, K. and Wentzcovitch, R. M. (2004). Phase transition in MgSiO $_3$ perovskite in the earth's lower mantle, *Earth and Planetary Science Letters* **224**(3-4): 241–248.

Umemoto, K. and Hirose, K. (2020). Chemical compositions of the outer core examined by first principles calculations, *Earth and Planetary Science Letters* **531**: 116009.

Umemoto, K. and Wentzcovitch, R. M. (2011). Two-stage dissociation in MgSiO $_3$ post-perovskite, *Earth and Planetary Science Letters* **311**(3): 225–229.

Umemoto, K. and Wentzcovitch, R. M. (2019). Ab initio exploration of post-PPV transitions in low-pressure analogs of $MgSiO_3$, *Physical Review Materials* **3**(12): 123601.

Umemoto, K., Wentzcovitch, R. M. and Allen, P. B. (2006). Dissociation of $MgSiO_3$ in the Cores of Gas Giants and Terrestrial Exoplanets, *Science* **311**(5763): 983–986.

Umemoto, K., Wentzcovitch, R. M., Wu, S., Ji, M., Wang, C.-Z. and Ho, K.-M. (2017). Phase transitions in $MgSiO_3$ post-perovskite in super-Earth mantles, *Earth and Planetary Science Letters* **478**: 40–45.

Unterborn, C., Schaefer, L. and Krijt, S. (2020). The composition of rocky planets, *Planetary Diversity: Rocky planet processes and their observational signatures*, IOP Publishing Bristol, UK, pp. 5–1.

Unterborn, C. T., Desch, S. J., Haldemann, J., Lorenzo, A., Schulze, J. G., Hinkel, N. R. and Panero, W. R. (2023). The Nominal Ranges of Rocky Planet Masses, Radii, Surface Gravities, and Bulk Densities, **944**(1): 42.

Unterborn, C. T., Desch, S. J., Hinkel, N. R. and Lorenzo, A. (2018). Inward migration of the TRAPPIST-1 planets as inferred from their water-rich compositions, *Nature Astronomy* **2**: 297–302.

Unterborn, C. T., Hinkel, N. R. and Desch, S. J. (2018). Updated Compositional Models of the TRAPPIST-1 Planets, *Research Notes of the American Astronomical Society* **2**(3): 116.

Unterborn, C. T., Johnson, J. A. and Panero, W. R. (2015). Thorium Abundances in Solar Twins and Analogs: Implications for the Habitability of Extrasolar Planetary Systems, **806**(1): 139.

Unterborn, C. T. and Panero, W. R. (2019). The Pressure and Temperature Limits of Likely Rocky Exoplanets, *Journal of Geophysical Research (Planets)* **124**(7): 1704–1716.

Vach, S., Zhou, G., Huang, C. X., Rogers, J. G., Bouma, L. G., Douglas, S. T., Kunimoto, M., Mann, A. W., Barber, M. G., Quinn, S. N., Latham, D. W., Bieryla, A. and Collins, K. (2024). The Occurrence of Small, Short-period Planets Younger than 200 Myr with TESS, **167**(5): 210.

Valencia, D., O'Connell, R. J. and Sasselov, D. (2006). Internal structure of massive terrestrial planets, **181**(2): 545–554.

Valencia, D., Sasselov, D. D. and O'Connell, R. J. (2007). Radius and Structure Models of the First Super-Earth Planet, **656**(1): 545–551.

van den Berg, A. P., Yuen, D. A., Umemoto, K., Jacobs, M. H. G. and Wentzcovitch, R. M. (2019). Mass-dependent dynamics of terrestrial exoplanets using ab initio mineral properties, **317**: 412–426.

Van Eylen, V., Agentoft, C., Lundkvist, M. S., Kjeldsen, H., Owen, J. E., Fulton, B. J., Petigura, E. and Snellen, I. (2018). An asteroseismic view of the radius valley: stripped cores, not born rocky, **479**(4): 4786–4795.

Venturini, J., Guilera, O. M., Haldemann, J., Ronco, M. P. and Mordasini, C. (2020). The nature of the radius valley. Hints from formation and evolution models, **643**: L1.

Venturini, J., Ronco, M. P., Guilera, O. M., Haldemann, J., Mordasini, C. and Miller Bertolami, M. (2024). A fading radius valley towards M dwarfs, a persistent density valley across stellar types, **686**: L9.

Vilella, K., Choblet, G., Tsao, W. E. and Deschamps, F. (2020). Tidally Heated Convection and the Occurrence of Melting in Icy Satellites: Application to Europa, *Journal of Geophysical Research (Planets)* **125**(3): e06248.

Vinet, P., Ferrante, J., Rose, J. H. and Smith, J. R. (1987). Compressibility of solids, **92**(B9): 9319–9325.

Virtanen, P., Gommers, R., Oliphant, T. E., Haberland, M., Reddy, T., Cournapeau, D., Burovski, E., Peterson, P., Weckesser, W., Bright, J., van der Walt, S. J., Brett, M., Wilson, J., Millman, K. J., Mayorov, N., Nelson, A. R. J., Jones, E., Kern, R., Larson, E., Carey, C. J., Polat, İ., Feng, Y., Moore, E. W., VanderPlas, J., Laxalde, D., Perktold, J., Cimrman, R., Henriksen, I., Quintero, E. A., Harris, C. R., Archibald, A. M., Ribeiro, A. H., Pedregosa, F., van Mulbregt, P. and SciPy 1.0 Contributors (2020). SciPy 1.0: Fundamental Algorithms for Scientific Computing in Python, *Nature Methods* **17**: 261–272.

Viswanathan, V., Rambaux, N., Fienga, A., Laskar, J. and Gastineau, M. (2019). Observational Constraint on the Radius and Oblateness of the Lunar Core-Mantle Boundary, **46**(13): 7295–7303.

Vlasov, K., Audétat, A. and Keppler, H. (2023). H_2-H_2O immiscibility in Earth's upper mantle, *Contributions to Mineralogy and Petrology* **178**(7): 36.

Wade, J. and Wood, B. J. (2005). Core formation and the oxidation state of the Earth, *Earth and Planetary Science Letters* **236**(1-2): 78–95.

Wagner, W. and Pruß, A. (2002). The IAPWS Formulation 1995 for the Thermodynamic Properties of Ordinary Water Substance for General and Scientific Use, *Journal of Physical and Chemical Reference Data* **31**(2): 387–535.

Wahl, S. M., Hubbard, W. B., Militzer, B., Guillot, T., Miguel, Y., Movshovitz, N., Kaspi, Y., Helled, R., Reese, D., Galanti, E., Levin, S., Connerney, J. E. and Bolton, S. J. (2017). Comparing Jupiter interior structure models to Juno gravity measurements and the role of a dilute core, **44**(10): 4649–4659.

Wang, C., Lv, M., Hu, R., Wang, J. and Zhao, Y. (2024). Prediction of stability of tenfold-coordinated silica up to 200 TPa pressure based on ab initio calculations with all-electron pseudopotentials, **109**(13): 134112.

Wang, X., Li, L., Jiang, X., Fry, P. M., West, R. A., Nixon, C. A., Guan, L., Karandana G, T. D., Albright, R., Colwell, J. E., Guillot, T., Hofstadter, M. D., Kenyon, M. E., Mallama, A., Perez-Hoyos, S., Sanchez-Lavega, A., Simon, A. A., Wenkert, D. and Zhang, X. (2024). Cassini spacecraft reveals global energy imbalance of Saturn, *Nature Communications* **15**(1): 5045.

Weber, R. C., Lin, P.-Y., Garnero, E. J., Williams, Q. and Lognonné, P. (2011). Seismic Detection of the Lunar Core, *Science* **331**(6015): 309.

Werlen, A., Dorn, C., Burn, R., Schlichting, H. E., Grimm, S. L. and Young, E. D. (2025). Sub-Neptunes Are Drier than They Seem: Rethinking the Origins of Water-rich Worlds, **991**(1): L16.

Widemann, T., Ghail, R., Wilson, C., Titov, D., Straume, A. G., Ocampo, A., Bocanegra-Bahamon, T., Bruzzone, L., Campbell, B., Carter, L. et al. (2022). The envision mission to venus, *53rd Lunar and Planetary Science Conference*, pp. LPI–Contribution.

Williams, J. G., Konopliv, A. S., Boggs, D. H., Park, R. S., Yuan, D.-N., Lemoine, F. G., Goossens, S., Mazarico, E., Nimmo, F., Weber, R. C., Asmar, S. W., Melosh, H. J., Neumann, G. A., Phillips, R. J., Smith, D. E., Solomon, S. C., Watkins, M. M., Wieczorek, M. A., Andrews-Hanna, J. C., Head, J. W., Kiefer, W. S., Matsuyama, I., McGovern, P. J., Taylor, G. J. and Zuber, M. T. (2014). Lunar interior properties from the GRAIL mission, *Journal of Geophysical Research (Planets)* **119**(7): 1546–1578.

Woodland, A. B. (1998). The orthorhombic to high-P monoclinic phase transition in Mg-Fe Pyroxenes: Can it produce a seismic discontinuity?, **25**(8): 1241–1244.

Workman, R. K. and Hart, S. R. (2005). Major and trace element composition of the depleted MORB mantle (DMM), *Earth and Planetary Science Letters* **231**(1-2): 53–72.

Wu, S., Umemoto, K., Ji, M., Wang, C.-Z., Ho, K.-M. and Wentzcovitch, R. M. (2011). Identification of post-pyrite phase transitions in SiO_2 by a genetic algorithm, **83**(18): 184102.

Xie, M., Fu, J. and Belonoshko, A. B. (2025). Equation of state and thermodynamic properties of liquid fe-o in the earth's outer core, *Geoscience Frontiers* **16**(1): 101847.

Yang, Z., Song, Z., Wu, Z., Mao, H.-k. and Zhang, L. (2024). Iron silicate perovskite and postperovskite in the deep lower mantle, *Proceedings of the National Academy of Science* **121**(17): e2401281121.

Ye, Y., Prakapenka, V., Meng, Y. and Shim, S. H. (2017). Intercomparison of the gold, platinum, and MgO pressure scales up to 140 GPa and 2500 K, *Journal of Geophysical Research (Solid Earth)* **122**(5): 3450–3464.

Yokoo, S. and Hirose, K. (2024). Melting experiments on Fe-S-O-C alloys at Martian core conditions: Possible structures in the O- and C-bearing core of Mars, **378**: 234–244.

Yokoo, S., Hirose, K., Tagawa, S., Morard, G. and Ohishi, Y. (2022). Stratification in planetary cores by liquid immiscibility in fe-sh, *Nature Communications* **13**(1): 644.

Yoshizaki, T. and McDonough, W. F. (2020). The composition of Mars, **273**: 137–162.

Zeng, L., Jacobsen, S. B., Sasselov, D. D., Petaev, M. I., Vanderburg, A., Lopez-Morales, M., Perez-Mercader, J., Mattsson, T. R., Li, G., Heising, M. Z., Bonomo, A. S., Damasso, M., Berger, T. A., Cao, H., Levi, A. and Wordsworth, R. D. (2019). Growth model interpretation of planet size distribution, *Proceedings of the National Academy of Science* **116**(20): 9723–9728.

Zeng, L. and Sasselov, D. (2013). A Detailed Model Grid for Solid Planets from 0.1 through 100 Earth Masses, **125**(925): 227.

Zeng, L., Sasselov, D. D. and Jacobsen, S. B. (2016). Mass-Radius Relation for Rocky Planets Based on PREM, **819**(2): 127.

Zhang, H., Schmandt, B., Zhou, W.-Y., Zhang, J. S. and Maguire, R. (2022). A Single 520 km Discontinuity Beneath the Contiguous United States With Pyrolitic Seismic Properties, **49**(24): e2022GL101300.

Zhang, J. and Rogers, L. A. (2022). Thermal Evolution and Magnetic History of Rocky Planets, **938**(2): 131.

Zhang, Y., Zhang, S., Kuang, D. and Xiong, C. (2025). Equation of state parameters of hcp-fe up to super-earth interior conditions, *Crystals* **15**(3): 221.

Zhang, Z., Csányi, G. and Alfè, D. (2020). Partitioning of sulfur between solid and liquid iron under Earth's core conditions: Constraints from atomistic simulations with machine learning potentials, **291**: 5–18.

Zhang, Z., Sun, Y. and Wentzcovitch, R. M. (2023). PBE-GGA predicts the B8B2 phase boundary of FeO at Earth's core conditions, *Proceedings of the National Academy of Science* **120**(28): e2304726120.

Zharkov, V. N. and Kalinin, V. A. (1971). *Equations of state for solids at high pressures and temperatures*, Springer.

Zurkowski, C. C., Yang, J., Chariton, S., Prakapenka, V. B. and Fei, Y. (2022). Synthesis and Stability of an Eight-Coordinated Fe_3O_4 High-Pressure Phase: Implications for the Mantle Structure of Super-Earths, *Journal of Geophysical Research (Planets)* **127**(8): e07344.

Chapter 3

Conclusion

3.1 Summary

In this work, we have constructed an interior structure model that calculates planetary radii for a planetary mass, composition, temperature, and other input parameters. The purpose of this model is to infer the compositions of exoplanets, particularly exoplanets in the super-Earth and sub-Neptune regions of parameter space. This model is unique in that it simultaneously includes:

- A Gibbs free energy minimization equilibrium mineralogy inside the upper mantle
- High-pressure phases of mantle material
- Light elements in the liquid and solid core and partitioning between the two
- Temperature jumps at the top and bottom of the mantle
- A prescription to directly calculate transit radii
- An upper atmospheric temperature profile from radiative transfer equations
- Thermal terms in all EOS
- H/He non-ideal mixing
- EOS for Iron that extrapolates well to high pressures
- Rotation

We have validated this model by inputting the independently constrained parameters of Earth, Mars, the Moon, Mercury, Venus, and Europa and have retrieved radii and

moment of inertia coefficients within 0.5% or 1σ of the coefficients measured in reality for objects with well-constrained moments of inertia and 1% or 3σ otherwise.

Isocomposition curves generated with this model support the consensus that the super-Earth planets making up the lower-radius peak of the radius valley have Earth-like compositions and the sub-Neptune planets making up the higher-radius peak of the radius valley either have % level H/He or 10s of % level H_2O. This provides a necessary foundation for any speculative astrobiology related to these classes of planets.

Our model's up-to-date EOS and inclusion of additional physics results in kinks in planetary isocomposition curves where changes occur in the phases present within the planet. We fit power-law relationships $M = R^X$ between these kinks and find that planets get denser more rapidly with mass than captured by a singular power law. The usage of a signular power law nontheless is only accurate up to $\sim 8\ M_\oplus$. We also find that previous studies overestimate the radii of super-Mercury planets. Finally, we find that the power law $M = R^X$ exponent of pure planetary cores are greater than that of super-Earths–indiciating greater compressions–while water world planets and super-Earths are within 1% at sufficiently high masses that both have the same core state.

We now turn to future work, splitting it into improvements that could be made to the model presented here and ways that the model could be applied.

3.2 Future Work

3.2.1 Improvements to the Interior Structure Model

The text of Chapter 2 makes note of several simplifications made in the interior structure model, some of which can be relaxed in future publications.

The most prominent oversimplification compared to our current understanding of geophysics is the chemical inventory of the core, which likely does not reflect reality, with incorrect values of the core S and O abundances input in our model replicating the densities of the actual combination of elements within the core (Hirose et al.; 2013; Umemoto and Hirose; 2020; Hirose et al.; 2021). Although this inaccuracy does not effect Earth's core, it may mean that our results do not extrapolate to the interiors of other bodies, as may be indicated in Mars' profile (see Section 2.3.2). Hakim et al. (2018) provide EOS that could be used to include O, Si, and C in the solid core, while Ichikawa and Tsuchiya (2020) provide EOS that could be used to include Si, C, and H

in the liquid core. As these publications already have EOS included within our model, the infrastructure already exists to expand the core chemical inventory.

Coupled with an expansion of the core chemical inventory should be an automated process to determine the best-fit core compositions. Determining the core abundances that matched the profiles of Earth, Mars, the Moon, and Mercury were all done manually in this thesis, at the cost of several hours and results that were not fully minimized. A routine that iteratively guesses core chemical parameters in our interior structure model and attempts to fit the resultant core profile to the observed core profiles of solar system bodies would greatly simplify the tweaking of core properties and could be of broader use to the community.

The other most prominent issue within our model is the usage of BM3 for some high pressure phases (FeO and $FeSiO_3$) due to the lack–to our knowledge–of literature EOS with the appropriate functional form of high pressure extrapolation (Morard et al.; 2022; Greenberg et al.; 2023). As functional forms are merely fits to data and do not require the gathering of additional data by themselves, future publications should fit EOS that extrapolate to higher pressures directly to the P-T-ρ data obtained via experiments or simulation. The inverse issue, the application of high-pressure EOS to pressures below where they are appropriate, happens for liquid Fe alloys in the core, leading to inferences of very anamolously high light element contents in the cores of the Moon and Mars (see Sections 2.3.3 and 2.3.2). Future work will switch Fe alloy EOS based off of pressure rather than planetary layer.

The non-inclusion of water outside the water layer discussed in Section 2.5.3 is justified as a realistic end member in the text, which is accurate, however, if water does truly go into the core, mantle, and/or envelope of planets in significant quantities, the impact on the planetary radius could be an order of magnitude larger than all of the improvements this model has made on the literature. Haldemann et al. (2024) provide a prescription for mixing water into the planetary H/He envelope while avoiding non-physical profiles. Future work could adopt this prescription as well as the miscibility curves of Bergermann et al. (2024). Mixing of water into the planetary mantle could be achieved with the additive volume law and a water molar mass fraction in the mantle following Dorn and Lichtenberg (2021). Mixing of water into the planetary core could be achieved using Equation 2.18 and Luo et al. (2024)'s equation for hydrated liquid Fe. As our model is static, it cannot simulate the process by which water enters the planetary interior, necessitating that any future inclusion of water sequestration either (1) consider the extreme edge case in which all possible water is sequestered or (2) be coupled with

a model of planetary formation and differentiation that can track how much water is actually sequestered.

The simplified effect of light elements on melting temperatures captured by Equation 2.22 does not affect our reproduction of the Earth's interior but does appear to affect our reproduction of Mercury's interior (see Section 2.3.5). Even if the effects on bulk properties are minor, even small differences change the inference of the fundamental nature of the planet (mostly solid or mostly liquid) because planetary pressure-temperature profiles can be near the melting curve for much of the interior. This could lead to inferences about other properties that are wrong, such as predicting a planet will not have a magnetic field and thus be uninhabitable due to having a purely solid core, even when a proper treatment of the melting curve would reveal a partially liquid planetary core (González-Cataldo and Militzer; 2023). As alluded to in Appendix A5, explicitly including the eutectic of iron alloy systems (the fact that $T_{\rm melt}$ is not monotonic with increasing prevalence of a secondary species) would improve the model's replication of the core. A more realistic temperature profile would also remove the need to artificially alter Equation 2.22 for high-Fe mantles such as Europa. The review article of Breuer et al. (2015) provides a starting place for eutectics of the Fe-S system to include in future works. A notable consequence of including more elements in the core and more realisitc temperatures is that Si affects the melting curve of Fe far less than S and C do (Knibbe et al.; 2025), so a model with Si and S in the core could vary core densities to come closer in line to reality without significantly impacting the melting temperature, as compared to our current model in which accurately retrieving the radius at which the core melts cannot be simultaneously achieved with accurately retrieving the bulk core density.

Although our validation on solar system bodies and relative chemical abundances justifies our limited mantle chemical inventory, our model is still inconsistent with Earth's parameters at the 0.1% level and thus the inclusion of additional chemicals may be justified. Al and Ca, the two most abundant mantle elements not included within our model (Palme and O'Neill; 2014), are included within HeFESTo and thus their addition to the lower mantle could be achieved without modifying the overall framework of the model (Stixrude and Lithgow-Bertelloni; 2005, 2011, 2024). The relative lack of high-pressure EOS for these materials may impose a difficulty, however their relatively low abundances may justify only including Al and Ca in the upper (non-ppv) mantle and re-normalizing the elemental abundances below it.

The discrepancy between our model and seismic data in Mars' lithosphere is stark, motivating the introduction of a parameterization for a conductive lid–a layer at the top

of the planetary mantle and crust where heat is transported via conduction rather than convection. A conductive lid can be parameterized as a thermal boundary layer with a thickness determined by the local material properties, determined by the local EOS, over which temperature increases linearly from the surface value to the mantle melting point (Valencia et al.; 2007). This would require attaining viscosity parameters from the literature, such as those resulting from the investigations of Stamenković et al. (2012); Karato (2011); Hirth and Kohlstedt (2003). Although the conductive lid is likely small for super-Earths, its inclusion should allow for a noticeably more accurate replication of planetary radii in the validation sample while self-consistently reducing in importance at higher masses.

The physics of the conductive lid thermal boundary layer are similar to that of the core-mantle boundary layer, so the new prescription for a conductive lid could also be applied to the planetary interior (Foley et al.; 2020). This could allow for the model to have a temperature jump at the core-mantle boundary that is not instantaneous, allowing us to test the hypothesis that our model may contain ppv while Earth's mantle doesn't due to enhanced temperatures or that Earth's pressure-temperature profile intersects the pv-ppv transition twice (Hernlund and Labrosse; 2007). This would also allow for testing for the existence of the Martian molten silicate layer found by Khan et al. (2023).

There are several phase transitions that the authors are aware of but are not included in the model. The EOS most lacking in phase transitions is SiO_2, for which we have one solid EOS over a regime in which several phase transitions are reported followed by a transition at very high pressures. Future versions of the model could include I4/mmm, cotunnite, pyrite, and α-PbO SiO_2 (Tsuchiya and Tsuchiya; 2011; Lyle et al.; 2015; Wang et al.; 2024). The transitions of Fe at very high pressures could also be included, which would merely involve using the EOS from Dorogokupets et al. (2017) already within our model again at higher pressures, although it should be cautioned that the Vinet EOS becomes unreliable at these pressures.

Finally, the radiative transfer model of the atmosphere by Parmentier and Guillot (2014); Parmentier et al. (2015) used in this publication does not include clouds, even though clouds have appeared in most (but not all) sub-Neptune to Neptune-sized planets whose atmospheres have been accessed by James Webb Space Telescope (JWST) and the Hubble Space Telescope (HST) before it (Brande et al.; 2024; Kreidberg et al.; 2014; Kempton et al.; 2023; Radica et al.; 2024; Estrela et al.; 2022; Davenport et al.; 2025).

3.2.2 Applications of the Interior Structure Model

The work presented herein is a strictly forward model: for some given planetary composition, it computes planetary observables. Often, it is the opposite, retrieval model that is of interest: for some given observables, what is the inferred planet composition? Several of these models exist in the literature (e.g. Dorn et al.; 2015, 2017; Haldemann et al.; 2024; Acuña et al.; 2021) and all provide a less complete phase diagram than the one presented here. The method of inverting the problem is Markov Chain Monte Carlo (MCMC) sampling using the Metropolis algorithm, in which model parameters are iteratively perturbed to new values with acceptance probabilities based on the relative likelihood functions of the new and old values (Dorn et al.; 2015). In principal, all that must be done is take the current forward model and feed it as a function into a MCMC algorithm. However, the current computational cost of the model is too high ($\sim$ 10 minutes for a single H/He enveloped planet on a mid-end laptop) for MCMC retrieval, which requires $\sim 10^5$ samples for a single planet (Haldemann et al.; 2023). Alternatively, a large (N$\sim$one million) dataset of forward planets could be used to train a machine learning algorithm (Haldemann et al.; 2023; Zhao and Ni; 2021; Baumeister et al.; 2020). In either case, pursuing this ultimate goal thus relies on computational and numerical improvements more than any additional physics.

The generation of a large dataset of model planets can itself be of use, as demonstrated by Unterborn et al. (2023)'s grid showing the nominal parameter space for rocky planets. Generating such grids for this model for rocky, water world, and H/He-enveloped worlds would provide an immediate physically-motivated reference point for observers to determine if newly discovered planets are rocky or volatile-enriched based off of density alone.

The model presented here would also provide great utility if applied to a large sample of observed exoplanets to determine their average properties, sidestepping the problems of degeneracy and observational uncertainties through sheer numbers, as has been done by Plotnykov and Valencia (2020); Adibekyan et al. (2021); Schulze et al. (2021) using earlier models in the context of comparing planetary compositions to their host stars. The high-pressure EOS of this model allows for more reliable inferred compositions for more massive planets, effectively increasing the parameter space over which such searches could be conducted.

A final application of this model for which work has already begun is its usage to

determine radii for planets synthetically generated by planet population synthesis models (PPSM), models of planet formation. PPSM synergize well with interior structure models such as ours because the many otherwise near-impossible to determine a priori free parameters such as planetary core mass fractions are directly simulated. Application of earlier versions of this model to the McMaster PPSM of Alessi et al. (2017); Alessi and Pudritz (2018); Alessi, Pudritz and Cridland (2020); Alessi, Inglis and Pudritz (2020); Alessi and Pudritz (2022) has found that the inclusion of physics not included in the original MPPSM–namely the thermal expansion of a highly irradiated steam atmosphere–shifts planetary radii in the super-Earth to sub-Neptune regime systematically higher and closer together. This effect has a major impact on the MPPSM's ability to recreate the radius valley. The completion of this work with a modern version of this model as well as comparative studies between the MPPSM and other PPSM, such as the Bern PPSM (Emsenhuber et al.; 2021a,b; Burn et al.; 2024)–which includes significantly more physics than the MPPSM but makes the notable exclusion of disk winds, which may actually be the primary driver of angular momentum transport within protoplanetary disks (Alessi and Pudritz; 2022)–or the PPSM of Izidoro et al. (2021); Izidoro, Dasgupta, Raymond, Deienno, Bitsch and Isella (2022); Izidoro, Schlichting, Isella, Dasgupta, Zimmermann and Bitsch (2022); Shibata and Izidoro (2025) which accurately reproduces the radius valley but requires seeding with artificially placed (but physically motivated) rings of planetesimals, would provide much insight.

Bibliography

Acuña, L., Deleuil, M., Mousis, O., Marcq, E., Levesque, M. and Aguichine, A. (2021). Characterisation of the hydrospheres of TRAPPIST-1 planets, **647**: A53.

Adibekyan, V., Dorn, C., Sousa, S. G., Santos, N. C., Bitsch, B., Israelian, G., Mordasini, C., Barros, S. C. C., Delgado Mena, E., Demangeon, O. D. S., Faria, J. P., Figueira, P., Hakobyan, A. A., Oshagh, M., Soares, B. M. T. B., Kunitomo, M., Takeda, Y., Jofré, E., Petrucci, R. and Martioli, E. (2021). A compositional link between rocky exoplanets and their host stars, *Science* **374**(6565): 330–332.

Alessi, M., Inglis, J. and Pudritz, R. E. (2020). Formation of planetary populations - III. Core composition and atmospheric evaporation, **497**(4): 4814–4833.

Alessi, M. and Pudritz, R. E. (2018). Formation of planetary populations - I. Metallicity and envelope opacity effects, **478**(2): 2599–2617.

Alessi, M. and Pudritz, R. E. (2022). Combined effects of disc winds and turbulence-driven accretion on planet populations, **515**(2): 2548–2577.

Alessi, M., Pudritz, R. E. and Cridland, A. J. (2017). On the formation and chemical composition of super Earths, **464**(1): 428–452.

Alessi, M., Pudritz, R. E. and Cridland, A. J. (2020). Formation of planetary populations - II. Effects of initial disc size and radial dust drift, **493**(1): 1013–1033.

Baumeister, P., Padovan, S., Tosi, N., Montavon, G., Nettelmann, N., MacKenzie, J. and Godolt, M. (2020). Machine-learning Inference of the Interior Structure of Low-mass Exoplanets, **889**(1): 42.

Bergermann, A., French, M. and Redmer, R. (2024). Ab initio calculation of the miscibility diagram for mixtures of hydrogen and water, **109**(17): 174107.

Brande, J., Crossfield, I. J. M., Kreidberg, L., Morley, C. V., Barman, T., Benneke, B., Christiansen, J. L., Dragomir, D., Fortney, J. J., Greene, T. P., Hardegree-Ullman, K. K., Howard, A. W., Knutson, H. A., Lothringer, J. D. and Mikal-Evans, T. (2024). Clouds and Clarity: Revisiting Atmospheric Feature Trends in Neptune-size Exoplanets, **961**(1): L23.

Breuer, D., Rueckriemen, T. and Spohn, T. (2015). Iron snow, crystal floats, and inner-core growth: modes of core solidification and implications for dynamos in terrestrial planets and moons, *Progress in Earth and Planetary Science* **2**: 39.

Burn, R., Mordasini, C., Mishra, L., Haldemann, J., Venturini, J., Emsenhuber, A. and Henning, T. (2024). A radius valley between migrated steam worlds and evaporated rocky cores, *Nature Astronomy* **8**: 463–471.

Davenport, B., Kempton, E. M. R., Nixon, M. C., Ih, J., Deming, D., Fu, G., May, E. M., Bean, J. L., Gao, P., Rogers, L. and Malik, M. (2025). TOI-421 b: A Hot Sub-Neptune with a Haze-free, Low Mean Molecular Weight Atmosphere, **984**(2): L44.

Dorn, C., Khan, A., Heng, K., Connolly, J. A. D., Alibert, Y., Benz, W. and Tackley, P. (2015). Can we constrain the interior structure of rocky exoplanets from mass and radius measurements?, **577**: A83.

Dorn, C. and Lichtenberg, T. (2021). Hidden Water in Magma Ocean Exoplanets, **922**(1): L4.

Dorn, C., Venturini, J., Khan, A., Heng, K., Alibert, Y., Helled, R., Rivoldini, A. and Benz, W. (2017). A generalized Bayesian inference method for constraining the interiors of super Earths and sub-Neptunes, **597**: A37.

Dorogokupets, P. I., Dymshits, A. M., Litasov, K. D. and Sokolova, T. S. (2017). Thermodynamics and Equations of State of Iron to 350 GPa and 6000 K, *Scientific Reports* **7**: 41863.

Emsenhuber, A., Mordasini, C., Burn, R., Alibert, Y., Benz, W. and Asphaug, E. (2021a). The New Generation Planetary Population Synthesis (NGPPS). I. Bern global model of planet formation and evolution, model tests, and emerging planetary systems, **656**: A69.

Emsenhuber, A., Mordasini, C., Burn, R., Alibert, Y., Benz, W. and Asphaug, E. (2021b). The New Generation Planetary Population Synthesis (NGPPS). II. Planetary population of solar-like stars and overview of statistical results, **656**: A70.

Estrela, R., Swain, M. R. and Roudier, G. M. (2022). A Temperature Trend for Clouds and Hazes in Exoplanet Atmospheres, **941**(1): L5.

Foley, B. J., Houser, C., Noack, L. and Tosi, N. (2020). The heat budget of rocky planets, *Planetary Diversity: Rocky planet processes and their observational signatures*, IOP Publishing Bristol, UK, pp. 4–1.

González-Cataldo, F. and Militzer, B. (2023). Ab initio determination of iron melting at terapascal pressures and Super-Earths core crystallization, *Physical Review Research* **5**(3): 033194.

Greenberg, E., Nazarov, R., Landa, A., Ying, J., Hood, R. Q., Hen, B., Jeanloz, R., Prakapenka, V. B., Struzhkin, V. V., Rozenberg, G. K. and Leonov, I. V. (2023). Phase transitions and spin state of iron in FeO under the conditions of Earth's deep interior, **107**(24): L241103.

Hakim, K., Rivoldini, A., Van Hoolst, T., Cottenier, S., Jaeken, J., Chust, T. and Steinle-Neumann, G. (2018). A new ab initio equation of state of hcp-Fe and its implication on the interior structure and mass-radius relations of rocky super-Earths, **313**: 61–78.

Haldemann, J., Dorn, C., Venturini, J., Alibert, Y. and Benz, W. (2024). BICEPS: An improved characterization model for low- and intermediate-mass exoplanets, **681**: A96.

Haldemann, J., Ksoll, V., Walter, D., Alibert, Y., Klessen, R. S., Benz, W., Koethe, U., Ardizzone, L. and Rother, C. (2023). Exoplanet characterization using conditional invertible neural networks, **672**: A180.

Hernlund, J. W. and Labrosse, S. (2007). Geophysically consistent values of the perovskite to post-perovskite transition Clapeyron slope, **34**(5): L05309.

Hirose, K., Labrosse, S. and Hernlund, J. (2013). Composition and State of the Core, *Annual Review of Earth and Planetary Sciences* **41**: 657–691.

Hirose, K., Wood, B. and Vočadlo, L. (2021). Light elements in the earth's core, *Nature Reviews Earth & Environment* **2**(9): 645–658.

Hirth, G. and Kohlstedt, D. (2003). Rheology of the upper mantle and the mantle wedge: A view from the experimentalists, *Geophysical Monograph Series* **138**: 83–105.

Ichikawa, H. and Tsuchiya, T. (2020). Ab Initio Thermoelasticity of Liquid Iron-Nickel-Light Element Alloys, *Minerals* **10**(1): 59.

Izidoro, A., Bitsch, B., Raymond, S. N., Johansen, A., Morbidelli, A., Lambrechts, M. and Jacobson, S. A. (2021). Formation of planetary systems by pebble accretion and migration. Hot super-Earth systems from breaking compact resonant chains, **650**: A152.

Izidoro, A., Dasgupta, R., Raymond, S. N., Deienno, R., Bitsch, B. and Isella, A. (2022). Planetesimal rings as the cause of the Solar System's planetary architecture, *Nature Astronomy* **6**: 357–366.

Izidoro, A., Schlichting, H. E., Isella, A., Dasgupta, R., Zimmermann, C. and Bitsch, B. (2022). The Exoplanet Radius Valley from Gas-driven Planet Migration and Breaking of Resonant Chains, **939**(2): L19.

Karato, S.-i. (2011). Rheological structure of the mantle of a super-Earth: Some insights from mineral physics, **212**(1): 14–23.

Kempton, E. M. R., Zhang, M., Bean, J. L., Steinrueck, M. E., Piette, A. A. A., Parmentier, V., Malsky, I., Roman, M. T., Rauscher, E., Gao, P., Bell, T. J., Xue, Q., Taylor, J., Savel, A. B., Arnold, K. E., Nixon, M. C., Stevenson, K. B., Mansfield, M., Kendrew, S., Zieba, S., Ducrot, E., Dyrek, A., Lagage, P.-O., Stassun, K. G., Henry, G. W., Barman, T., Lupu, R., Malik, M., Kataria, T., Ih, J., Fu, G., Welbanks, L. and McGill, P. (2023). A reflective, metal-rich atmosphere for GJ 1214b from its JWST phase curve, **620**(7972): 67–71.

Khan, A., Huang, D., Durán, C., Sossi, P. A., Giardini, D. and Murakami, M. (2023). Evidence for a liquid silicate layer atop the Martian core, **622**(7984): 718–723.

Knibbe, J. S., Rivoldini, A., Zhao, Y. and Van Hoolst, T. (2025). On the thermal evolution and magnetic field generation of planet Mercury, *Physics of the Earth and Planetary Interiors* **363**: 107348.

Kreidberg, L., Bean, J. L., Désert, J.-M., Benneke, B., Deming, D., Stevenson, K. B., Seager, S., Berta-Thompson, Z., Seifahrt, A. and Homeier, D. (2014). Clouds in the atmosphere of the super-Earth exoplanet GJ1214b, **505**(7481): 69–72.

Luo, H., Dorn, C. and Deng, J. (2024). The interior as the dominant water reservoir in super-Earths and sub-Neptunes, *Nature Astronomy* **8**: 1399–1407.

Lyle, M. J., Pickard, C. J. and Needs, R. J. (2015). Prediction of 10-fold coordinated TiO_2 and SiO_2 structures at multimegabar pressures, *Proceedings of the National Academy of Science* **112**(22): 6898–6901.

Morard, G., Antonangeli, D., Bouchet, J., Rivoldini, A., Boccato, S., Miozzi, F., Boulard, E., Bureau, H., Mezouar, M., Prescher, C., Chariton, S. and Greenberg, E. (2022). Structural and Electronic Transitions in Liquid FeO Under High Pressure, *Journal of Geophysical Research (Solid Earth)* **127**(11): e2022JB025117.

Palme, H. and O'Neill, H. (2014). Cosmochemical estimates of mantle composition. planets, asteriods, comets and the solar system, volume 2 of treatise on geochemistry . edited by andrew m. davis.

Parmentier, V. and Guillot, T. (2014). A non-grey analytical model for irradiated atmospheres. I. Derivation, **562**: A133.

Parmentier, V., Guillot, T., Fortney, J. J. and Marley, M. S. (2015). A non-grey analytical model for irradiated atmospheres. II. Analytical vs. numerical solutions, **574**: A35.

Plotnykov, M. and Valencia, D. (2020). Chemical fingerprints of formation in rocky super-Earths' data, **499**(1): 932–947.

Radica, M., Coulombe, L.-P., Taylor, J., Albert, L., Allart, R., Benneke, B., Cowan, N. B., Dang, L., Lafrenière, D., Thorngren, D., Artigau, É., Doyon, R., Flagg, L., Johnstone, D., Pelletier, S. and Roy, P.-A. (2024). Muted Features in the JWST NIRISS Transmission Spectrum of Hot Neptune LTT 9779b, **962**(1): L20.

Schulze, J. G., Wang, J., Johnson, J. A., Gaudi, B. S., Unterborn, C. T. and Panero, W. R. (2021). On the Probability That a Rocky Planet's Composition Reflects Its Host Star, **2**(3): 113.

Shibata, S. and Izidoro, A. (2025). Formation of Super-Earths and Mini-Neptunes from Rings of Planetesimals, **979**(2): L23.

Stamenković, V., Noack, L., Breuer, D. and Spohn, T. (2012). The Influence of Pressure-dependent Viscosity on the Thermal Evolution of Super-Earths, **748**(1): 41.

Stixrude, L. and Lithgow-Bertelloni, C. (2005). Thermodynamics of mantle minerals - I. Physical properties, *Geophysical Journal International* **162**(2): 610–632.

Stixrude, L. and Lithgow-Bertelloni, C. (2011). Thermodynamics of mantle minerals - II. Phase equilibria, *Geophysical Journal International* **184**(3): 1180–1213.

Stixrude, L. and Lithgow-Bertelloni, C. (2024). Thermodynamics of mantle minerals - III: the role of iron, *Geophysical Journal International* **237**(3): 1699–1733.

Tsuchiya, T. and Tsuchiya, J. (2011). Prediction of a hexagonal SiO_2 phase affecting stabilities of $MgSiO_3$ and $CaSiO_3$ at multimegabar pressures, *Proceedings of the National Academy of Science* **108**(4): 1252–1255.

Umemoto, K. and Hirose, K. (2020). Chemical compositions of the outer core examined by first principles calculations, *Earth and Planetary Science Letters* **531**: 116009.

Unterborn, C. T., Desch, S. J., Haldemann, J., Lorenzo, A., Schulze, J. G., Hinkel, N. R. and Panero, W. R. (2023). The Nominal Ranges of Rocky Planet Masses, Radii, Surface Gravities, and Bulk Densities, **944**(1): 42.

Valencia, D., Sasselov, D. D. and O'Connell, R. J. (2007). Radius and Structure Models of the First Super-Earth Planet, **656**(1): 545–551.

Wang, C., Lv, M., Hu, R., Wang, J. and Zhao, Y. (2024). Prediction of stability of tenfold-coordinated silica up to 200 TPa pressure based on ab initio calculations with all-electron pseudopotentials, **109**(13): 134112.

Zhao, Y. and Ni, D. (2021). Machine learning techniques in studies of the interior structure of rocky exoplanets, **650**: A177.

A1 Saturn

Our model does not include physics critical for gas giant interior models such as helium rain, diffuse cores, or conductive temperature gradients (Sur et al.; 2025, 2024; Mankovich and Fuller; 2021; Mankovich and Fortney; 2020; Preising et al.; 2023). Additionally, Saturn's equilibrium temperature is outside of the boundaries of the Parmentier et al. (2015) atmospheric profile fits that we use, forcing us to use an equilibrium temperature of 100 K rather than Saturn's actual value. We thus do not include Saturn in our validation sample and discourage the use of our model for gas giants.

Nevertheless, Saturn has a mass $< 100 M_\oplus$ and serves as a useful edge case test that our prescription for H/He and high-density matter is sensible, bolstering confidence in the applicability of our model to sub-Neptunes with few % H/He envelopes that are within the scope of our model but do not exist in the solar system and thus for which we have no direct validation.

We take Saturn as having its reported Albdeo of 0.41 (Wang et al.; 2024), $Z_{\rm atm} = 3.16$ roughly following the upper atmosphere value found in Sur et al. (2025), solar $w_{\rm H}$ and $w_{\rm He}$, and a non-H/He center that is 50% water and 50% Earthlike. If we take the center as having the mass of Saturn's core found in the model of Sur et al. (2025) that replicates Saturn's current properties well, we get a radius of $9.0615 R_\oplus$ (-0.86%) and a MoIC of 0.25566[1] (16.208%). If we take the total mass of Saturn's fuzzy core as $17 M_\oplus$–as derived by observations of pulsation modes in Saturn's rings originating from Saturn's interior (Mankovich and Fuller; 2021)–we get a radius of $8.3078 R_\oplus$ (-9.11%) and a MoIC of 0.22896 (4.072%). Although high, we note that our trend in errors is directionally correct: adding more material to the center decreases the planetary radii, indicating a higher average density, and decreases the planetary MoIC, indicating a greater degree of mass concentration towards the planet's center.

The most prominent reason for our error is our simplified temperature structure. The combined effects of Helium rain and conduction cause our temperature at $\frac{m}{M_{\rm pl}} = 0.2$ to be ∼12,000 K lower than Sur et al. (2025)'s model at those temperatures (15,000 K v. 3,000 K). This nearly order of magnitude lower temperature leads to systematically higher densities, explaining our systematic underprediction of Saturn's radius regardless of the core mass we assume. Applying our temperature jump at the mantle-envelope

[1] As is standard for Saturn (Saillenfest et al.; 2021), we normalize Saturn's MoI using our model's equatorial radius in Eq. 2.48 rather than using Saturn's volume-equivalent radius. Note that Eq. 2.48 assumes spherical symmetry, we do not account for the flattening of objects in our MoI calculations.

interface means that this discrepancy disappears within the mantle and core of Saturn. This discrepancy starts to occur under a total H/He envelope mass of $\sim 25 M_\oplus$, so we estimate that our model still applies well to planets with $w_{\mathrm{H/He}} \lesssim 20\%$.

Another possible reason for our model's underprediction of Saturn's radius is that our EOS predict higher densities at high pressures compared to the literature due to phase transitions and using a Holzapfel EOS for iron (as opposed to assuming silicates are in the post-perovskite and using a Keane EOS for iron as in Zhang and Rogers (2022)). If this were the case, a version of our model including more physics relevant to gas giants would still predict smaller Saturn radii than the literature when using the same input parameters.

We do note that replicating Saturn's radius is difficult even for interior structure models more suited to it: Sur et al. (2025) find a radius of Saturn 1.18% smaller than reality while reproducing Saturn's surface temperature and J_2 gravitational moment within 0.13% and 0.4%, respectively.

A2 Example Planet Profile

In Figure A0.1 we plot the interior structure of a $20 M_\oplus$ Super Earth. We choose this high mass–nearing the highest mass super-Earths detected–to show all mantle transitions in our model. Note the relatively small jump caused by the recombination of MgO and $MgSiO_3$ into Mg_2SiO_4 and large jump caused by the dissociation of Mg_2SiO_4 into MgO and SiO_2. Also note how the higher surface gravity of the planet causes mantle features to come closer together.

A3 Numerical Details

Our solver is multi-threaded, solving five problems at once on different threads. Two threads integrate inward from the surface, one for the guessed radius and another for a slightly higher value of the radius. Three threads integrate outward from the core, one for the guessed pressure and temperature, one for a slightly higher value of pressure, and one for a slightly higher value of temperature. The integrations at slightly different values are calculated to perform numerical derivation for the Newton-Raphson method. We find that a value of slightly larger of a factor of 10^{-4} yields universal convergence within our parameter space.

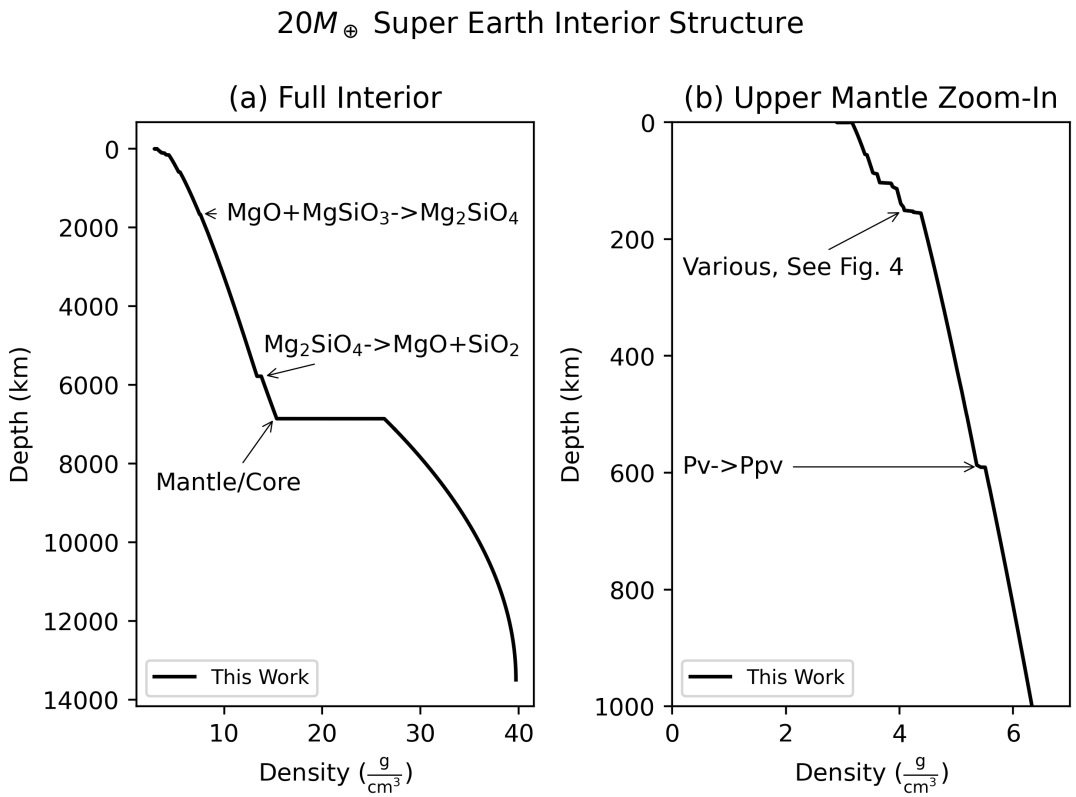

FIGURE A0.1: An example profile of a $20M_\oplus$ super-Earth. Transition and boundary notation is the same as in Figure 2.4. The uppermost mantle contains many phase transitions in close proximity in the same order as in Figure 2.4.

The mass at which our outwards and inwards integrations meet is by default the mass of the core, but can be iteratively reduced to 0.75 times the inner-outer core boundary if the melting curve and temperature profile have similar slopes to promote convergence. The mass must be less than or equal to the core mass as the temperature jump that occurs at the outer core can only be performed when integrating inwards. In the case where $w_{\text{Core}} = 0$, our meeting mass is half the total mass.

We have found that imposing an agreement of r, P, and T of a factor of 10^{-4} leads to results only $\sim 10^{-8}$ different from imposing an agreement of 10^{-6} and thus choose our threshold for accepting a solution as 10^{-4} because further improvements from a lower threshold are minuscule. Our chosen threshold for relative error in Cash-Karp steps is 10^{-7}, which causes differing results of order $\sim 10^{-10}$ compared to 10^{-9}. To avoid proximity to the divergence of r, we treat $\frac{m}{m_p} = 10^{-5}$ as the core of the planet, changing

this value to $\frac{m}{m_p} = 10^{-4}$ results in a change in radii by only $\sim 10^{-9}$. Lowering this value by an order of magnitude results in numerical instabilities due to proximity to the numerical singularity at the core.

We need reasonable values of the pressure and temperature of the planetary core to begin iterating. We attain these by integrating from the outer boundary condition to the inner boundary condition and refining our guesses via the Newton-Raphson method (we perform single-shooting integration to seed our initial guess in double-shooting integration).

Where we construct our own EOS table, they are uniformly spaced in log space such that $\frac{P_{i+1}}{P_i} = \frac{T_{i+1}}{T_i} = 1.01$. For the HeFESTo tables generated by Perple_X, we use the highest possible number of datapoints and construct square tables. This corresponds to spacings of $P_{i+1}/P_i \lesssim 1.012$ and $T_{i+1} - T_i \lesssim 3$ K (the maximum number of datapoints permitted depends on composition). We interpolate in log space for all tables besides HeFESTo, where we interpolate in linear space. This is because the parameter space of HeFESTo is the smallest of our dataset.

As r and m are not identically zero at our inner boundary condition, calculations of the local critical rotation can be unreliable for guesses too far from the solution. We thus set $\omega = \Omega f(m_\mathrm{p})/\sqrt{Gm_\mathrm{p}}$ when single shooting, where $f(m_\mathrm{p})$ is a rough estimate of the planetary radius from its mass. We found that the $\frac{M}{M_\oplus} = (1 + 0.55w_{\mathrm{H_2O}} - 0.14w_{\mathrm{H_2O}}^2)(\frac{R}{R_\oplus})^{\frac{1}{3.7}}$ relation of Zeng et al. (2019), multiplied by 1.5 for planets with envelope mass fractions above 10^{-2} and 2 for planets with equilibrium temperatures above or equal to 700 K (if they have a non-condensed surface) was sufficient for this purpose.

Even for guesses close to the solution, the calculation of ω for $\frac{m}{m_\mathrm{p}} < 10^{-4}$ is unreliable. We thus set $r_e = r$ at these small masses.

A4 Constants

We take molar masses for all elements from NIST[2]. We take the value for G from NIST of $6.67430 * 10^{-11} \frac{\mathrm{m}^3}{\mathrm{kgs}^2}$[3].

We take the mass of Earth as $5.9723651 * 10^{24}$ kg from Moulik and Ekström (2025) (atmospheric mass included) and the radius of Earth as $6.371000 * 10^6$ m from Moulik and Ekström (2025). We take Earth's rotational period as 0.997270 days following Moulik

[2] `https://webbook.nist.gov/`

[3] `https://physics.nist.gov/cuu/pdf/wall_2022.pdf`

and Ekström (2025)'s value of Earth's angular velocity. We take Earth's irradiance as 1360.8 $\frac{\mathrm{W}}{\mathrm{m}^2}$ following Kopp and Lean (2011), which we note is from the 2008 solar minimum and thus a lower bound.

We take the mass of the moon as $7.3463 * 10^{22}$ kg, radius of the moon as $1.737151 * 10^6$ m, and MoIC of the moon as 0.393112 ± 0.000012 from Williams et al. (2014).

We take the mass of Mars $6.417 * 10^{23}$ kg, the radius of Mars as 3389.5 km, and the MoIC of Mars as 0.3634 following Khan et al. (2022); Konopliv et al. (2020); Archinal et al. (2018).

We take the mass of Venus as $4.8673 * 10^{24}$ kg following Saliby et al. (2023). We take the radius of Venus as 6051.8 km following Archinal et al. (2018). We take the MoIC of Venus as 0.337 ± 0.024 following Margot et al. (2021).

We take the mass of Europa as $4.79982 * 10^{22}$ kg following Anderson et al. (1998) and the radius of Europa as 1560.8 km following Archinal et al. (2018). We use the instellation of Europa of 51 $\frac{\mathrm{W}}{\mathrm{m}^2}$ and rotational period of Europa of 3.547 days from Ashkenazy (2016). We take the MoIC of Europa as 0.3547 ± 0.0024 following Gomez Casajus et al. (2021), higher than the previously-accepted value of 0.346 ± 0.005 following Anderson et al. (1998).

We take the radius of Mercury as 2439.4 km following Archinal et al. (2018). We take the mass of Mercury as $3.3009999 * 10^{23}$ kg and MoIC of Mercury as 0.333 ± 0.005 following Genova et al. (2019). We get a Mercury rotation period of 58.646146 days from Mazarico et al. (2014).

We take the mass of Saturn as $5.6845789 * 10^{26}$ kg following Jacobson et al. (2006). We take the radius of Saturn as 58232 km following Archinal et al. (2018). This is at a pressure of 10^5 Pa, we report Saturn radii at 10^5 Pa rather than the 100 Pa outer boundary to account for this. We take the bulk rotation period of Saturn as 11.18 hours following Mankovich et al. (2019). We take the Moment of Inertia of Saturn as 0.22 ± 0.022 following Fortney et al. (2018); Helled (2018), although note that Militzer and Hubbard (2023) report a much more constrained value on the lower end of 0.2181 ± 0.0002 using an interior model of Saturn.

For all solar system bodies beyond those specified, we take masses from JPL[4].

[4] `https://ssd.jpl.nasa.gov/planets/phys_par.html` for planets, `https://ssd.jpl.nasa.gov/sats/phys_par/` for moons

In the body text, we reduce the number of significant figures of the pressure changes in Eq. 2.39. We use values of 82.65823 GPa and 409.76935 GPa in our code.

A5 Iron Snow

Our model lunar core's adiabatic temperature profile is slightly less steep ($\frac{\partial T}{\partial P}$) than the Fe melting curve at the same pressures. For the right x_{S}^{s}, this means that the core could be solid at the core-mantle boundary but then become liquid at higher pressures. This creates an unphysical scenario in our model wherein a denser layer overlies a less-dense layer. However, if such a situation were to occur in reality, this unphysicality would be remedied by the dynamical motion of the denser layer. This phenomenon is known as Iron snow and it has been proposed to describe the present state of Ganymede's core (Hauck et al.; 2006), the future state of Mars' core (Stewart et al.; 2007), and possibly the current state of Mercury's core (Dumberry and Rivoldini; 2015; Chen et al.; 2008). Alternatively, the sinking iron could re-melt then float back upwards, resulting in compositional convection that could explain the modern-day dynamo of Ganymede (Christensen; 2015a,b; Rückriemen et al.; 2015; Brügger et al.; 2020). Essential to the phenomenon of Iron snow is the relation of the core composition to the eutectic, the lowest melting temperature achieved in an alloy, which cannot be accommodated for by our monotonic function for melting temperature of Eq. 2.22 (Brügger et al.; 2020; Unterborn et al.; 2020).

Nevertheless, we do obtain a solid outer core and liquid inner core for Mercury compositions between 0.0264 and 0.0290 $M_{\oplus}$ (the exact numbers change with even minor changes in core composition). Our model Mercury's temperature is within 51 K of the melting curve throughout the entire core, indicating that even small changes to our model–such as the inclusion of a eutectic–could result in Iron snow within our model Mercury and in Mercury-like planets more broadly.

Gaidos et al. (2010) proposed that Iron snow could occur in super-Earths, however, the newer iron melting curves used in this work from Dong, Fischer, Stixrude, Brennan, Daviau, Suer, Turner, Meng and Prakapenka (2025); Dong, Mardaru, Asimow, Stixrude and Fischer (2025); González-Cataldo and Militzer (2023) are sufficiently shallow that we found no super-Earths with Iron snow.

The appearance of iron snow in our model, even if it is not consistently handled, is a testament to our model's ability to capture physics over a wide range of planetary parameters.

A6 Stoichiometry

Our solid core, liquid mantle, and post-perovskite mantle all have species abundances calculated identically to Haldemann et al. (2024).

For the liquid core, the total number of Fe, FeS, and FeO are given by Equations 1-3, derived by the constraint that each $Fe_{0.81}S_{0.19}$ depletes 81 times as many free Fe atoms as free S atoms, each FeO deplets Fe and O at a 1:1 rate, and no free S or O are allowed. Note that $\tilde{N}_{\mathrm{Fe}}$ represents the number of free Fe atoms while N_{Fe} represents the total number of Fe atoms.

$$\tilde{N}_{Fe} = N_{Fe} - \frac{81}{19}N_S - N_O \tag{1}$$

$$\tilde{N}_{FeS} = N_S \tag{2}$$

$$\tilde{N}_{FeO} = N_O \tag{3}$$

When calculating molar fractions, we need a total molar mass for a denominator, yielding Eq. 4.

$$N_{Fe} - \frac{81}{19}N_S - N_O + N_S + N_O = N_{Fe} - \frac{81}{19}N_S \tag{4}$$

Dividing Equations 1-3 by Eq. 4 and utilizing the fact that number fractions are proportional to molar fractions yields Equations 5-7.

$$\tilde{x}^l_{Fe} = \frac{x_{Fe} - \frac{81}{19}x_S - x_O}{x_{Fe} + (1 - \frac{81}{19})x_S} \tag{5}$$

$$\tilde{x}^l_{Fe} = \frac{x_{Fe} - \frac{81}{19}x_S - x_O}{x_{Fe} + (1 - \frac{81}{19})x_S} \tag{6}$$

$$\tilde{x}^l_{FeO} = \frac{x_O}{x_{Fe} + (1 - \frac{81}{19})x_S} \tag{7}$$

Bibliography

Anderson, J. D., Schubert, G., Jacobson, R. A., Lau, E. L., Moore, W. B. and Sjogren, W. L. (1998). Europa's Differentiated Internal Structure: Inferences from Four Galileo Encounters, *Science* **281**: 2019.

Archinal, B. A., Acton, C. H., A'Hearn, M. F., Conrad, A., Consolmagno, G. J., Duxbury, T., Hestroffer, D., Hilton, J. L., Kirk, R. L., Klioner, S. A., McCarthy, D., Meech, K., Oberst, J., Ping, J., Seidelmann, P. K., Tholen, D. J., Thomas, P. C.

and Williams, I. P. (2018). Report of the IAU Working Group on Cartographic Coordinates and Rotational Elements: 2015, *Celestial Mechanics and Dynamical Astronomy* **130**(3): 22.

Ashkenazy, Y. (2016). The surface temperature of Europa, *arXiv e-prints* p. arXiv:1608.07372.

Brügger, N., Burn, R., Coleman, G. A. L., Alibert, Y. and Benz, W. (2020). Pebbles versus planetesimals. The outcomes of population synthesis models, **640**: A21.

Chen, B., Li, J. and Hauck, S. A. (2008). Non-ideal liquidus curve in the Fe-S system and Mercury's snowing core, **35**(7): L07201.

Christensen, U. R. (2015a). Corrigendum to "Iron snow dynamo models for Ganymede" [Icarus 247 (2015) 248-259], **256**: 63–65.

Christensen, U. R. (2015b). Iron snow dynamo models for Ganymede, **247**: 248–259.

Dong, J., Fischer, R. A., Stixrude, L. P., Brennan, M. C., Daviau, K., Suer, T.-A., Turner, K. M., Meng, Y. and Prakapenka, V. B. (2025). Nonlinearity of the post-spinel transition and its expression in slabs and plumes worldwide, *Nature Communications* **16**(1): 1039.

Dong, J., Mardaru, G.-D., Asimow, P. D., Stixrude, L. P. and Fischer, R. A. (2025). Structure and Melting of Fe, MgO, SiO_2, and $MgSiO_3$ in Planets: Database, Inversion, and Phase Diagram, **6**(4): 103.

Dumberry, M. and Rivoldini, A. (2015). Mercury's inner core size and core-crystallization regime, **248**: 254–268.

Fortney, J. J., Helled, R., Nettelmann, N., Stevenson, D. J., Marley, M. S., Hubbard, W. B. and Iess, L. (2018). The Interior of Saturn, *in* K. H. Baines, F. M. Flasar, N. Krupp and T. Stallard (eds), *Saturn in the 21st Century*, pp. 44–68.

Gaidos, E., Conrad, C. P., Manga, M. and Hernlund, J. (2010). Thermodynamic Limits on Magnetodynamos in Rocky Exoplanets, **718**(2): 596–609.

Genova, A., Goossens, S., Mazarico, E., Lemoine, F. G., Neumann, G. A., Kuang, W., Sabaka, T. J., Hauck, S. A., Smith, D. E., Solomon, S. C. and Zuber, M. T. (2019). Geodetic Evidence That Mercury Has A Solid Inner Core, **46**(7): 3625–3633.

Gomez Casajus, L., Zannoni, M., Modenini, D., Tortora, P., Nimmo, F., Van Hoolst, T., Buccino, D. and Oudrhiri, K. (2021). Updated Europa gravity field and interior structure from a reanalysis of Galileo tracking data, **358**: 114187.

González-Cataldo, F. and Militzer, B. (2023). Ab initio determination of iron melting at terapascal pressures and Super-Earths core crystallization, *Physical Review Research* **5**(3): 033194.

Haldemann, J., Dorn, C., Venturini, J., Alibert, Y. and Benz, W. (2024). BICEPS: An improved characterization model for low- and intermediate-mass exoplanets, **681**: A96.

Hauck, S. A., Aurnou, J. M. and Dombard, A. J. (2006). Sulfur's impact on core evolution and magnetic field generation on Ganymede, *Journal of Geophysical Research (Planets)* **111**(E9): E09008.

Helled, R. (2018). The Interiors of Jupiter and Saturn, *Oxford Research Encyclopedia of Planetary Science*, p. 175.

Jacobson, R. A., Antreasian, P. G., Bordi, J. J., Criddle, K. E., Ionasescu, R., Jones, J. B., Mackenzie, R. A., Meek, M. C., Parcher, D., Pelletier, F. J., Owen, Jr., W. M., Roth, D. C., Roundhill, I. M. and Stauch, J. R. (2006). The Gravity Field of the Saturnian System from Satellite Observations and Spacecraft Tracking Data, **132**(6): 2520–2526.

Khan, A., Sossi, P. A., Liebske, C., Rivoldini, A. and Giardini, D. (2022). Geophysical and cosmochemical evidence for a volatile-rich Mars, *Earth and Planetary Science Letters* **578**: 117330.

Konopliv, A. S., Park, R. S., Rivoldini, A., Baland, R.-M., Le Maistre, S., Van Hoolst, T., Yseboodt, M. and Dehant, V. (2020). Detection of the Chandler Wobble of Mars From Orbiting Spacecraft, **47**(21): e90568.

Kopp, G. and Lean, J. L. (2011). A new, lower value of total solar irradiance: Evidence and climate significance, **38**(1): L01706.

Mankovich, C., Marley, M. S., Fortney, J. J. and Movshovitz, N. (2019). Cassini Ring Seismology as a Probe of Saturn's Interior. I. Rigid Rotation, **871**(1): 1.

Mankovich, C. R. and Fortney, J. J. (2020). Evidence for a Dichotomy in the Interior Structures of Jupiter and Saturn from Helium Phase Separation, **889**(1): 51.

Mankovich, C. R. and Fuller, J. (2021). A diffuse core in Saturn revealed by ring seismology, *Nature Astronomy* **5**: 1103–1109.

Margot, J.-L., Campbell, D. B., Giorgini, J. D., Jao, J. S., Snedeker, L. G., Ghigo, F. D. and Bonsall, A. (2021). Spin state and moment of inertia of Venus, *Nature Astronomy* **5**: 676–683.

Mazarico, E., Genova, A., Goossens, S., Lemoine, F. G., Neumann, G. A., Zuber, M. T., Smith, D. E. and Solomon, S. C. (2014). The gravity field, orientation, and ephemeris of Mercury from MESSENGER observations after three years in orbit, *Journal of Geophysical Research (Planets)* **119**(12): 2417–2436.

Militzer, B. and Hubbard, W. B. (2023). Relation of Gravity, Winds, and the Moment of Inertia of Jupiter and Saturn, **4**(5): 95.

Moulik, P. and Ekström, G. (2025). Radial structure of the Earth: (I) Model concepts and data, *Physics of the Earth and Planetary Interiors* **361**: 107319.

Parmentier, V., Guillot, T., Fortney, J. J. and Marley, M. S. (2015). A non-grey analytical model for irradiated atmospheres. II. Analytical vs. numerical solutions, **574**: A35.

Preising, M., French, M., Mankovich, C., Soubiran, F. and Redmer, R. (2023). Material Properties of Saturn's Interior from Ab Initio Simulations, **269**(2): 47.

Rückriemen, T., Breuer, D. and Spohn, T. (2015). The Fe snow regime in Ganymede's core: A deep-seated dynamo below a stable snow zone, *Journal of Geophysical Research (Planets)* **120**(6): 1095–1118.

Saillenfest, M., Lari, G., Boué, G. and Courtot, A. (2021). The past and future obliquity of Saturn as Titan migrates, **647**: A92.

Saliby, C., Fienga, A., Briaud, A., Mémin, A. and Herrera, C. (2023). Viscosity contrasts in the Venus mantle from tidal deformations, **231**: 105677.

Stewart, A. J., Schmidt, M. W., van Westrenen, W. and Liebske, C. (2007). Mars: A New Core-Crystallization Regime, *Science* **316**(5829): 1323.

Sur, A., Su, Y., Tejada Arevalo, R., Chen, Y.-X. and Burrows, A. (2024). APPLE: An Evolution Code for Modeling Giant Planets, **971**(1): 104.

Sur, A., Tejada Arevalo, R., Su, Y. and Burrows, A. (2025). Simultaneous Evolutionary Fits for Jupiter and Saturn Incorporating Fuzzy Cores, **980**(1): L5.

Unterborn, C., Schaefer, L. and Krijt, S. (2020). The composition of rocky planets, *Planetary Diversity: Rocky planet processes and their observational signatures*, IOP Publishing Bristol, UK, pp. 5–1.

Wang, X., Li, L., Jiang, X., Fry, P. M., West, R. A., Nixon, C. A., Guan, L., Karandana G, T. D., Albright, R., Colwell, J. E., Guillot, T., Hofstadter, M. D., Kenyon, M. E., Mallama, A., Perez-Hoyos, S., Sanchez-Lavega, A., Simon, A. A., Wenkert, D. and Zhang, X. (2024). Cassini spacecraft reveals global energy imbalance of Saturn, *Nature Communications* **15**(1): 5045.

Williams, J. G., Konopliv, A. S., Boggs, D. H., Park, R. S., Yuan, D.-N., Lemoine, F. G., Goossens, S., Mazarico, E., Nimmo, F., Weber, R. C., Asmar, S. W., Melosh, H. J., Neumann, G. A., Phillips, R. J., Smith, D. E., Solomon, S. C., Watkins, M. M., Wieczorek, M. A., Andrews-Hanna, J. C., Head, J. W., Kiefer, W. S., Matsuyama, I., McGovern, P. J., Taylor, G. J. and Zuber, M. T. (2014). Lunar interior properties from the GRAIL mission, *Journal of Geophysical Research (Planets)* **119**(7): 1546–1578.

Zeng, L., Jacobsen, S. B., Sasselov, D. D., Petaev, M. I., Vanderburg, A., Lopez-Morales, M., Perez-Mercader, J., Mattsson, T. R., Li, G., Heising, M. Z., Bonomo, A. S., Damasso, M., Berger, T. A., Cao, H., Levi, A. and Wordsworth, R. D. (2019). Growth model interpretation of planet size distribution, *Proceedings of the National Academy of Science* **116**(20): 9723–9728.

Zhang, J. and Rogers, L. A. (2022). Thermal Evolution and Magnetic History of Rocky Planets, **938**(2): 131.